



Departament de Ciència dels
Materials i Enginyeria Metal·lúrgica

UNIVERSITAT POLITÈCNICA DE CATALUNYA

Micromechanical characterization of small volumes by means of Nanoindentation

Nuria Cuadrado Lafoz

Supervisors: Marc J. Anglada Gomila

Daniel Casellas i Padró

*A Thesis submitted to opt to the degree of Doctor in the Universitat
Politècnica de Catalunya*

Escola Tècnica Superior d'enginyeria Industrial de Barcelona (ETSEIB)

Barcelona. July 2013



Acta de qualificació de tesi doctoral

Curs acadèmic:

Nom i cognoms
NURIA CUADRADO LAFOZ

DNI/NIE/Passaport
43452027J

Programa de doctorat
Ciència i Enginyeria dels Materials

Unitat estructural responsable del programa
Ciència dels Materials i Enginyeria Metal·lúrgica (CMEM)

Resolució del Tribunal

Reunit el Tribunal designat a l'efecte, el doctorand / la doctoranda exposa el tema de la seva tesi doctoral titulada

Acabada la lectura i després de donar resposta a les qüestions formulades pels membres titulars del tribunal, aquest atorga la qualificació:

APTA/E NO APTA/E

(Nom, cognoms i signatura)		(Nom, cognoms i signatura)	
President/a		Secretari/ària	
(Nom, cognoms i signatura)			
Vocal	Vocal	Vocal	Vocal

_____, _____ d'/de _____ de _____

El resultat de l'escrutini dels vots emesos pels membres titulars del tribunal, efectuat per l'Escola de Doctorat, a instància de la Comissió de Doctorat de la UPC, atorga la MENCIÓ CUM LAUDE:

SÍ NO

(Nom, cognoms i signatura)	(Nom, cognoms i signatura)
Presidenta de la Comissió de Doctorat	Secretària de la Comissió de Doctorat

Barcelona, _____ d'/de _____ de _____

To my parents

Agraïments

Al llarg de tots els anys que ha durat aquesta tesi, he tingut l'ajuda i col·laboració, en molts casos desinteressada, de moltes persones i institucions. Sense ànim d'oblidar-me a ningú, m'agradaria agrair tots els consells, opinions i suports tant tècnics com humans, que he rebut i que m'han ajudat a tirar endavant aquest repte.

En primer lloc agrair tant al Dr. Marc J. Anglada com al Dr. Daniel Casellas la seva confiança, dedicació i paciència dipositades en aquesta tesi doctoral. El seu esforç i a la seva orientació m'han permès seguir endavant i concloure satisfactòriament aquest projecte. Agrair també al Dr. Emilio Jiménez i al Dr. Luís Miguel Llanes, la seva dedicació i discussions constructives que han ajudat a la millora tant de la part experimental com teòrica d'aquesta tesi. Sense el suport de la Universitat Politècnica de Catalunya i de la Fundació CTM Centre Tecnològic, així com del seu director el Dr. José Manuel Prado, que m'han donat la possibilitat de realitzar aquesta tesis en les seves instal·lacions, cap dels resultats que aquí es presenten serien realitat.

Vull fer menció especial a l'Àrea de Tecnologia de Materials del CTM pel seu suport, ajuda i acolliment. També en particular a Marc Sebastià, Iban Gonzalez i Eduard Vidales per la seva inestimable ajuda en la realització d'aquesta tesi Han estat moltes hores davant les polidores, així com innumerables sessions de SEM que ens han ajudat a descobrir moltes coses, com el teu alter-ego de psicòleg. Indubtablement, agrair la paciència infinita dels meus companys de despatx: Montse, Raül, Jaume, Giselle, Ainhoa, i no tant de despatx, Iban; m'heu hagut d'aguantar que sé que no és fàcil. Han estat molts anys de teràpia de grup molt valuosa i de neurones perdudes pel camí; sense el comitè aquesta tesi no seria el que és.

Fora del món acadèmic i/o laboral, moltes persones han ajudat a créixer mica en mica aquesta tesi. En primer lloc, tot agraïment queda curt per als meus pares; gràcies per la vostra confiança, paciència, consells i ànims, sense el vostre ajut no hagués arribat a on sóc ara. A la meva germana, Montse, i a la seva família tot el suport i ajuda mostrat, en especial a la Jània i a l'Oriol, per saber treure somriures d'on no n'hi han. Agrair també la confiança i recolzament que he rebut de la petita família que afortunadament he anat trobant al llarg de tots aquest anys. A Helena i a Gemma per ser-hi sempre, tant en els bons moments com en els dolents, que bé sabem que n'hi ha hagut. Gràcies per acollir-me a casa vostra, allà a on fos, per animar-me a seguir endavant, per tots els consells i moments viscuts, heu estat i sempre sereu un gran suport. A Masquè per totes les aventures i experiències viscudes, poder compartir aquest viatge, que tu també has viscut en les pròpies carns, ha estat molt divertit i encoratjador. A Raül, Darta, Dani, per deixar-me compartir amb vosaltres el sofà dels perdedors, les maratons de cine, la xocolata encara que faci mal, han estat moltes estones que han ajudat a fer passar molt millor alguns dels

moments difícils que ha tingut aquesta tesi. I per últim, encara que no per això ets els menys important, gràcies per tots els moments que m'has donat, per acompanyar-me en les llargues jornades de treball, per confiar-hi i animar-me en aquesta última etapa, i sobretot, per voler compartir el que vingui de nou.

A tots, als que hi sou i també als que no hi sou, gràcies per haver-me deixat compartit aquesta experiència amb vosaltres.

Abstract

Mechanical characterization of micro-volume systems, as thin films or micro-sized phases embedded in multiphase materials, has attracted special interest in the last decades since different micromechanical techniques have been developed to characterize microdevices and materials at the micro and nano scale and it has become apparent that mechanical properties may depend on the analysis scale. An example is the way a crack grows in a bulk material that is likely to be different from crack propagation in a micro-volume where crack and microstructural dimensions are comparable. Consequently, there is a need of a detailed knowledge of material properties at micro and nano scale to design materials with advanced mechanical properties. In this way, micro and nanoscale science and technology enables to improve new materials and applications at macroscopic scale through a sound micromechanical design.

The accuracy of test methodologies will depend on the size scale in which specific mechanical properties are studied. Micro scale is usually defined as the length scale in the range of 1-1000 microns, whereas nanoscale is usually defined as smaller than a one tenth of a micrometer in at least one dimension, although this term is sometimes also used for materials of larger dimension but smaller than one micrometer. Efforts to characterize the mechanical response of small volumes have led to the development of a variety of test methodologies, as uniaxial micro testing machines, micro beam cantilever deflection or nanoindentation devices. Challenges of testing at the micro scale include micro specimen preparation and handling, the application of small forces, and stress and strain measurement.

Nanoindentation appears as the easiest way to study local behaviour on thin films or micro-sized phases, since no special sample preparation is required and tests can be performed quickly and inexpensively. Nanoindentation tests consist in the application of a controlled load on the specimen surface through the direct contact with a sharp diamond indenter and recording the evolution of the load versus the penetration depth of the indenter.

The use in engineering of thin films, advanced coatings and materials with small tailored microstructures has led to the analysis of mechanical properties of very small volumes in which size effects might be important. Efforts to design and model the reliability of small-scale devices are directly dependent on the availability of accurate and reliable measurements of relevant mechanical properties at small scales.

In designing structural or machine components an important step is the identification of the main micromechanical damage mechanisms. It is particularly interesting to determine the first fracture step, i.e., the crack nucleation in order to optimize the material resistance to crack nucleation. Stable brittle fracture takes place easily by the contact of a hard indenter on a brittle surface; this methodology is known as indentation fracture. Indentation fracture yields valuable information on the fundamental processes of brittle fracture in covalent-ionic solids, and detail on subsidiary deformation processes in the

contact region; it provides ‘controlled flaws’ for systematically evaluating fracture properties, and it serves as a simple microprobe for determining material fracture parameters, toughness, crack-growth exponent, etc. For materials that exhibit R-curves behaviour, it affords a much needed bridge between the short-crack domain of microstructural flaws and the long-crack domain of traditional toughness testing; mainly in the study of the first regimes of crack propagation. The great appeal of the indentation methodology is its versatility, control and simplicity, requiring only access to routine hardness testing apparatus.

In order to study the mechanical behaviour of small-volumes and micro-sized phases, nanoindentation has become a suitable technique for the mechanical characterization of small-volumes and micrometer – sized phases, in terms of hardness (H), elastic modulus (E) and fracture toughness (K_{Ic}). While H and E can be routinely measured by nanoindentation from the load – displacement curves, the evaluation of K_{Ic} of hard micro-sized phases can in principle be measured from the length of the cracks at the corners of the indentation. This method of evaluation of K_{Ic} is known as *Indentation Microfracture (IM)* and it was proposed in the 1970s for Vickers indentation cracks in bulk materials. However, the design of new materials leads to ever smaller microstructures, hence lower loads and sharper indenters has to be used in order to concentrate the deformation and fracture only in the very small volume of phases of interest.

Mechanical characterization of small volumes, has recently received much attention, and many works have focused on the determination of K_{Ic} by nanoindentation following the IM method. Nanoindentation allows using low loads needed for accurate micromechanical characterization with high spatial resolution. However, the use of a different kind of tip geometry and load range in nanoindentation technique raises some questions about the applicability of the existent fracture toughness equations which were developed in the past mainly for Vickers tips and for loads typically more than two orders of magnitude higher. Therefore, for a better knowledge of the micromechanical behaviour of brittle materials, this work is directed to the study of indentation microfracture applied to small volumes, focussing on the understanding of the fracture behaviour of brittle materials in terms of indenter tip geometry, applied load and crack morphology generated.

On the other hand, since it is of a scientific and technological interest to understand the mechanical response of micro-volume systems, the feasibility of extending the IM developed for brittle bulk materials to engineering systems formed by micro-sized hard phases in multiphase materials or thin films will be also studied.

Contents

Abstract	1
List of Figures	7
List of tables	13
List of symbols.....	15
List of abbreviations	17
Chapter 1. Introduction	19
1.1. Aspects from contact mechanics and indentation	21
1.1.1. Normal contact of elastic and inelastic solids	21
1.1.2. Indentation parameters	26
1.2. Mechanical properties extraction with indentation	30
1.2.1. Mechanical characterization.....	30
1.2.2. Indentation fracture toughness	32
1.3. Objectives.....	45
Chapter 2. Experimental Procedure.....	47
2.1. Materials.....	49
2.1.1. Silicon Nitride, Si ₃ N ₄	50
2.1.1. Hardmetals.....	51
2.1.2. Al-Si Cast Alloy	52
2.1.3. Tool steels.....	54
2.2. Mechanical characterization.....	56
2.2.1. Conventional hardness test.....	56
2.2.2. Instrumented indentation	57

2.3.	Residual imprint characterization.....	60
2.3.1.	Field Emission Scanning Electron Microscopy, FE-SEM	60
2.3.2.	Focused Ion Beam, FIB.....	62
2.3.3.	Sequential polishing technique.....	62
2.3.4.	Crack morphology identification.....	63
2.3.5.	Atomic Force Microscopy, AFM	64
 Chapter 3. Influence of crack morphology on nanoindentation fracture toughness		65
3.1.	Crack morphology evaluation	67
3.1.1.	Crack morphology observations.....	74
3.1.2.	Crack morphology analysis from the $P-h_s$ nanoindentation curves.....	75
3.1.3.	Indentation plastic zone size and crack morphology.....	79
3.2.	Crack morphology effect on K_c with Berkovich and Vickers indenters.	81
3.2.1.	R-curve behaviour effect on fracture toughness evaluated by nanoindentation.....	87
3.3.	Crack morphology effect on K_c with Cube-corner indenters.	90
 Chapter 4. Micromechanical characterization of micro-sized particles by means of Nanoindentation: Influence of Crystal Anisotropy and Residual Stresses effect.....		95
4.1.	Crystal anisotropy on single crystals.....	97
4.2.	Crystal anisotropy and residual stresses effects in multiphase materials	102
4.2.1.	Crystal anisotropy effects.....	103
4.2.2.	Residual stresses effects	110
 Chapter 5. Micromechanical characterization of micro-sized particles by means of nanoindentation: Practical applications.....		119
5.1.	Micromechanical characterization of carbides in tool steels.....	121
5.2.	COD: another method to compute fracture toughness by nanoindentation.....	142
5.3.	Multiphase materials design.....	145

Chapter 6. Conclusions149

 6.1. Conclusions151

 6.2. Future work153

References155

 Published articles 160

List of Figures

Figure 1.1	Indentation of an elastic-plastic half-space by spheres and cones. Small – dashed line — elastic: A cone, B sphere. Solid line — finite elements [1].....	19
Figure 1.2	Cavity model of an elastic-plastic indentation by a cone (adapted from [1]).....	20
Figure 1.3	Plastic region round a spherical cavity expanded by uniformly distributed pressure (adapted from [3])......	20
Figure 1.4	Schematic of an instrumented indentation applied load (P)-penetration depth (hs) curve with the associated contact parameters.....	23
Figure 1.5	Figure 1.5 Schematic representation of (a) sinking-in and (b) pile-up around the contact periphery of a Berkovich and Vickers indentation and associated nomenclature. Note that bulging at the imprint sides indicates pile-up development ($\alpha > 1$), whereas pincushion affects denote sinking-in ($\alpha < 1$).....	23
Figure 1.6	Schematic diagram illustrating the change in the relative contribution of the plastic deformation to the formation of an indentation with an increase in the indentation load, P, ad a change in the corresponding stage of the penetration of an indenter into the material (adapted from [8]).....	27
Figure 1.7	Schematic illustration of a Vickers and a Berkovich indentation with radial cracks showing pertinent dimensions.....	29
Figure 1.8	The typical crack system observed during the indentation of brittle materials. Adapted from Cook and Pharr [16].....	31
Figure 1.9	Scheme of the basic model proposed by Lawn, Evans and Marshall [10].....	32
Figure 1.10	The model for the formation of the indentation plastic zone and subsequent residual stresses, a) elastic half-space before indentation, b) remove hemisphere of material with characteristic radius b , c) indent hemisphere and allow hemisphere to expand at constant volume to $b + \Delta b$, d) elastically compress hemisphere back to original radius, place hemisphere back in hole and allow system to relax.....	32
Figure 1.11	(a) Deformation zone, (b) residual stresses in the uncracked body and (c) scheme of the crack opening profile on the specimen surface (adapted from [19]).....	37
Figure 1.12	Contact stresses in the centre region of a Vickers crack.....	38
Figure 1.13	Total displacements δ_{total} obtained by the superposition of the residual and contact solutions (adapted from [19]).....	39
Figure 1.14	Model for crack initiation at Vickers indentation, (a) quadrant of an indentation with a microcrack; (b) residual shear stress τ_R and tensile stress, σ_R , on microcrack segment. (Adapted from [20]).....	40

Figure 2.1	Microstructure of the Si ₃ N ₄ studied.....	46
Figure 2.2	Microstructures the four grades of hardmetal studied: (a) GD 13; (b) K -30; (c) WC; (d) Resinterized.....	47
Figure 2.3	Morphology of WC grains in WC-Co alloys showing the (0001) basal and {10-10} prismatic facets.....	48
Figure 2.4	Al-Si phase diagram.....	49
Figure 2.5	Microstructure of the Al-Si alloy analysed.....	49
Figure 2.6	Microstructure of (a)1.2379 tool steel, (b) CAST WRA 46 tool steel and (c) UNIVERSAL tool steel.....	50
Figure 2.7	Image of the Nanoindenter used, Nanoindenter XP (MTS).....	54
Figure 2.8	Scheme of the instruments indentation device.....	54
Figure 2.9	Scheme diagram of typical FE-SEM.....	57
Figure 2.10	Scheme diagram of a typical FIB-SEM.....	58
Figure 2.11	Scheme diagram of a typical AFM.....	60
Figure 3.1	Crack evolution SEM images of a Vickers indentation in soda-lime glass at 2 N using the sequential polishing technique (a, b, c, d, e, f). In the final steps and 5% HF etching has been applied (e, f) and (g) shows the 3D crack morphology reconstruction.....	65
Figure 3.2	Crack evolution SEM images of a Berkovich indentation in soda-lime glass at 2 N using the sequential polishing technique (a, b, c, d, e, f). In the final steps and 5% HF etching has been applied (e, f) and (g) shows the 3D crack morphology reconstruction.....	66
Figure 3.3	Crack morphology system for a cube-corner indentation in soda-lime glass using FIB tomography at (a) 5 mN, (b) 10 mN, (c) 20 mN, (d) 50 mN and (e) 100 mN. Yellow area corresponds to the indentation impression, violet indicates the crack morphology.....	68
Figure 3.4	Crack morphology of a cube-corner indentation in Si (100) at 20 mN using FIB tomography. Yellow area corresponds to the indentation impression, green indicates the crack morphology.....	69
Figure 3.5	Crack morphology of a cube-corner indentation in SiC-6H (0001) at 50 mN using FIB tomography. Yellow area corresponds to the indentation impression, blue indicates the crack morphology.....	70
Figure 3.6	Experimental $P-h_s$ curves for Vickers, Berkovich and cube-corner indenters and soda-lime glass, Si (100) and SiC-6H (0001) samples.....	74
Figure 3.7	TEM images of microindentations in SiC-6H showing the dislocation density around it at 50 mN (Adapted from [45]).....	77

Figure 3.8	Vicker indentation on:(a) soda lime glass at 10 N, (b) Si (100) at 200 mN, (c) SiC-6H (0001) at 1,5 N; Berkovich indentation on: (d) soda-lime glass at 0,5 N, (e) Si (1000) at 177 mN, (f) SiC-6H (0001) at 650 mN.....	78
Figure 3.9	Experimental calibration fitting of the constant ξ_R in Anstis <i>et al.</i> equation (equation 1.22) for a Berkovich indenter.....	79
Figure 3.10	Experimental calibration fitting of the constant k^p in Laugier equation (equation 1.25) for a Berkovich indenter.....	79
Figure 3.11	Experimental calibration fitting of the constant in Niihara equation (equation 1.24) for a Berkovich indenter.....	82
Figure 3.12	Crack evolution SEM images of a Berkovich indentation in Si ₃ N ₄ at 20 N using the sequential polishing technique.....	84
Figure 3.13	$P-h_s$ curves for Berkovich indenters for Si ₃ N ₄	85
Figure 3.14	R-curve behaviour for Si ₃ N ₄ evaluated by nanoindentation.....	85
Figure 3.15	Cube-corner indentation on: (g) soda-lime glass at 50 mN, (h) Si (100) at 10 mN, (i) SiC-6H (0001) at 200 mN.....	86
Figure 3.16	Berkovich indentation on (a) Si (111) at 250 mN, (b) SiO ₂ (0001) at 2 N; Cube-corner indentation on (c) Si (111) at 20 mN (d) SiO ₂ (0001) at 50 mN.....	87
Figure 3.17	Experimental calibration fitting of the constant k_p in Laugier equation (equation 1.25) for a cube-corner indenter.....	88
Figure 4.1	Representation of the unit cell for Al ₂ O ₃ ($\bar{1}\bar{1}20$) and MgO (100) single crystals.....	94
Figure 4.2	SEM images showing the anisotropic way of fracture for the single crystals analysed.....	95
Figure 4.3	Fracture toughness variations with crystal – tip orientation ranging from 0° to 180° with respect the <110> direction.....	96
Figure 4.4	SEM images of (a) a Berkovich indentation imprint and the generated cracks performed at 0.12 N in a Si needle, (b) the final polishing step of the Berkovich indentation imprint presented in (a), (c) a cube-corner indentation at 20 mN in a Si needle.....	100
Figure 4.5	EBSD images indicating the crystallographic orientation of each WC grain.....	101
Figure 4.6	Effect of the crystal anisotropy and ISE on: (a) H, (b) E (pattern bars); (c) the ratio E/H in (0001) basal planes and (10-10), (11-20) prismatic facets.....	102
Figure 4.7	Hall-Petch effect on K _c evaluation for WC crystals.....	104
Figure 4.8	SEM images of cube-corner indentations on different WC crystal planes in hardmetal: (a) prismatic facet (0,15 N), (b) prismatic plane (0,2 N), (d) basal facet (50 mN), (e) prismatic facte (0,25 N), (f) basal facet (50 mN).....	105

Figure 4.9	Schematic of the role of tensile stress and $P-h_s$ behavior under tensile residual stresses. (Adapted from [63]).....	107
Figure 4.10	Schematic of the role of tensile stress and $P-h_s$ behavior under compressive residual stresses. (Adapted from [63]).....	107
Figure 4.11	EBSD images for Si needles in Al-Si alloy.....	108
Figure 4.12	Experimental fit to equation 5.1. Data points correspond to cube-corner indentation performed at different loads and Si needles.....	110
Figure 4.13	SEM images of three Si needles indented at different locations and their corresponding $P-h_s$ curves in comparison with one obtained for a Si single crystal..	111
Figure 4.14	FEM simulations of the residual stresses experimented by Si needles caused the surrounding matrix during the cooling process.....	112
Figure 5.1	SEM images of fracture induced by sharp nanoindenters in MC carbides in CAST WRA 46 tool steel.....	119
Figure 5.2	SEM images of fracture induced by sharp nanoindenters in M_7C_3 carbides in 1.2379 tool steel.....	121
Figure 5.3	SEM images of fracture induced by sharp nanoindenters in MC and M_7C_3 carbides in UNIVERSAL tool steel.....	123
Figure 5.4	FIB tomographies of a cube-corner indentation at 50 mN performed on a MC carbide in a UNIVERSAL sample. Yellow area corresponds to the indentation impression, violet indicates the crack morphology and green corresponds to the carbide-matrix boundary.....	125
Figure 5.5	FIB tomographies of a cube-corner indentation at 200 mN performed on a WC in a hardmetal sample. Yellow area corresponds to the indentation impression, violet indicates the crack morphology.....	126
Figure 5.6	(a) – (b) SEM images and (c)- (j) sequential FIB tomographies of a cube-corner indentation performed at 40 mN in a M_7C_3 carbide in a UNIVERSAL tool steel sample.....	129
Figure 5.7	(a) – (b) SEM images and (c)- (n) sequential FIB tomographies of a cube-corner indentation performed at 30 mN in a M_7C_3 carbide in a UNIVERSAL tool steel sample.....	131
Figure 5.8	(a) SEM images and (b)- (f) sequential FIB tomographies of a cube-corner indentation performed at 20 mN in a M_7C_3 carbide in a UNIVERSAL tool steel sample.....	132
Figure 5.9	Plot of K_c vs. P for a M_7C_3 carbides in a UNIVERSAL sample.....	133
Figure 5.10	SEM images of different sequential polishing steps of MC carbides in CAST WRA 46 tool steel.....	134

Figure 5.11	SEM images of different sequential polishing steps of M_7C_3 carbides in 1.2379 tool steel.....	135
Figure 5.12	SEM image of a cube-corner indentation performed at 10 mN in a MC carbide from a UNIVERSAL tool steel sample.....	135
Figure 5.13	Plot of K_c vs. P for a M_7C_3 carbides in a UNIVERSAL and 1.2379 samples when cube-corner indenters are used.....	136
Figure 5.14	Plot of K_c vs. P for a M_7C_3 carbides in a UNIVERSAL and 1.2379 samples when Berkovich indenters are used.....	137
Figure 5.15	AFM images of (a) cube-corner indentation performed at 100 mN and (b) Berkovich indentation performed at 100 mN.....	139
Figure 5.16	(a) SEM image and (b) AFM image of an indented WC crystal.....	140
Figure 5.17	SEM and their corresponding EBSD images of a crack path in a hardmetal sample.	141
Figure 5.18	SEM image of: (a) a damaged tool steel and (b) the initial fracture point located in a primary carbide.....	142

List of tables

Table 2.1	Fracture toughness values determined by the SENB method	46
Table 2.2	Chemical composition and hardness of the hardmetals studied.....	49
Table 2.3	Chemical composition of the studied Al-Si alloy (in wt%).....	50
Table 2.4	Chemical composition of the studied steels (in wt%).....	52
Table 2.5	Heat treatments applied to the studied steels and obtained hardness.....	52
Table 2.6	Chemical composition of the metal part of carbides (in wt%).....	52
Table 3.1	Comparison of crack lengths measured by FIB and SEM in microns.....	68
Table 3.2	Summary of the pop-in and pop-out events observed in the experimental $P-h_s$ curves.....	72
Table 3.3	Yield strength evaluation from Johnson's model and CME's model using the plastic zone size computed by FIB tomographies.....	77
Table 3.4	Experimental calibration of the constants ξ_R and k^p for a Berkovich indenter for Anstis et al. and Laugier equations.....	81
Table 3.5	K_c values computed using Anstis equation (equation 1.22) and Laugier equation (equations 1.25) for Vickers and Berkovich indenters.....	81
Table 3.6	Experimental calibration of the constants in Niihara equation for a Berkovich indenter.....	83
Table 3.7	K_c values computed using Niihara equation (equations 1.23 and 1.24).....	84
Table 3.8	K_c values computed using Laugier equation (equations 1.25) for Berkovich and cube-corner indenters.....	89
Table 4.1	K_c values computed by means of IM method without any orientation consideration.....	96
Table 4.2	Schmid factor for the 12 possible slip systems for Si.....	99
Table 4.3	H and E of Silicon needles.....	100
Table 4.4	K_c of Silicon needles.....	100
Table 4.5	Hardness anisotropy in WC crystals.....	103
Table 4.6	Fracture toughness of WC at different crystal orientation.....	105
Table 4.7	σ_{res} evaluated for Si (111) needles.....	110
Table 4.8	σ_{res} evaluated for Si (100) needles.....	110
Table 5.1	Micromechanical characterization of hard particles evaluated by means of nanoindentation.....	118
Table 5.2	Comparison of K_c of MC and M_7C_3 carbides in CAST WRA 46, 1.2379 and UNIVERSAL tool steels computed using either Berkovich or cube-corner tips.....	125

Table 5.3	K_c values obtained by IM method (equation (1.25)) and COD method (equation (1.30)).....	140
------------------	--	-----

List of symbols

α	surface deformation around an indentation (pile-up or sink-in)
a	radius of the imprint which is equivalent to the radius at the spherical cavity
A	true project contact area
A_s	geometrical projected area
β	geometrical factor that depends on the indenter geometry
c	plastic zone radius
δ_{total}	crack opening displacement
d	diameter of the contact circle in spherical indentation
d'	length of the imprint diagonal in Vickers hardness
D	diameter of the indenter in spherical indentation
E	Young's modulus of the specimen
E_{eff}	effective Young's modulus
E_i	Young's modulus of the indenter
E'	plane strain modulus
E_{bond}	bonding energy between atoms
f	geometrical factor that depends on the indenter geometry
H	hardness
h	true height of the contact surface
h_e	elastic displacement
h_p	plastic displacement
h_s	penetration depth
h_c	contact depth
h_{max}	maximum penetration depth
ϕ	angle between the loading and the perpendicular to the slip plane in Smith law
κ	constant stiffness of the material
k	bulk modulus
k^p	material independent constant containing elements relating to the geometry of the indenter and the crack system in Lawn equation
K	stress intensity factor
K_c	fracture toughness
K_{res}	residual stress intensity factor
λ	angle between the loading direction and the slip direction in Smith law
l	crack length
n	strain-hardening exponent

P	indentation applied load
p	pressure distribution
\bar{p}	hydrostatic component of the stress tensor
p_m	mean contact pressure
θ	indenter half-apex angle
R	indenter radius in spherical indentation
r	radial component
σ	stress tensor
σ_{ys}	yield stress
σ_{cont}	contact stress
σ_{res}	residual stress
ν	Poisson's ratio of the specimen
ν_i	Poisson's ration of the indenter
V	volume
ξ_R	material independent constant containing elements relating to the geometry of the indenter and the crack system in Anstis <i>et al.</i> equation
Ψ	constant that depends on the crack morphology
ψ	included angle between opposite faces of a indenter pyramid

List of abbreviations

AFM	Atomic Force Microscopy
BHN	Brinell Hardness Number
CME	Chiang, Marshall and Evans's model
COD	Crack Opening Displacement
cRnE	<i>Centre de Recerca de Nanoenginyeria</i>
CVD	Chemical Vapor Deposition
EBSD	Electron Back Scatter Diffraction
EDX	Energy Dispersive X-ray Spectrometry
FE-SEM	Field Emission Scanning Electron Microscope
FIB	Focused Ion Beam
IIT	Instrumented Indentation Testing
IM	Indentation Microfracture
ISE	Indentation size effect
VH	Vickers Hardness
wt%	Wight percentage

Chapter 1

Introduction

- Then why do you want to know?
- Because learning does not consist only of knowing what we must or we can do, but also of knowing what we could do and perhaps should not do.

Umberto Eco, The Name of the Rose (1986)

The theoretical background of the analysis of indentation experiments is strongly linked with the field of Contact Mechanics. This discipline provides a description of the stress and strain fields underneath the indenter as well as of the contact pressure distribution existing between the indenter and the material. Contact mechanics gives a mechanistic interpretation of the intrusion of an indenter into a solid which is extremely relevant to the analysis of experimental results.

1.1. Aspects from contact mechanics and indentation

Since the early work by Hertz on the elastic contact between two spherical bodies considerable research efforts have been devoted to study the behaviour of a wide range of solids brought into contact against different indenter geometries [1]. Thus, Contact Mechanics has evolved considerably, providing general descriptions on the link between indentation parameters and mechanical properties. For instance, Sneddon [2] derived a theoretical framework for the contact response attained between an elastic solid and axisymmetric punches (e.g., sphere, cone, or flat-ended punch). He obtained correlations of indentation parameters (such as pressure distribution p , hardness H , and surface deformation around the indenter) in terms of the elastic properties of the solid and the indenter. On the other hand, the slip-line field theory allowed examining the contact response of rigid-perfectly-plastic solids. Characterization of the indentation response of elastic-perfectly-plastic solids was undertaken by Johnson through the analogy between indentation and the expansion of a spherical cavity [1]. In spite of the limitation in such analogy, the results from Johnson's analysis provided important guidelines to the analysis of indentation experiments.

1.1.1. Normal contact of elastic and inelastic solids

Elastic Contact: Hertz theory

The first satisfactory analysis of the stresses at the contact of two elastic solids is due to Hertz. Hertz attempted to use his theory to give a precise definition of hardness of a solid in terms of the contact pressure to initiate plastic yield in the solid by pressing a harder body into contact with it. This definition has proved unsatisfactory because of the difficulty of detecting the point of first yield under the action of constant stress. A satisfactory theory of hardness was only achieved after the development of the theory of plasticity.

Hertz made the hypothesis that the contact area is, in general, elliptical; he then introduced the simplification that, for the purpose of calculating the local deformations, each body can be regarded as an elastic half-space loaded over a small elliptical region of its plane surface. By this simplification, which is still generally followed in contact stress theory, the highly concentrated contact stresses are treated separately from the general distribution of stress in the two bodies which arises from their shape and the way in which they are supported. In order for this simplification to be justifiable two conditions must be

satisfied. The significant dimensions of the contact area must be small compared with the dimensions of each body, and with the relative radii of curvature of the surfaces. This first condition ensures that the stress field calculated on the basis of an infinite solid is not seriously influenced by the proximity of its boundaries to the highly stressed region; the second condition is necessary to ensure that the surfaces just outside the contact region roughly approximate to the plane surface of a half-space, and that the strains in the contact region are sufficiently small to lie within the scope of the linear theory of elasticity.

Finally, the surfaces are assumed to be frictionless so that only a normal pressure is transmitted between them. Although physically the contact pressure must act perpendicular to the interface which will not necessarily be planar, the linear theory of elasticity does not account for changes in the boundary forces arising from the deformation they produce. Hence, in view of the idealization of each body as a half-space with plane surface, normal tractions at the interface are taken to act parallel to the z -axis and tangential tractions to act in the x - y plane.

Elasto-plastic contact

Static indentation hardness test usually involve the application of load to a spherical or pyramidal indenter. The value of the mean contact pressure p_m which does not increase by increasing the indenter load is shown by experiment to be related to the hardness H . Therefore the pressure distribution beneath the indenter is of particular interest. The elasticity of real materials plays an important part in the plastic indentation process. When the yield point is first exceeded the plastic zone is small and fully contained by material which remains elastic so that the plastic strains are of the same magnitude as the surrounding elastic strains. In these circumstances the material displaced by the indenter is accommodate by an elastic expansion of the surrounding solid. As the indentation becomes more severe, either by increasing the load or by using a more acute angle cone, an increasing pressure is required beneath the indenter to produce the necessary expansion. Eventually the plastic zone breaks out of the free surface and the displaced material is free to escape by flow to the sides of the indenter. It is expected that the plastic zone will break out to the surface when the pressure beneath the indenter reaches the value given by rigid-plastic theory:

$$p_m = \phi \sigma_{ys} \quad (1.1)$$

where ϕ is called constrain factor and depends on the geometry of the indenter and friction at the interface, and σ_{ys} is the yield stress.

The indentation response of materials can generally be divided into three regimes, which depend on the uniaxial compressive yield stress σ_{ys} of the material:

- i. $p_m < \sigma_{ys}$: fully elastic response, no permanent or residual impression left in the test specimen after removal of load.

- ii. $\sigma_{ys} < p_m < C\sigma_{ys}$: elasto-plastic response, plastic deformation exists beneath the surface but is constrained by the surrounding elastic material, where C is a constant whose value depends on the material and the indenter geometry.
- iii. $p_m > C\sigma_{ys}$: fully plastic response, plastic region extends to the surface of the specimen and continues to grow in size such that the indentation contact area increases at a rate that gives little or no increase in the mean contact pressure for further increases in indenter load.

The indentation pressure under elastic, elasto-plastic and fully plastic conditions may be correlated on a non-dimensional graph, like in Figure 1.1, where θ is the angle of the indenter at the edge of the contact.

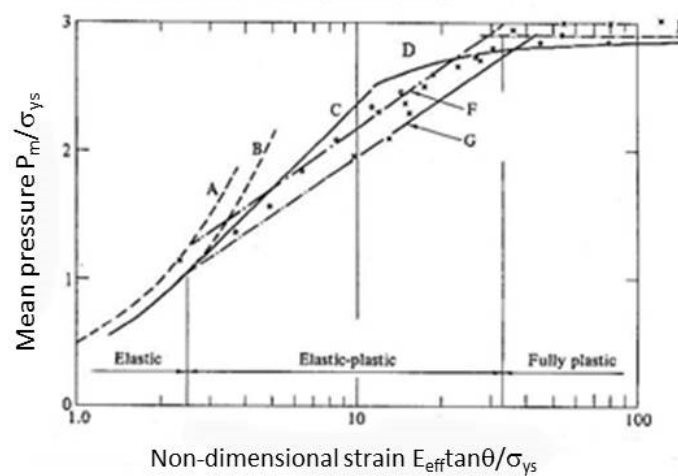


Figure 1.1.—Indentation of an elastic-plastic half-space by spheres and cones. Small – dashed line — elastic: A cone, B sphere. Solid line — finite elements.[1].

In principle the contact stresses due to an elastic-plastic indentation in which the strains remain small can be calculated. In practice this is very difficult because the shape and size of the elastic-plastic boundary is not known a priori. One way to calculate these contact stresses is by means of finite elements, but the high stress concentration makes it difficult to obtain a refined picture of the stress field in the contact zone. An alternative approach is based on the observations of Samuels & Mulhearn that the subsurface displacements produced by any blunt indenter (cone, sphere or pyramid) are approximately radial from the point of first contact, with roughly hemispherical contours of equal strain [1].

In this simplified model, known as spherical cavity model of an elastic-plastic indentation, the contact surface of the indenter is tough encased in a hemi-spherical core of radius a (see Figure 1.2). Within the core there is assumed to be a hydrostatic component of stress \bar{p} . Outside the core it is assumed that the stresses and displacements have radial symmetry and are the same as in an infinite elastic, perfectly-plastic body which contains a spherical cavity under a pressure \bar{p} . The elastic-plastic

boundary lies at a radius c , where $c > a$. At the interface between core and the plastic zone the hydrostatic stress in the core is just equal to the radial component of stress in the external zone, and the radial displacement of particles lying on the boundary $r = a$ during an increment of penetration dh_s must accommodate the volume of material displaced by the indenter (neglecting compressibility of the core).

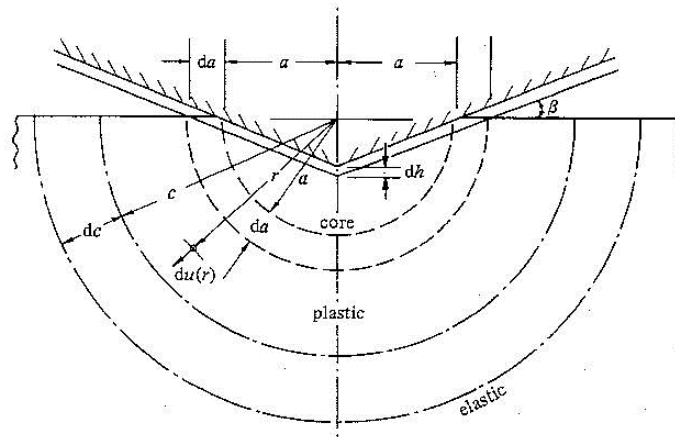


Figure 1.2.- Cavity model of an elastic-plastic indentation by a cone (adapted from [1]).

The solution of a spherical cavity in an infinite solid medium was developed by Hill [3]. In Figure 1.3 is shown a cavity of internal and external radii a and b respectively, and their initial values are denoted by a_0 and b_0 . The pressure is distributed uniformly over the inner surface, while the external pressure is negligible compared with the yield stress of the material. Inflation of the cavity exerts hydrostatic pressure which modifies the stress-strain state of the surrounding medium. With increasing pressure a plastic region spread into the shell. After an initial elastic behaviour of the solid, further inflation of the cavity leads to the onset of the plastic deformation at a critical value of internal pressure. An elastic-plastic boundary of radius c is thus induced where for $\rho > c$ the solid remains elastic. For reasons of symmetry, the plastic boundary in a homogeneous material must be a spherical surface, its radius at any moment is denoted by c (see Figure 1.3).

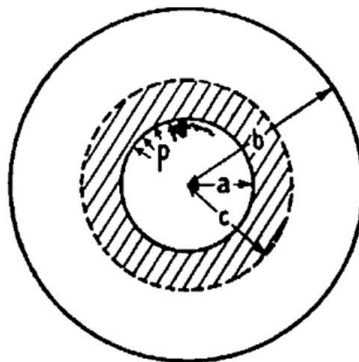


Figure 1.3.- Plastic region round a spherical cavity expanded by uniformly distributed pressure (adapted from [3]).

When a spherical cavity is expanded from zero radii in an infinite medium and a non-worked hardening material is considered, the ratio c/a remains constant.

$$\frac{c}{a} = \left\{ \frac{E}{3(1-\nu)\sigma_{ys}} \right\}^{1/3} \quad (1.1)$$

Thus, the constant internal pressure is

$$p = \frac{2\sigma_{ys}}{3} \left\{ 1 + \ln \left(\frac{E}{3(1-\nu)\sigma_{ys}} \right) \right\} \quad (1.2)$$

This may also be thought as the work needed to create the unit volume of the cavity. When a work hardening material is considered, and the material is treated as incompressible ($\nu = 1/2$) the ratio c/a is as follow

$$\frac{c}{a} = \left(\frac{2E}{3\sigma_{ys}} \right)^{1/3} \quad (1.3)$$

The knowledge of the plastic zone size is important because allows the extraction of the yield stress of a material, the examination, within a continuum framework, of discrete deformation processes occurring at small loads, and the assessment of possible influence of substrate effects on the contact response of thin films and small-volume structures.

In addition to the contact pressure, the depth of penetration of the indenter is also of interest. It is a difficult quantity to determine theoretically, because the uncertain deformation at the edge of the indentation. With a rigid-plastic solid the material displaced by the indenter appears in the indenter shoulder, but with an elastic-plastic solid this is not the case. Most, if not all, of the displaced material is accommodated by radial expansion of the elastic hinterland. The amount of material deformation is also influenced by the strain-hardening properties of the material. A large capacity for strain hardening pushes the plastic zone further into the material and thereby decreases the pile-up adjacent to the indenter. So, the deformation around the indenter imprint is an important effect that has to be taken into account in indentation tests.

1.1.2. Indentation parameters

The contact response of an indented material in instrumented indentation is described by the recorded loading – penetration depth curve. An indentation loading curve is the relationship between load (P) and displacement (h_s) that can be continuously measured during an indentation experiment (see Figure 1.4). Apart from the displacement scale involved, the distinguishing feature of most nanoindentation testing is the indirect measurement of the contact area, that is, the area of contact between the indenter and the specimen. In conventional indentation tests, the area of contact is calculated from direct measurements of the dimensions of the residual impression left in the specimen surface upon the removal of load. In nanoindentation tests, the size of the residual impression is of the order of microns and too small to be conveniently measured directly. Thus, the area of the contact has to be determined by measuring the depth of penetration of the indenter into the specimen surface. This, together with the known geometry of the indenter, provides an indirect measurement of the contact area at full load.

The contact response in a conventional hardness test is described by the hardness. Hardness (H) is calculated as the ratio between the applied load (P) and the projected area of the residual imprint (A), namely,

$$H = \frac{P}{A} \quad (1.4)$$

From this equation one can say that hardness is indicative of the resistance of the material to deform plastically under the action of the indenter. It is well known that immediately outside the contact area of an indentation some deformation usually occurs and the surface does not remain flat [4]. In an indentation into an elastic material, the surface of the specimen is typically drawn inwards and downwards underneath the indenter and sinking-in occurs. When the contact involves plastic deformation, the material may either sink in, or pile up around the indenter. The degree of pile-up or sink-in depends upon the ratio E/σ_{ys} of the specimen material and the strain-hardening exponent n [5]. Piling-up or sinking-in can be quantified by a pile-up parameter given by,

$$\alpha = \frac{A}{A_s} \quad (1.5)$$

where A is the true projected contact area and A_s is the geometrical area that measures the imprint as if the surface would remain flat (i.e., ignoring the development of pile-up or sinking-in), see Figure 1.5.

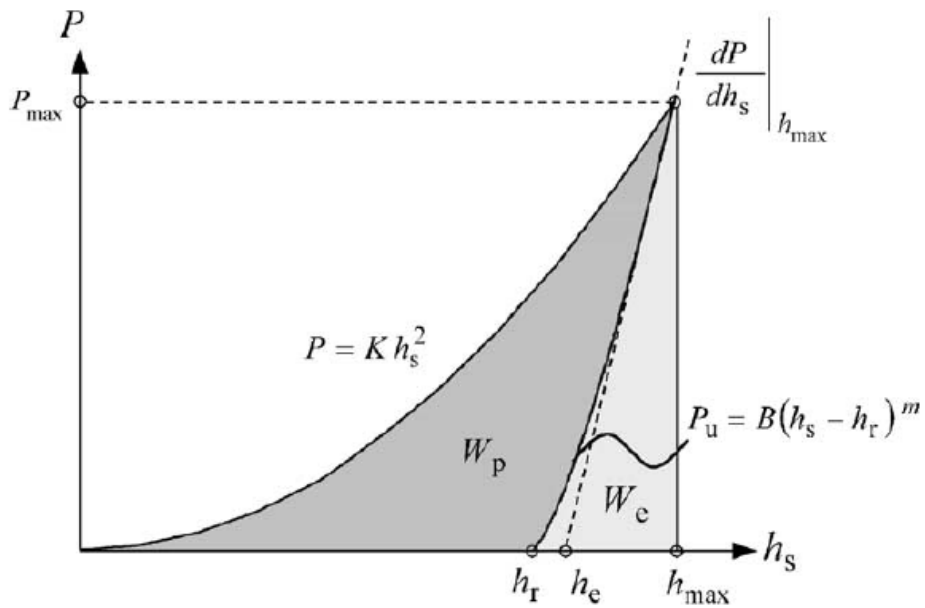


Figure 1.4.-Schematic of an instrumented indentation applied load (P)-penetration depth (h_s) curve with the associated contact parameters.

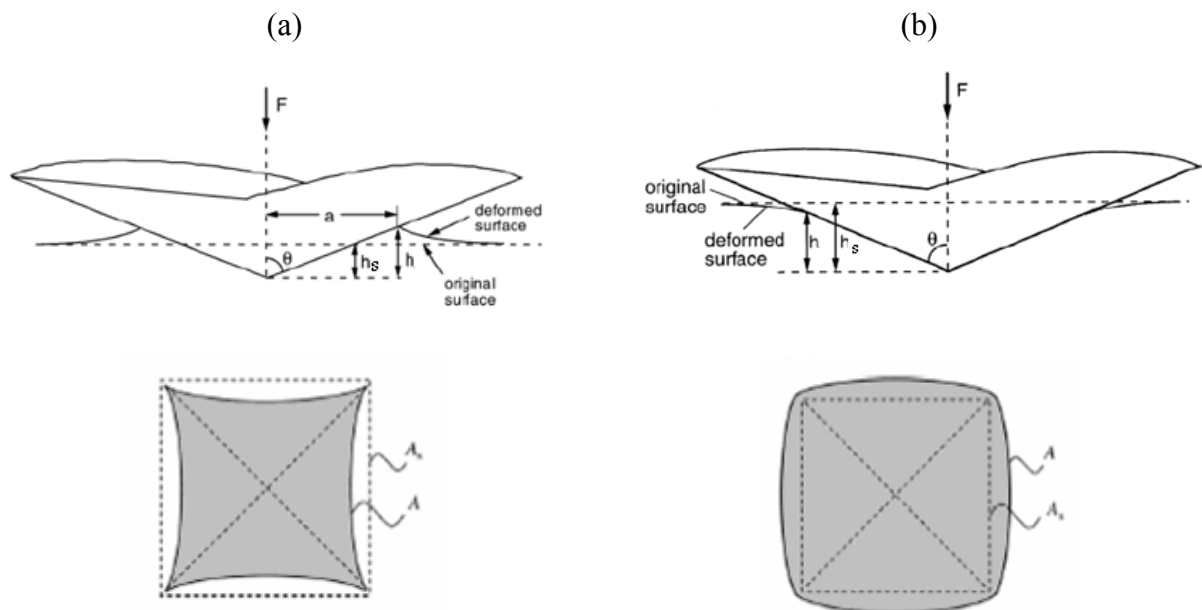


Figure 1.5.-Schematic representation of (a) sinking-in and (b) pile-up around the contact periphery of a Berkovich and Vickers indentation and associated nomenclature. Note that bulging at the imprint sides indicates pile-up development ($\alpha > 1$), whereas pincushion affects denote sinking-in ($\alpha < 1$).

By geometrical arguments, A_s is determined as

$$A_s = fh_s^2 \quad (1.6)$$

where h_s is the penetration depth of the indenter, as measured from the undeformed surface of the material, and f a geometrical factor which depends on the indenter's shape ($f = 24.5$ for the Vickers four-sided indenter; 24.562 for the Berkovich trigonal indenter; and $f = \pi \tan^2 \theta$ for a cone with arbitrary half-apex angle θ). By virtue of the axisymmetry of the conical tip, it follows that it is possible to substitute A_s by A and h_s by h in equation 1.5. Thus, in accordance with equation 1.6, one can measure the amount of pile-up or sink-in using the true height of the contact surface (h) and the penetration depth from the undeformed surface to the indenter's tip (h_s). That is, pile-up occurs when $\alpha > 1$, and sink-in develops for $\alpha < 1$, being the parameter α defined as follows,

$$\sqrt{\alpha} = \frac{h}{h_s} \quad (1.7)$$

Notice that equations 1.5 and 1.7 are equivalent because the apical angle in a conical indentation remains constant around the z-axis so that pile-up and sink-in are homogeneous throughout the contact boundary. Vickers and Berkovich pyramidal indentations, however, have uneven heights along the periphery as a result of the different constraints imposed to the material by the sharp edges of the indenter and its sides. Hence, α varies throughout the contact boundary. In such cases, it becomes necessary to estimate a mean value for the amount of surface deformation through the ratio of contact areas with equation 1.5 rather than with equation 1.7.

Although the occurrence of pile-up and sink-in is indicative of the mechanical response of the material, α cannot be taken as an intrinsic material property because, in the same way as hardness, is the result of a combination of elastic and plastic uniaxial mechanical properties. Hardness H and surface deformation parameter α are also dependant of the indenter's geometry. For non-strain-hardening materials with large value of E/σ_{ys} pile-up is to be expected, since most of the plastic deformation occurs near the indenter. For materials with a low value of E/σ_{ys} (e.g., some glasses and ceramics) sinking-in is more likely to occur. For strain-hardening materials (e.g., a well annealed metal with $n > 0$), the yield strength effectively increases with the strain. Therefore, it is seen that piling-up is most pronounced for non-strain-hardening materials with a high value of E/σ_{ys} . Sinking-in is more pronounced for strain-hardening or non-strain-hardening materials with a low value of E/σ_{ys} [5].

Instrumented indentation experiments evaluate the evolution of the contact response along the loading and the unloading stages of the experiment, providing a complementary knowledge to that given

through measurement of H and α . Analysis of an instrumented indentation $P-h_s$ curve provides an indication of the elastic and plastic responses of the material. The elastic response, characterized through the Young's modulus, E , can be directly obtained from the early unloading stage [6, 7]. The following closed-form solution for elastic contacts with punches of arbitrary shape is used for the purpose of extracting Young's modulus:

$$E_{eff} = \frac{\sqrt{\pi}}{2\beta} \frac{1}{\sqrt{A}} \left. \frac{dP}{dh} \right|_{h_{max}} \quad (1.8)$$

where E_{eff} is the effective elastic modulus defined by

$$\frac{1}{E_{eff}} = \frac{1-\nu^2}{E} + \frac{1-\nu_i^2}{E_i} \quad (1.9)$$

The effective elastic modulus takes into account the fact that elastic displacement occur in both the specimen, with Young's modulus E and Poisson's ratio ν , and the indenter, with elastic constants E_i and ν_i . dP/dh_s is the slope of the $P-h_s$ curve in the first part of the unloading segment (see Figure 1.4), β is a geometrical constant that depends on indenter's geometry, and A is the contact area at maximum load. Since only A_s and not A is inferred from the $P-h_s$ curve, an important limitation in instrumented indentation experiments becomes evident as the use of this formulation requires a prior knowledge on the amount of pile-up or sinking-in. The wide accepted Oliver & Pharr methodology to evaluate H and E in nanoindentation provides an empirical approach for finding true contact area A from penetration depth h_s measurements [7].

The loading segment of the $P-h_s$ curve reflects the elasto-plastic response of the material. In the absence of length scales which may be induced, for instance, by microstructural features, the relation between applied load and penetration depth is prescribed through Kick's law

$$P = \kappa h_s^2 \quad (1.10)$$

where κ is a material constant which, through equations 1.4, 1.5 and 1.6, is related to hardness H and surface deformation parameter α as

$$\kappa = fH\alpha \quad (1.11)$$

this relation demonstrates the link between parameter κ from instrumented indentation experiments and hardness H . Thus, it is considered that the contact response is completely defined by a reduced number of

independent variables: hardness H , surface deformation parameter α , and unloading slope dP/dh_s . The first two parameters (H and α) result from the elasto-plasticity developing at the contact surface (that is, they are anticipated to be functions of yield strength σ_{ys} , hardening coefficient n , and Young's modulus E), while dP/dh_s only concerns the elastic behaviour of the indented material.

1.2. Mechanical properties extraction with indentation

Nanoindentation test allows extracting elastic modulus and hardness of the specimen from load-displacement measurements. In nanoindentation testing, the depth of penetration beneath the specimen surface is measured as the load is applied to the indenter. The known geometry of the indenter then allows the size of the area of contact to be determined. The procedure also allows for the modulus of the specimen material to be obtained from a measurement of the stiffness of the contact, that is, the rate of change of load and depth. Although the most common properties extracted from nanoindentation tests are the hardness and the Young modulus, it is also possible determine the fracture toughness of the material, depending on the geometry of the indenter used. In this section, a reviewed of the indentations tests to extract the mechanical properties of the materials by using different tip geometries is presented.

1.2.1. Mechanical characterization

The methods used for local mechanical testing of materials have often been formally divided into macroindentation, microindentation, nanoindentation, and even picoindentation, according to the characteristic indentation size. An increase in the applied load, P , leads to a change not only in the characteristic size of a locally deformed region, but also in the ratio between the contributions of the elastic and plastic deformations, and in the atomic mechanisms of deformation.

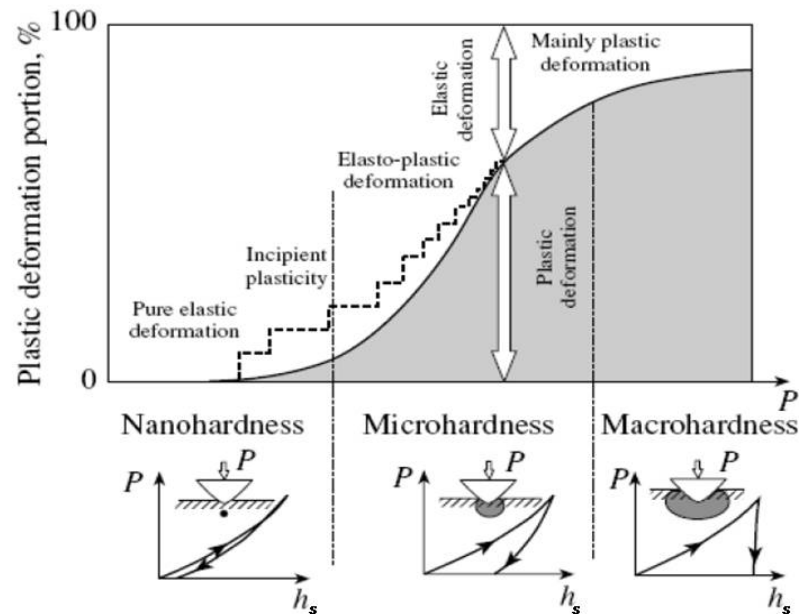


Figure 1.6.- Schematic diagram illustrating the change in the relative contribution of the plastic deformation to the formation of an indentation with an increase in the indentation load, P , and a change in the corresponding stage of the penetration of an indenter into the material (adapted from [8]).

The deformation of materials takes place via two different processes: elastic (reversible) and plastic (irreversible). Since elastic deformation is a reversible process it exhibits virtually no size dependence unless a large population of pre-existing defects is involved. The plastic deformation response, which takes place as a result of the generation, annihilation, and motion of defects such as dislocations, displays marked size effects when they are in the range of microns or below.

During the last 20 years, Instrumented Indentation Testing (IIT) has been widely employed. Also known as depth-sensing indentation, continuous recording indentation, ultra-low-load indentation or nanoindentation, IIT is a relatively new form of mechanical testing, which significantly expands the capabilities of traditional hardness testing. The method was introduced in 1992 for measuring hardness and elastic modulus, it has been widely adopted and used in the characterization of mechanical behaviour at the nanometric scale [6]. This technique has several advantages, firstly it is a local probe that can evaluate the properties of a material in different areas; secondly, it is depth-sensing, so it can characterize a material at different depths. Also, nanoindentation technique is especially well suited for the characterization of small volumes of material, such as single grains in a composite material or thin films and coatings. During the past decade, IIT has introduced several changes to the method that have improved its accuracy and extended its fields of application. These modifications have been developed through experience in testing a large number of materials, and by improvements to testing equipment and techniques [7].

1.2.2. Indentation fracture toughness

Indentation techniques for assessing fracture toughness are attractive due to the simplicity and expediency of experiments, and because they potentially allow the characterization of both local and bulk fracture properties. Accurately measuring the fracture toughness of brittle materials can often be challenging. Creating sharp pre-cracks can be difficult without catastrophically failing the specimen, while fracture toughness data using large cracks from notched specimens can give erroneously high values [9]. For those reasons, assessing fracture toughness by making direct measurements of cracks created using sharp diamond indenters, such as Vickers, Berkovich or cube corner, can appear to be an attractive alternative to more traditional fracture toughness testing techniques [10, 11]. Such tests can be relatively quick and easy to perform, required little specialized equipment, and can allow probing localized microstructural features. Accordingly, such techniques are finding considerable usage in studying the fracture behaviour of micro sized materials.

As with all fracture toughness testing techniques, the ultimate goal is to accurately quantify the fracture toughness in a way that can be universally compared with results generated using other techniques and from other studies. Techniques involving direct measurements from different indent cracks are often unsuccessful in this regard. A secondary goal may be to provide a quick semi quantitative way to rank the toughness of different materials. In this case, indentation techniques can have some merit, but cannot be used indiscriminately. Criticisms to the IM method remark that this technique is not suitable for the measurement of the fracture toughness, K_c , or any other form of the fracture resistance of ceramics or other brittle material. Quinn *et al* state that any agreement with accepted K_c data is either fortuitous or due to force fitting the IM calibration constants [12]. This assertion from Quinn *et al.* is based on some observations on the derivation of the IM methodology. One of the greatest objections is that there are numerous equations, by different authors, highly questionable for none of them are the product of an accurate stress intensity factor. The complex crack network and residual stress damage zone around indentations are not amenable to a straight forward analysis as in most traditional fracture mechanics test configurations. When different equations are applied to estimate resistance, the technique does not compute a unique value of K_c for brittle materials such as ceramics. One reason for this result is that crack initiation and propagation in the IM method test is not the same as the sequence of crack processes in the standardized fracture toughness tests. Quin *et al.* affirm that a fundamental problem with the IM method is that brittle materials do not deform and fracture underneath an indentation in a self-similar manner as many have assumed [12]. Furthermore, the cracks often do not present the semi-circular median or Palmqvist cracks assumed in the models [12].

Despite such criticisms on the IM technique there has been an escalating interest in applying some of the IM method concepts to the nanomeasurements of the K_c of materials by measuring the crack lengths emanating from the three corners of sharp nanoindenters as it is practically the only technique available to determine fracture behaviour of small volumes embedded in a surrounding matrix. One different approach is that proposed by Zhang *et al.* and built in an energy-based method to compute K_c

with cube-corner tips using experimental data and finite-element calculations [13]. With respect to the IM method, Shiffman has performed a study trying to adapt the existing IM models to cube-corner indenters [14]. Morris *et al.* studied the use of IM with cube-corner indenters and conclude that very acute indenters induced an extra crack-driving component due to the acuity of the tip and this leads to uncertainty in the physical basis for K_c estimation using IM [15]. Paying attention at the lack of acceptance in the use of IM with sharp indenters, in this work some of the limitations of, and concerns with, using such indentation fracture techniques will be discussed. Additionally, some new experimental results using cube corner indentation to assess the fracture toughness of micro-sized brittle materials will be presented.

The measurement of fracture toughness by indentations methods

The indentation method relies on the fact that most brittle materials form radial cracks when indented with a sharp indenter such as a Vickers or Berkovich diamond. A Vickers and a Berkovich indentation with radial cracks of length c , along with pertinent dimensions for describing various features of the indentation, are shown schematically in Figure 1.7.

Indentation cracking was first realized as an indication of a material's fracture toughness in the late 50's and early 60's by Palmqvist who worked exclusively on WC-Co cermets, but the concept was encouraged as a fracture toughness test by Evans and Charles in the mid 70's [12]. Evans and Charles suggested that it was possible to utilize the cracks that emanate from the corners of a high testing load Vickers microhardness indentation to determine the fracture toughness of brittle materials. Evans and Charles presented a generalized equation and a normalized calibration curve that appeared to apply to many different materials, some with Palmqvist cracks and some with median cracks, see Figure 1.8b and 1.8c respectively. Subsequently numerous other authors have used similar curve fitting methods and dimensional analyses to improve the methodology of the fracture toughness calculation thorough the crack length generated with an indentation test. In this section it will see the most used equations and their formulation.

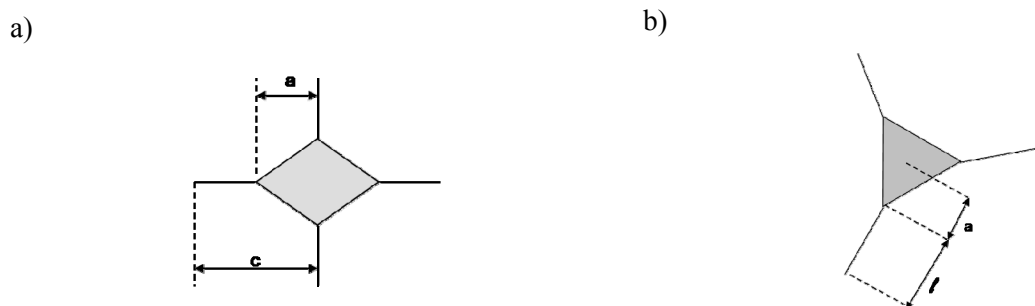


Figure 1.7.- Schematic illustration of a Vickers and a Berkovich indentation with radial cracks showing pertinent dimensions.

In 1975 Lawn and Swain applied the Boussinesq solutions for the stress fields in an isotropic linear elastic half-space under normal point loading to the analysis the crack patterns observed around indentations in brittle materials. Their analysis lead to the first use of two-dimensional linear elastic fracture mechanics to model the propagation of “well-behaved” median cracks, associated with indentation by sharp indenter such as a Vickers diamond, see Figure 1.8c. Median cracks, as observed in transparent materials such as soda-lime glass, were considered as “penny-shaped” internal cracks having a diameter D . For the median crack system, Lawn and Swain were able to estimate the stress intensity factor in terms of the depth of the median crack by

$$K = \left\{ \frac{(1-2\nu)(\alpha p_0)^{1/2}}{2^{1/2} \pi^{1/2} \beta} \right\} \left(\frac{P}{c} \right)^{1/2} \quad (1.16)$$

where α and β are dimensionless constants equal to $2/\pi$ and 2, respectively.

In 1980 Lawn, Evans and Marshall [10] resolved the complex elastic-plastic indentation stress field into two components: a reversible elastic stress field component and a irreversible residual stress component resulting from the plastic zone surrounding an indentation, see Figure 1.9. The elastic stress field component, operating outside the plastic zone, takes a subordinate role in crack growth because of its reversible nature. The elastic stress field, however, enhance the growth of subsurface median cracks while at the same time restricts the growth of surface radial (Palmqvist) cracks during loading. Upon unloading the effects are reversed: median-crack growth is suppressed and surface radial crack growth is enhanced. The residual stress field component provides the driving force for both median and surface radial crack growth during unloading. This ultimately results in an equilibrium half-penny configuration upon complete removal of the load. Thus, the dominance of the residual stress field is responsible for the creation of the half-penny crack configuration.

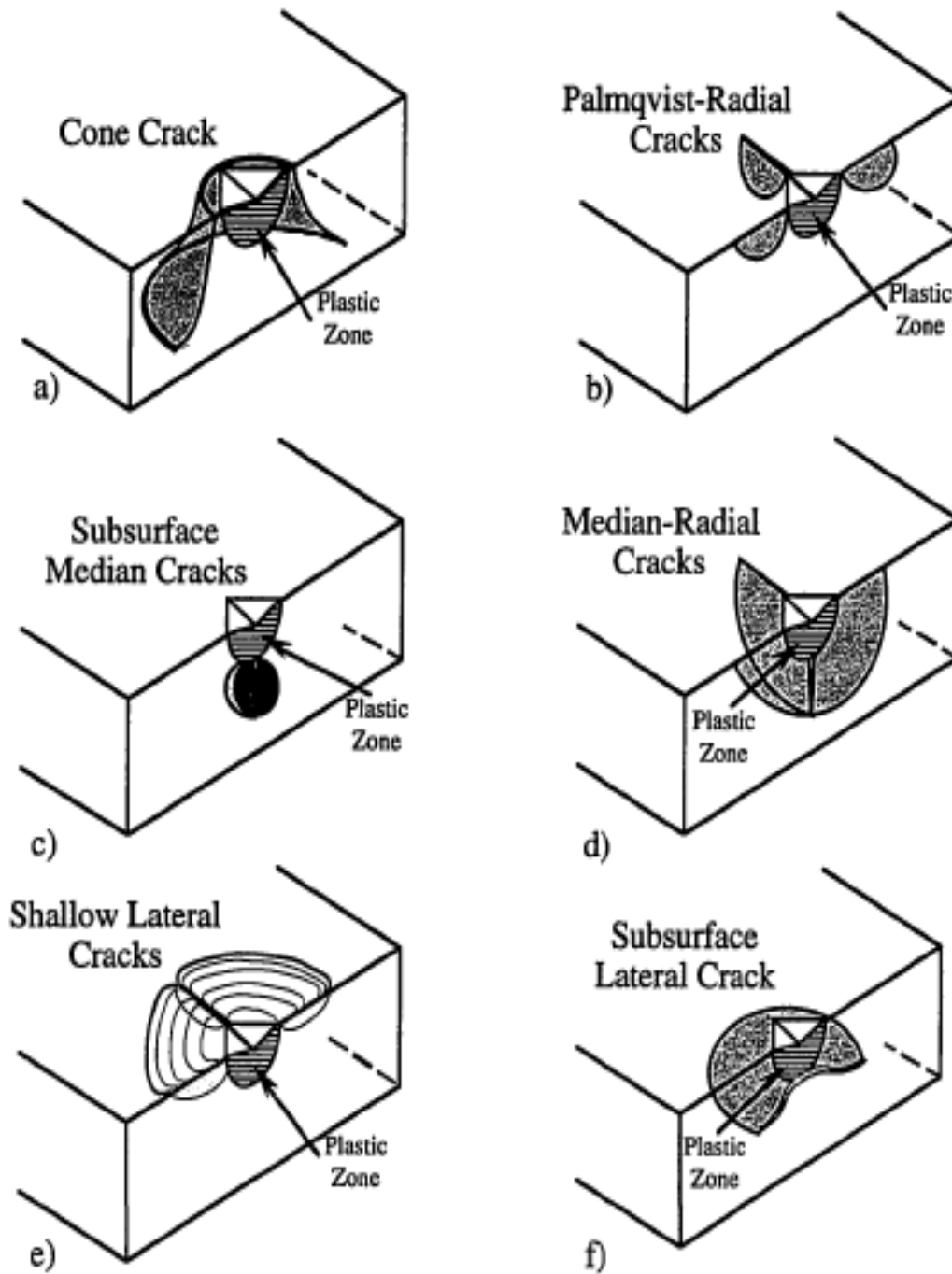


Figure 1.8.- The typical crack system observed during the indentation of brittle materials. Adapted from Cook and Pharr [16].

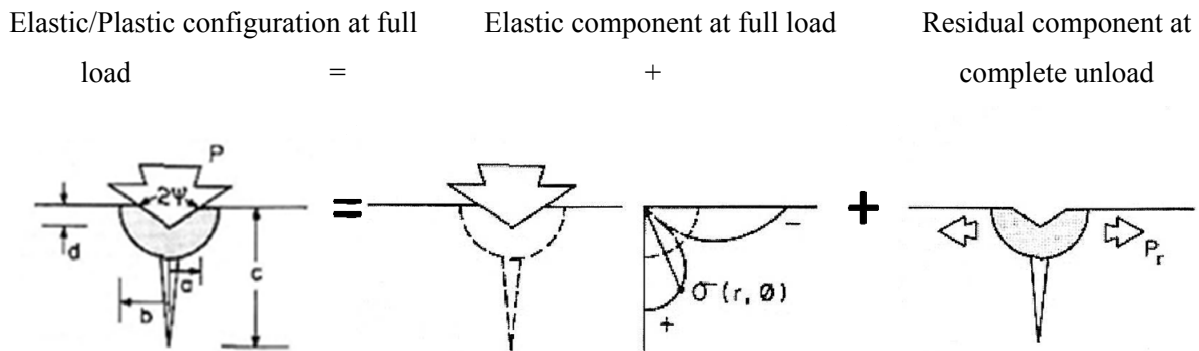


Figure 1.9.- Scheme of the basic model proposed by Lawn, Evans and Marshall [10].

The origin of the residual stresses, which ultimately determine the final lengths of indentation cracks is schematized in Figure 1.10. First, a small hemisphere of material is removed from an elastic half-space (see Figure 1.10b), and plastically deformed by indentation (see Figure 1.10c).

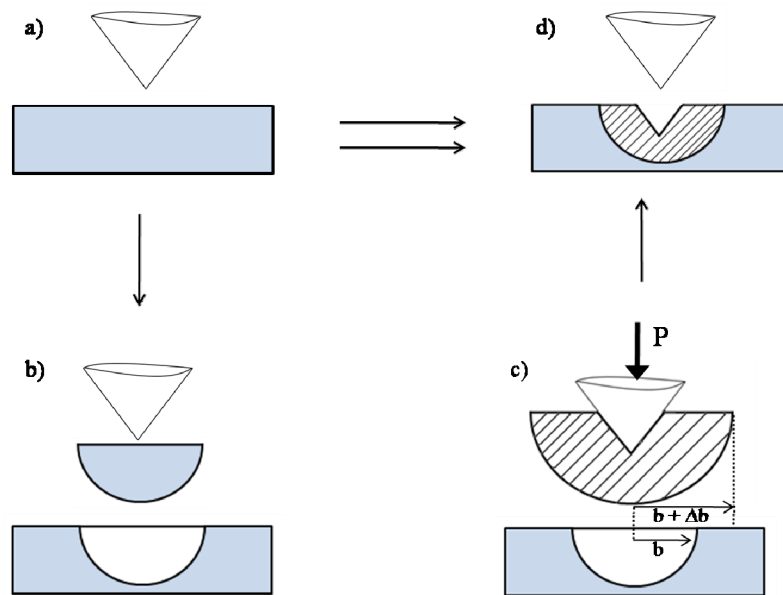


Figure 1.10.- The model for the formation of the indentation plastic zone and subsequent residual stresses, a) elastic half-space before indentation, b) remove hemisphere of material with characteristic radius b , c) indent hemisphere and allow hemisphere to expand at constant volume to $b + \Delta b$, d) elastically compress hemisphere back to original radius, place hemisphere back in hole and allow system to relax.

The irreversible strain associated with the formation of the impression is accommodated by an expansion of the radius of the hemisphere maintaining constant volume. If ΔV is the volume displaced by a Vickers indenter and V is the volume of material removed from the elastic half-space, the volumetric strain is

$$\frac{\Delta V}{V} = \left(\frac{a}{b}\right)^3 \cot \psi \quad (1.17)$$

where a is the Vickers indent half-diagonal and b is the radius of the hemisphere, i.e., the plastic zone radius. The hemisphere is elastically compressed back to its original radius by hydrostatic compression across the outer boundaries. The pressure required to restore the hemisphere to its original radius is given by

$$p_b = k \left(\frac{\Delta V}{V}\right) \quad (1.18)$$

where k is the bulk modulus. The compressed hemisphere is reinserted into the original cavity, restoring coherence at the interface and allows the system to relax. Relaxation of the surface over the surface diametral plane must inevitably modify the stresses at the elastic plastic interface. Consequently, the plastic zone can be considered as a source of effective outward residual force on the crack, the magnitude of this force may be obtained by integrating the horizontal stress components over the zone cross section within the crack plane, assuming p_b to remain effectively invariant with crack size, the reduced pressure on the relaxed hemisphere from the constraint of the matrix is given by

$$p_r = p_0 b^2 \quad (1.19)$$

In the limit of “well-developed” cracks $c \gg b$, these forces may be regarded as concentrated at a point. Assuming penny-like crack geometry, the stress intensity factor due to the residual far field force may be written as,

$$K_r = f(\phi) \frac{P}{c^{3/2}} \quad (1.20)$$

where $f(\phi)$ is an angular function introduced to allow for the effects of the free surface; generally $f(\phi)$ is a slowly varying function, of value near unity, with its minimum at $\phi = 0^\circ$ (median orientation) and maximum at $\phi = \pm 90^\circ$ (radial orientation). Combining equations p_b , p_r and K_r we obtain

$$K_r = \chi_r \frac{P}{c^{3/2}} \quad (1.21)$$

$$\text{with } \chi_r = f(\phi) \left(\frac{a}{b} \right) \left(\frac{E}{H} \right) \cot \psi .$$

Lawn *et al.* extended their analysis by using Hill's expanding cavity solution to determine the relative plastic zone size, b/a , and the effect of material parameters and indenter geometry on plastic zone size. Lawn *et al.* considered the approximate result $\frac{b}{a} \approx \left(\frac{E}{H} \right)^{1/2} (\cot \Psi)^{1/3}$, on the assumption that this result remains a good approximation for the equivalent half-space problem and assuming $K_r = K_c$, the equilibrium condition necessary for crack arrest in a decaying stress field, substitution into equation 1.21 gives

$$K_c = \xi_R \left(\frac{E}{H} \right)^{1/2} \frac{P}{c^{3/2}} \quad (1.22)$$

The term ξ_R in Lawn *et al.* analysis was thought to be a material independent constant containing elements relating to the geometry of the indenter and the half-penny crack system. The material properties that govern crack extension were thought to be embodied in the modulus-to-hardness ratio.

In 1981 Anstis *et al.* provided a critical evaluation of equation 1.22 as a basis for using Vickers indentation crack lengths for determining fracture toughness. Anstis *et al.* chose a number of brittle materials covering a wide span of toughness values [11]. The materials were tested to determine their hardness, modulus, and toughness using double cantilever beams when possible (literature values were used when experimental values could not be obtained). Each material was then indented with a Vickers indenter at several loads and the ensuing cracks measured. Plots of $P/c^{3/2}$ versus P revealed that $P/c^{3/2}$ was independent of load, i.e., constant, for each material. Using the experimentally determined values of E , H , K_c , and mean $P/c^{3/2}$ values for each material, the calibration constant α in equation 1.22 was found to be 0.016. The toughness of each material was calculated from indentation crack lengths using equation 1.22 and $\xi_R = 0.016$; the accuracy of the method was found to be within about 40%.

In 1982 Niihara *et al.* used Blendell's curve-fit as an accurate representation of Evans and Charles data that showed that the relation between fracture toughness and ratio of crack-to-indent size exhibited universal behaviour [17]. The normalized toughness versus crack length data of Evans and Charles deviates from a slope of $-3/2$ at c/a values of less than approximately 2.5. The slight reduction in slope from that of the ideal centre-loaded, half-penny crack was recorded in a curve-fit of Evans and Charles's data by Blendell. When Niihara *et al.*'s data did not exhibit the same reduction in slope at $c/a < 2.5$ as Blendell's curve-fit, they understood the lack of deviation in their data as a change in crack morphology

from fully developed half-penny median cracks to Palmqvist cracks. The term “fully developed” was then applied to half-penny cracks having a value of $c/a \geq 2.5$ while Palmqvist cracks were considered to have $c/a < 2.5$. Niihara *et al.* proceeded to develop a normalized empirical expression relating toughness to Palmqvist crack length for Palmqvist cracks in the range $0.25 \leq l/a \leq 2.5$,

$$\left(\frac{K_{Ic}\phi}{Ha^{1/2}} \right) \left(\frac{H}{E\phi} \right)^{2/5} = 0.035 \left(\frac{l}{a} \right)^{-1/2} \quad (1.23)$$

where $\phi \sim 3$, a is the Vickers half-diagonal length, and l is the Palmqvist crack length measured from the corner of the indentation to crack tip, see Figure 1.7. For median cracks ($c/a > 2.5$), the corresponding expression is shown in equation 1.24.

$$\left(\frac{K_{Ic}\phi}{Ha^{1/2}} \right) \left(\frac{H}{E\phi} \right)^{2/5} = 0.129 \left(\frac{c}{a} \right)^{-3/2} \quad (1.24)$$

The value of $-3/2$ for the exponent in equation 1.24 suggests that the formation of median cracks is mechanically equivalent to a penny-shaped crack, wedged by a force, P , at its centre. The exponent of $-1/2$ in equation 1.23 suggests that the formation of the Palmqvist cracks may be mechanically equivalent to a semi-infinite crack loaded by a force P at a distance l from the crack tip.

In 1987 Laugier adapted the Lawn half-penny formalism (equation 1.22) to take into account the morphology of Palmqvist cracks by treating them as a semi-ellipse instead of considering a semi-circle [18]. Calibration of the expression proposed for the stress intensity factor for Palmqvist cracks was performed using the data of Anstis *et al* and led to a new value of $k^p = 0.015$. From a theoretical point of view this approach is more satisfactory, and the value of the stress intensity factor for which the crack arrests is considered to be the fracture toughness,

$$K_c = k^p \left(\frac{l}{a} \right)^{-1/2} \left(\frac{E}{H} \right)^{2/3} \frac{P}{c^{3/2}} \quad (1.25)$$

Indentation microfracture method is very often used for the determination of K_c of brittle materials. Besides its simplicity the indentation test offers the possibility to measure the fracture toughness inside micro sized ceramic grains and thin films using nanoindenters. However, there are some disadvantages with this method that must be considered:

- i. There is an uncertainty associated with the empirical calibration constant required to compute the K_c equations that depends on the indenter used and the crack morphology generated. Thus, such experimental calibration leads to an inherent uncertainty in the computed toughness values.
- ii. The method is problematic for materials that exhibit increasing toughness with crack extension (i.e., R-curve behaviour) because of the presence of extrinsic toughening mechanisms, such as crack bridging in the crack wake. The indentation toughness test gives as essentially a toughness value corresponding to the crack length and geometry of the indentation crack, on the R-curve. This toughness value lies between the intrinsic toughness, K_{I0} , and the steady-state plateau toughness K_c .
- iii. Because of indentation size effect in ceramics, the value of H is not always constant and sometimes depends on the load, P , placing further uncertainty on K_c values computed using the IM method.

An alternative method for evaluating the fracture toughness of ceramics has been proposed by Fett *et al* [19] based on the computed crack-opening displacements (COD) of cracks emanating from Vickers hardness indentations. This alternative method presents some advantages with respect the IM method:

- i. There is no need of an empirical calibration to formulate the expressions for the CODs.
- ii. The hardness is not part of the formulation, erasing any concerns about the indentation size effect.
- iii. The technique only evaluates the crack tip toughness, that is for materials with R-curves only evaluates the initiation or intrinsic toughness.

This alternative method developed by Fett is based on the fact that the remaining stress field after unloading is responsible of the existence of a residual crack opening displacement field. Fett computed the “applied” crack opening displacement field as superposition of the residual stresses in the uncracked material, which result from Vickers indentation and the contact stresses in the inner contact zone. For this purpose, the applied stress field is taken to be analogous to an expanding spherical zone according to Hill, and the indentation crack is assumed to be semi-circular. It is furthermore assumed that the crack is a fully embedded crack, i.e., change of the stress intensity factor along the crack contour is neglected.

The residual stress zone remaining after unloading is illustrated in Figure 1.11. The residual stress is the reason for the Vickers indentation crack being open after unloading (see Figure 1.11c).

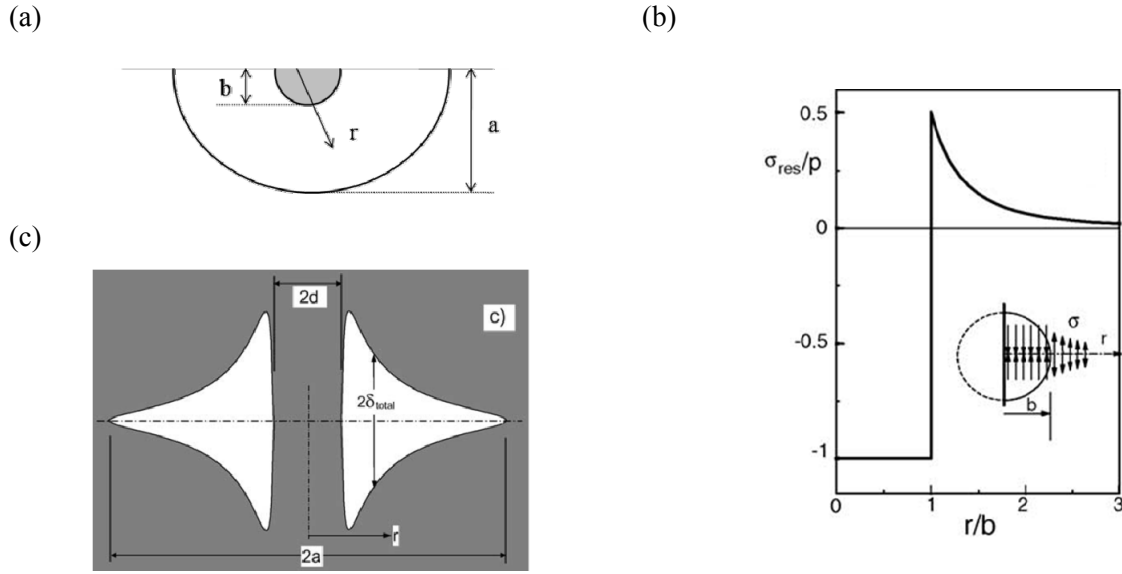


Figure 1.11.- (a) Deformation zone, (b) residual stresses in the uncracked body and (c) scheme of the crack opening profile on the specimen surface (adapted from [19]).

If the tangential component of residual stresses, σ_{res} , is assumed to be

$$\sigma_{res} = \begin{cases} -p & \text{for } r < b \\ \frac{1}{2}p \left(\frac{b}{r}\right)^3 & \text{for } r > b \end{cases} \quad (1.26)$$

where b is the extension of the compressive zone and p is the applied load. Then the residual stress intensity factor of the crack of radius a is given as

$$K_{res} = \frac{2}{\sqrt{\pi a}} \int_0^a \frac{r \sigma_{res}(r) dr}{\sqrt{a^2 - r^2}} = -\frac{2p}{\sqrt{\pi a}} \left(a - \sqrt{a^2 - b^2} - \frac{1}{2} \left(\frac{b}{a}\right)^2 \sqrt{a^2 - b^2} \right) \leq 0 \quad (1.27)$$

In equation 1.26 it can be observed that K_{res} is negative for any b/a . As a first consequence of the negative residual stress intensity factor, penetration of the crack faces has to be expected at least for the near-tip crack opening displacement field. In a real structure, crack face penetration is not possible. Prevented crack face penetration must result in a distribution of (positive) contact stress σ_{cont} , which causes a positive contact COD field and a contact stress intensity factor

$$K_{cont} = \frac{2}{\sqrt{\pi a}} \int_0^a \frac{r \sigma_{cont}(r) dr}{\sqrt{a^2 - r^2}} \quad (1.28)$$

This stress intensity factor is positive, since the contact stresses open the crack. The related contact stresses are restricted to a contact area of radius d with $d \approx b$ and must disappear in the region of real (positive) crack opening (see Figure 1.12).

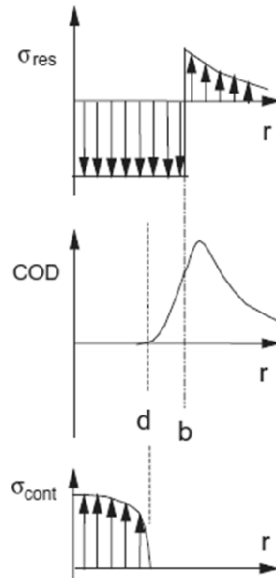


Figure 1.12.-Contact stresses in the centre region of a Vickers crack.

The total stress results by superposition of the residual and the contact stresses, so that, the total stress intensity factor is the sum of K_{res} and K_{cont} . Thus, the total crack opening displacements is given by

$$\delta_{total}(r) = \frac{4}{\pi E'} \int_r^a \left(\int_0^{a'} \frac{r' \sigma_{total}(r')}{\sqrt{a'^2 - r'^2}} dr' \right) \frac{da'}{\sqrt{a'^2 - r^2}} \quad (1.29)$$

Where E' is the plane strain modulus, i.e. $E' = \frac{E}{1 - \nu^2}$.

The small deviations from $\delta_{total} = 0$ in $0 \leq r \leq b$ indicate the slight differences between the correct and the approximate contact stress solutions. Total displacements are represented in Figure 1.13 in terms of r/b . The related total stress intensity factor exhibits the well-established proportionality $K \propto a^{-3/2}$ for $a/b \geq 2.5$.

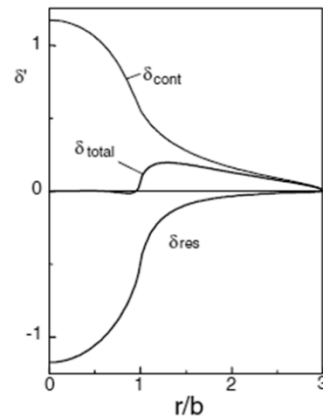


Figure 1.13.-Total displacements δ_{total} obtained by the superposition of the residual and contact solutions (adapted from [19]).

The determination of the crack-tip toughness is reduced to the near-tip displacement field in practical applications. A series expansion of δ_{total} gives

$$\delta_{tip} = \sqrt{\frac{8}{\pi}} \frac{K_{tip}}{E'} \sqrt{a-r} \quad (1.30)$$

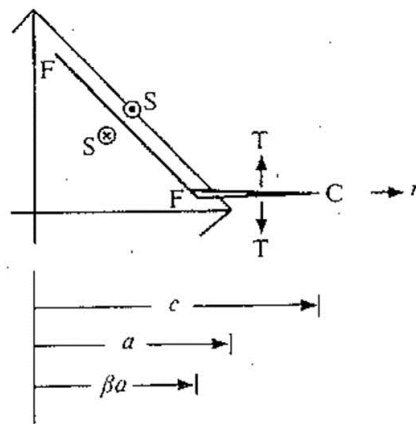
The application of the near-tip approximation is recommended for $\frac{a-r}{b} \leq 1 + 0,15 \frac{a}{b}$ and $2.5 \leq \frac{a}{b} \leq 10$.

Crack initiation

Once K_c evaluation from indentation test has been done, an important issue is the study of micromechanics of crack initiation. Johnson showed that there is a critical load for radial cracking; however this threshold is insensitive to surface state, implying that the indentation creates its own flaw population within the inelastic contact zone [1]. For covalent-ionic solids the contact pressure is of the same order as the intrinsic cohesive strength, thus deformation of the rigidly bonded structure takes place thorough shear faulting. This kind of deformation does tend to occur in directions of highest shear stress in the manner of dislocations, and it is not confined to ordinarily preferred glide planes.

From the crack observations in soda-lime glass and fused silica induced by a Vickers indenter, Johnson suggested that the driving force for radial crack initiation comes from the residual field from an elastic – plastic expanding cavity representation of the deformation zone. His model is shown in Figure 1.14, the fault FF is regarded as a constrained shear crack with uniform friction stress τ_R at its interface, extending radially from its edge as a tensile segment FC into the outer field $\sigma_R(r)$. Thus, for equilibrium fracture, radial pop-in will occur spontaneously when $\tau_R > \sigma_R$.

(a)



(b)

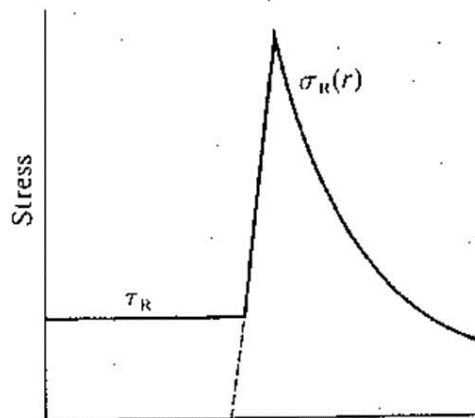


Figure 1.14.- Model for crack initiation at Vickers indentation, (a) quadrant of an indentation with a micro-crack; (b) residual shear stress τ_R and tensile stress, σ_R , on micro-crack segment. (Adapted from [20]).

Apart from crack initiation it is worth studying the cracking sequence in order to understand the fracture behaviour of brittle materials. Cook and Pharr determined this sequence for soda-lime glass thanks to its transparency [16].

- i. Radial cracks: initiate on unloading and grow to full length on complete unload. The radial cracks are nucleated by flaws at the deformation zone boundary and are driven by the residual stress field arising from the mismatch of the plastically deformed zone embedded in the surrounding elastically restraining matrix.
- ii. Median cracks: appear when peak load is increased and are initiated on loading. On unloading median cracks spread outward along the surface to leave half-penny geometry at complete unload, being wedged loaded by the residual field.

- iii. Lateral cracks: appear at high peak loads, and they are nucleated beneath the deformation zone on the unloading and grow to reach full size at complete unload, similar to radial cracks.

However, this sequence it is not considered general since has rarely been observed. Acoustic emission measurements made for different authors indicate activity at the indentation site only during loading, and such measurements correlate directly with the observation of radial cracks [16]. Thus, it seems that soda –lime glass cracks in different ways from the majority of brittle materials, in both morphology and sequence.

1.3. Objectives

The indentation cracking method for determining fracture toughness has typically been applied to Vickers indentations made at relatively high loads. The main aim of this investigation is extent the indentation cracking method to nanoindentation, where three-sided pyramidal Berkovich and cube corner indenters are used and lower loads are applied. One of the issues to consider in detail in applying indentation cracking method with other indenter geometries is the considered crack morphology. The existent fracture toughness equations depend on both the tip geometry and the crack morphology generated; thus, accurate K_c measurements require a proper knowledge of crack morphology in order to select the most appropriate expressions for evaluating K_c by means of nanoindentation.

Thus, the main objectives of this work can be summarized as follows:

1. Extend the applicability of indentation microfracture method to the three-sided pyramidal indenters and the low loads used with nanoindentation technique.
2. To assess the applicability of the IM method for obtaining K_c of small material volumes by means of nanoindentation, taking into account the influence of the indenter geometry (Vickers, Berkovich and cube-corner) and the generated crack morphology.
3. To apply the nanoindentation technique in multiphase materials in order to perform a mechanical characterization, including hardness, Young's modulus and fracture toughness of their constituents phases, particularly when one is in the form of micro-sized particles.

Furthermore, the cracking threshold diminishes when using the cube-corner indenter, thus the indentation cracking method can be applied with smaller loads for measuring fracture toughness with indentations that are submicron in size and allowing in this way, small volumes to be mechanically characterized. Multiphase materials are often formed by micro-sized particles which are single crystals

embedded in a softer matrix. Thus, this investigation will deal with some aspects inherent to single crystals,

- i. Anisotropy: mechanical properties of single crystals can change depending on their crystallographic orientation. This effect should be taken into account when fracture is analysed in small crystals as those present in the studied materials.
- ii. Residual stresses: when fracture toughness of micro-sized particles embedded in a matrix or thin films are evaluated it has to be taken into account the residual stresses imposed by the matrix and the substrate, respectively, and how these stresses could affect the initiation and propagation of the cracks generated by nanoindentation.
- iii. Matrix effects: in this work micro-sized particles surrounded by an elastic matrix were analysed. Thus, an important aspect to take into account during the mechanical evaluation of the particles is the elastic effects that could introduce the matrix on their plastic and fracture behaviour.

Experimental Procedure

To help our blindness's so as to devise
a pair of new and artificial eyes
By whose augmenting power we now see
more than all world has ever done before.

Henry Powers (1664)

2.1. Materials

The materials used in this thesis have been chosen carefully in order to study the dependency of the indentation cracking method with the generated crack morphology and therefore with the indenter geometry. The following premises have been considered:

1. The IM method will be applied onto micro-sized brittle particles in multiphase materials as metallic carbides in tool steels, WC in hardmetals or Si particles in Al-Si cast alloys. According to the aims of this work, the chosen materials should be as similar as possible to the hard particles of these alloys, that is, ceramic materials with covalent bonds shall be studied.
2. It is well known that there are some polycrystalline ceramic materials that present R-curve behaviour, i.e., their fracture toughness depends on the crack length. If R-curve behaviour is present, the toughness developed with cracks induced by nanoindentation will differ from that obtained from large cracks. Thus, materials without R-curve behaviour will be studied. Consequently, amorphous and single crystal materials were chosen.
3. Since a calibration of the existing indentation fracture toughness equations will be performed for the different the tip geometries, the materials chosen should have a well known fracture toughness independent of any calibration constant. There exist several standardized procedures for fracture toughness determination such as the single-edge precracked beam (SEPB), chevron-notched beam (CNB), surface crack in flexure (SCF) methods or single edge notch bend (SENB), which do not precise experimental calibrations. Nevertheless, there is scarce information in the literature of K_{Ic} values for single crystals obtained by means of standardized methods.

Following these premises and according to material availability the fracture behaviour of soda-lime glass, Si (100) and SiC-6H (0001) were studied. Fracture toughness values reported in the literature for the studied materials by using the SENB method are shown in Table 2.1.

Table 2.1. -Fracture toughness values determined by the SENB method.

Material	$K_{Ic\ SENB}$ (MPa·m ^{1/2})
Soda-lime glass	0.7 [11]
Si (100)	0.95[21]
SiC-6H	3.4 [22]

Influence of crack morphology and tip geometry in fracture toughness IM equations was studied using the materials reported in Table 2.1. Because fracture toughness equations depend on an experimental constant that include the tip geometry and the crack morphology effect, in this work the value of this constant for three tip geometries, Vickers, Berkovich and cube-corner, and for two crack morphologies, radial and Palmqvist cracks was experimentally assessed. Two additional single crystals were analysed, Si (111) and SiO₂ (0001) for which no information about K_c determined with standardized methods was found in the literature. To overcome this lack of knowledge K_c was determined by IM using the value obtained after calibration with soda-lime glass, Si (100) and SiC-6H (0001) for the Berkovich indenter. The values obtained for K_c with this tip were used for the experimental calibration of K_c equations for cube-corner tip geometry.

For the study of the application of the IM method at the nanoindentation level to the micro-sized particles of engineering alloys, three tool steels (1.2379, UNIVERSAL, CAST WRA 46), a hypereutectic Al-Si cast alloy with 67 wt % Si and different grades of hardmetals were chosen.

2.1.1. Silicon Nitride, Si₃N₄

A material with R-curve behaviour, polycrystalline Si₃N₄, was studied for evaluating the effect of crack size on the fracture toughness computed by nanoindentation.

The Si₃N₄ used here is a commercial material produced by hot-pressing. It was received in the form of rectangular bars of 45 mm x 7 mm and with 3 mm in thickness. The as-received microstructure is fully β-Si₃N₄ and consists of small grains of average size of about 1 μm with some larger elongated grains (Figure 2.1). The material had been densified with a small amount of MgO as a sintering additive. Energy-dispersive spectrometry microanalysis showed the presence of Fe and Al, as well as Mg, on the grain boundaries.

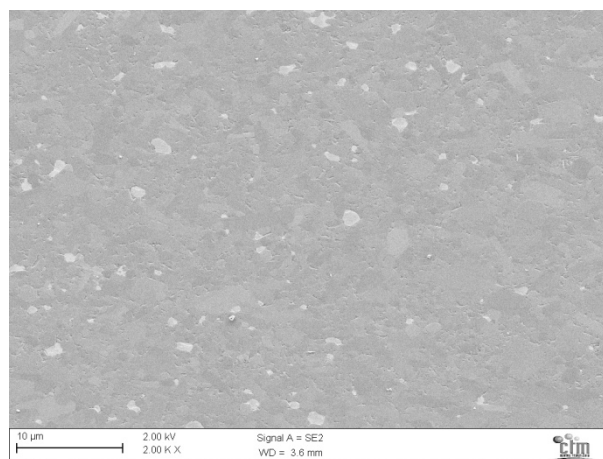


Figure 2.1.-Microstructure of the Si₃N₄ studied.

2.1.1. Hardmetals

WC-Co cemented carbides represent a group of hard and wear-resistant refractory composites in which hard carbide particles are bound together by a ductile and tough binder matrix. They are part of a group of inorganic composites which are commonly referred as hardmetals, which combine the high hardness and strength of the covalent carbides (WC, TiC, TaC) with the toughness and plasticity of the metallic binder (Co, Ni, Fe). Their unique combination of hardness and toughness makes them outstanding as tool materials in the manufacturing industry. In this work, different hardmetal Co grades combining WC and Co were analysed. Tungsten carbide (WC) is the basic and the most widely used hard component. Cobalt was found to be the best binder metal. WC-Co grades, consisting in two phases (WC and Co, Figure 2.2), are often referred to as unalloyed grades or straight tungsten carbide grades. The main role of WC in the microstructure is to provide hardness and wear resistance. On the other hand, the constrained plastic deformation and rupture of the tough Co binder phase ligaments, as well as the fracture of the carbide-binder interfaces mainly account for the global fracture toughness [23].

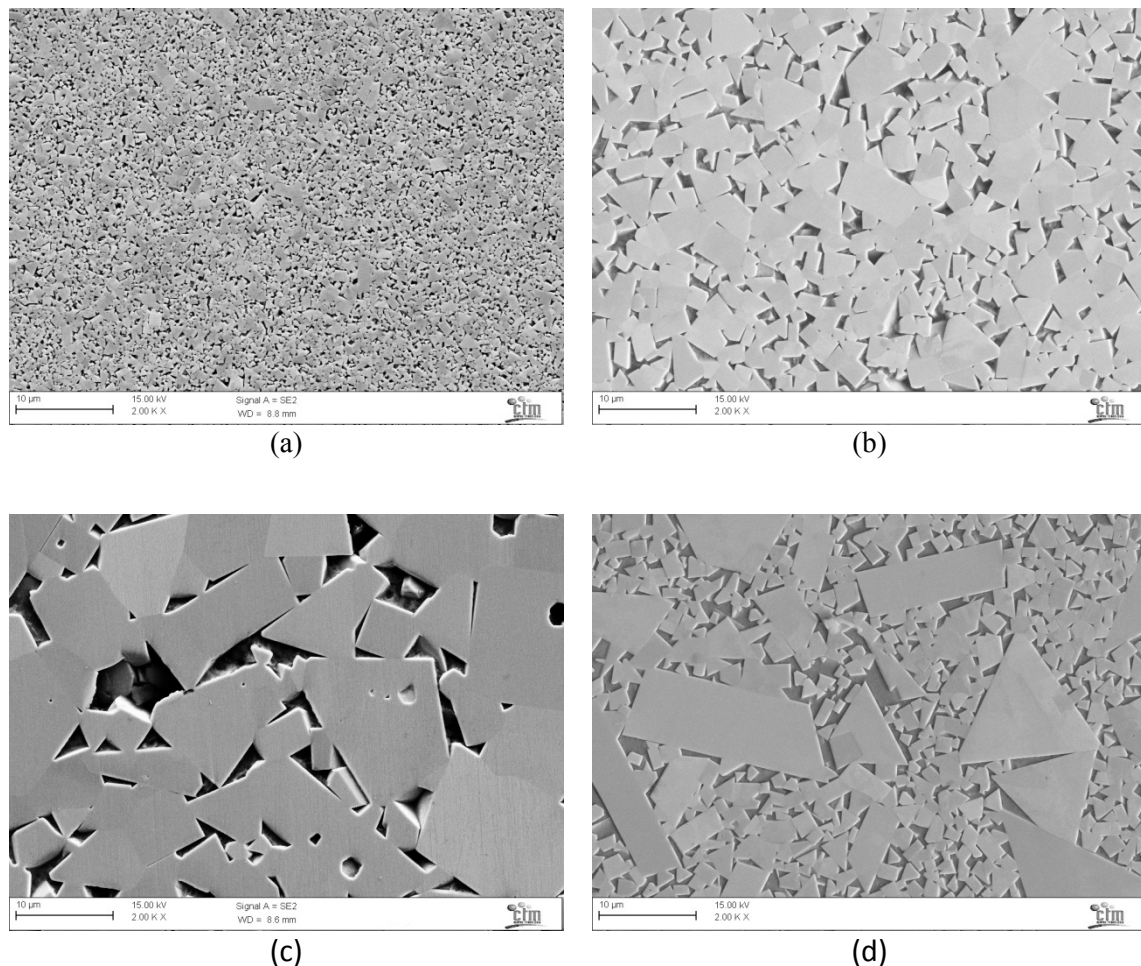


Figure 2.2.- Microstructures the four grades of hardmetal studied: (a) GD13; (b) K -30; (c) WC; (d) Resinterized.

WC presents a hexagonal crystal structure (type P-6m2), with three types of facets: two prismatic $\{10\text{-}10\}$ and one basal (0001) (Figure 2.3) [24]. WC single crystals show a marked anisotropy in hardness, being about 1450 HV for the prismatic planes and about 2500 HV for the basal ones [25]. Such pronounced anisotropy is also expected in other mechanical properties, as fracture toughness. However, experimental information on this parameter as a function of crystal orientation does not exist in the open literature. Hence, one of the aims of this thesis is to establish a correlation between crystallographic orientation of the carbides and the anisotropy of properties such as hardness and fracture toughness. These correlations would permit to be understood in terms of observed crack-microstructure interactions in WC-Co cemented carbides.

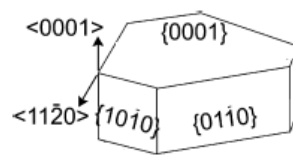


Figure 2.3.-Morphology of WC grains in WC-Co alloys showing the (0001) basal and $\{10\text{-}10\}$ prismatic facets.

Table 2.2 shows the chemical composition and hardness of the hardmetals studied in this work.

Table 2.2.-Chemical composition and hardness of the hardmetals studied

	WC	K-30 B	RESINTERIZED	GD13
WC (in wt %)	91.5	94.0	88.7	90
Co (in wt %)	8.5	6.0	11.3	10
Mean grain size (μm)	20.0	5	up to 30	1.2
Hardness (HV)	1050	1242	1140	1540

2.1.2. Al-Si Cast Alloy

Al-Si alloys are widely used in different engineering applications.. Al-Si binary alloy is a eutectic system with the eutectic composition at 12.6 wt% (Figure 2.4). Silicon reduces the thermal expansion coefficient, increases corrosion and wear resistance, and improves casting and machining characteristics of the alloy. When the Al-Si alloy solidifies, according to the silicon content either the primary aluminium forms and grows in dendrites or silicon phase forms and grows in angular primary particles. When the eutectic point is reached the eutectic Al-Si phases nucleate and grow until the end of solidification. At room temperature, hypoeutectic alloys consist of a soft and ductile primary aluminium phase and a hard brittle eutectic constituent. Hypereutectic alloys usually contain coarse, angular primary silicon particles as well as the eutectic constituent. These hard Si particles are exposed on the surface to bear the load, prevent adhesion of counter face materials to the Al matrix, and resist wear damage.

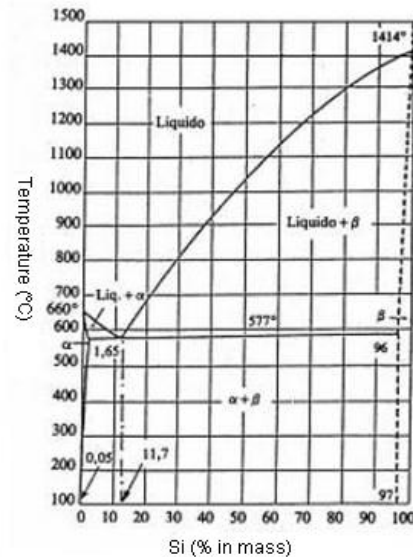


Figure 2.4.- Al-Si phase diagram.

Chemical composition of the studied Al-Si hypereutectic alloy is shown in Table 2.3. It was chosen because Si needles are big enough to fit an indentation impression and the cracks generated. Taking advantage of studying two Si single crystals with different crystallographic orientation, Si (100) and Si (111), and the silicon of Al-Si alloy, there is the possibility to study fracture behaviour of silicon and its anisotropy with and without a surrounding softer matrix. Nevertheless, when comparing results it should be taken into account the different casting processes of Al-Si alloys and Si single crystals. Thus, the Si on Al-Si alloy could be affected by porosity or the presence of metallic impurities among other effects.

Table 2.3.-Chemical composition of the studied Al-Si alloy (in wt%).

	Al	Si
Al-Si alloy	33.4 ± 0.9	66.6 ± 0.9

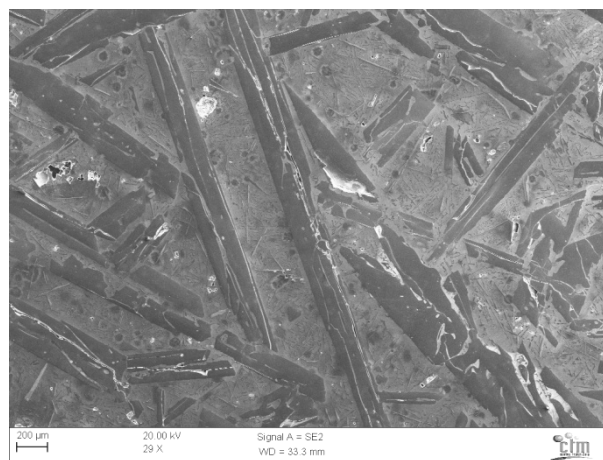


Figure 2.5.- Microstructure of the Al-Si alloy analysed.

2.1.3. Tool steels

Tool steel is a generic term applied to a wide range of steels, with carbon content between 0.7% and 1.5%, that after quenching and tempering gives high hardness and enables to use it to build forming tools. Forming tools for either hot or cold work include as die blocks and inserts, hot-forging machine tools, press-forming tools, deep-drawing tools, cold-heading dies and punches, thread-rolling dies, and extrusion tools. Such tools are in sliding contact with solids metal parts for a portion of their working life and may be subject to high stresses for short periods of time during operation. Thus, their principal requirement is wear resistance; secondary requirements include toughness and machinability. Forming tools used for hot work have the additional requirement of hot hardness. These materials also cover a broad range of compositions, from plain carbon to very highly alloyed high-speed steels.

Tool steels studied in this work are wrought and cast steels of high alloy and high carbon content used for cold work. These materials are composed of metallic carbides embedded in a soft matrix (Figure 2.6). These carbides are more or less evenly distributed in the steel mass with high volume content (about 20%). The tool steels studied present a considerable portion of retained austenite although achieve hardness values after quenching of about 63 HRC. Once quenched and annealed they possess good wear resistance and high compressive strength.

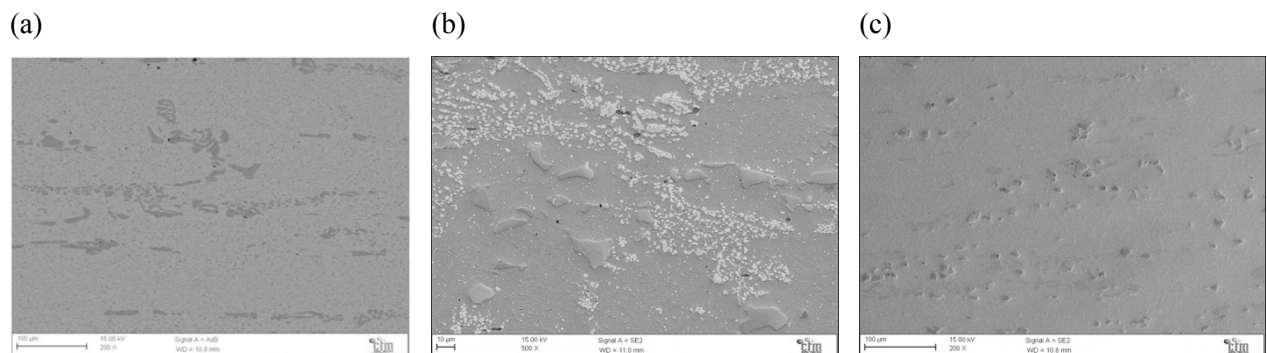


Figure 2.6.- Microstructure of (a) 1.2379 tool steel, (b) CAST WRA 46 tool steel and (c) UNIVERSAL tool steel.

The study is focused on the primary carbides of different tool steels in which a micromechanical characterization of these micro-sized phases was performed in order to evaluate their H , E and K_c . The studied steels were a conventional high chromium-high carbon tool steel, with denomination 1.2379, CAST WRA 46 and UNIVERSAL (Figure 2.6). Chemical compositions of these steels are shown in Table 2.4. Table 2.5 details the heat treatment schedule along with the obtained hardness (HRC) for each steel.

Table 2.4.-Chemical composition of the studied steels (in wt.%).

Steel	C	Cr	Mo	V	Si	Mn	W
1.2379	1.5-1.6	11.0-12.0	0.6-0.8	0.9-1.0	–	–	–
CAST WRA 46	1.25-1.40	4.00-4.75	0.20-0.40	3.9-4.50	0.20-0.40	0.20-0.40	5.25-6.5
UNIVERSAL	0.9-1.2	6.5-8.5	–	2.5-3.0	–	–	1.1-1.4

Table 2.5.-Heat treatments applied to the studied steels and obtained hardness

Steel	Austenizing (quench in oil)	Tempering	HRC
1.2379	1050°C for 30 min	530°C for 2h (x2)	61.0 ± 0.5
CAST WRA 46	1210°C for 4 min	560°C 2h (x3)	62.5 ± 0.1
UNIVERSAL	1070°C for 30 min	520°C 2h (x3)	61.0 ± 0.5

As carbide orientation strongly affects the properties of the tool steels, samples were extracted with the same carbide orientation, that is, parallel to the rolling direction. The chemical composition of the carbides was evaluated by energy-dispersive X-ray microanalysis (EDAX) and is shown in Table 2.6. In spite of the existence of some equipment limitations, a proper calibration of EDAX with a well known material made possible to estimate the stoichiometry of primary metallic carbides. The size of the metallic carbides was up to 11 μm so that they were big enough for indentation impressions and crack generated were fully contained in the carbide particles.

Table 2.6.-Chemical composition of the metal part of carbides (in wt%).

Steel	Carbide	Fe	Cr	V	Mo	W
1.2379	M_7C_3	40-45	46-51	6.0-6.5	2-3	–
CAST WRA 46	MC	2.27	–	68.5	6.0	8.6
CAST WRA 46	M_cC	34.3	7.3	2.9	24.3	26.8
UNIVERSAL	M_cC_c	40.0	38.4	7.7	3.3	2.2
UNIVERSAL	MC	1.9	10.8	61.3	3.8	4.0

2.2. Mechanical characterization

Mechanical characterization of the samples was carried with a conventional hardness test for Vickers indentations and with instrumented indentation for Berkovich and cube-corner indentations.

2.2.1. Conventional hardness test

A particularly meaningful quantity in indentation hardness is the mean contact pressure of the contact, and is found by dividing the indenter load by the projected area of the contact. The mean contact pressure, when determined under conditions of a fully developed plastic zone, is taken to be the indentation hardness, H , of the specimen material. Conventional hardness tests are generally made with either spherical (Brinell test) or pyramidal (Vickers test) indenters.

The mean contact pressure, and, hence, indentation hardness, for an impression made with a spherical indenter is given by:

$$p_m = H = \frac{4P}{\pi d^2} \quad (2.1)$$

where d is the diameter of the contact circle at full load (assumed to be equal to the diameter of the residual impression in the surface). The mean contact pressure determined in this way is often called the Meyer hardness in contrast to the Brinell hardness number (BHN), which uses the actual area of the curved surface of the impression and is given by:

$$BHN = \frac{2P}{\pi D(D - \sqrt{D^2 - d^2})} \quad (2.2)$$

where D is the diameter of the indenter. The Brinell hardness is usually performed at a value for a/R (the indentation strain) of 0.4, a value found to be consistent with a fully developed plastic zone.

For a Vickers diamond indenter (a square pyramid with opposite faces at an angle of 136° and edges at 148°), the Vickers hardness (HV) is found from:

$$HV = \frac{2P}{d^2} \sin \frac{136^\circ}{2} = 1.86 \frac{P}{d^2} \quad (2.3)$$

with d equal to the length of the diagonal measured from corner to corner on the residual impression in the specimen surface. The mean contact pressure is found using the projected area of contact:

$$p_m = 2 \frac{P}{d^2} \quad (2.4)$$

The Berkovich indenter (three-sided pyramid) is generally used in small scale indentation studies and has the advantage that the edges of the pyramid are more easily constructed to meet at a single point, rather than the inevitable line that occurs in the four-sided Vickers pyramid. The face angle of the Berkovich indenter commonly used for nanoindentation tests is 65.3° , which gives the same projected area-to-depth ratio as the Vickers indenter.

There is an important distinction to be made between conventional definitions of hardness and the hardness obtained by nanoindentation using depth sensing measurements. In conventional hardness test, such as the Brinell test, the size of the residual impression in the surface is used to determine the area of contact and hence the hardness value. In depth-sensing indentation tests, such as in nanoindentation, the size of the contact area under full load is determined from the depth of penetration of the indenter and the shape of the elastic recovery during the removal of load. Usually, the area given by the shape of the residual impression and that given by the depth-sensing technique are almost identical, but this is not always the case. A highly elastic material may give a very small residual impression after unloading while giving an appreciable contact area under load, if the former area is used the hardness will be higher than if the latter is used..

2.2.2. Instrumented indentation

In addition to conventional hardness testing, instrumented indentation experiments were performed to obtain in situ recording of applied load (P)-penetration depth (h_s) curves. The instrumented indentation technique captures the progress with time of the evolution of the contact response of the specimen. The equipment used to perform the tests was a Nanoindenter XP (MTS) (Figure 2.7) with the following technical features:

- Maximum applied load: 10 N, with a resolution of 50 nN.
- Displacement in Z axis of the tip: resolution of 0.02 nm.
- Position precision of the indentation in XY plane: 0.5 μm .
- Mode of operation: CSM mode (Continuous Stiffness Measurement) and Basic Mode.



Figure 2.7.- Image of the Nanoindenter used, Nanoindenter XP (MTS).

A schematic of the instrumented indentation device is depicted in Figure 2.8. The vertical displacement of the crosshead (A) induces the penetration of indenter (B) into specimen (C). Measurement of penetration depth, h_s , is performed with respect to the surface of the material using three-legged reference table (D). A capacitive sensor (E) is employed in such measurements of h_s .

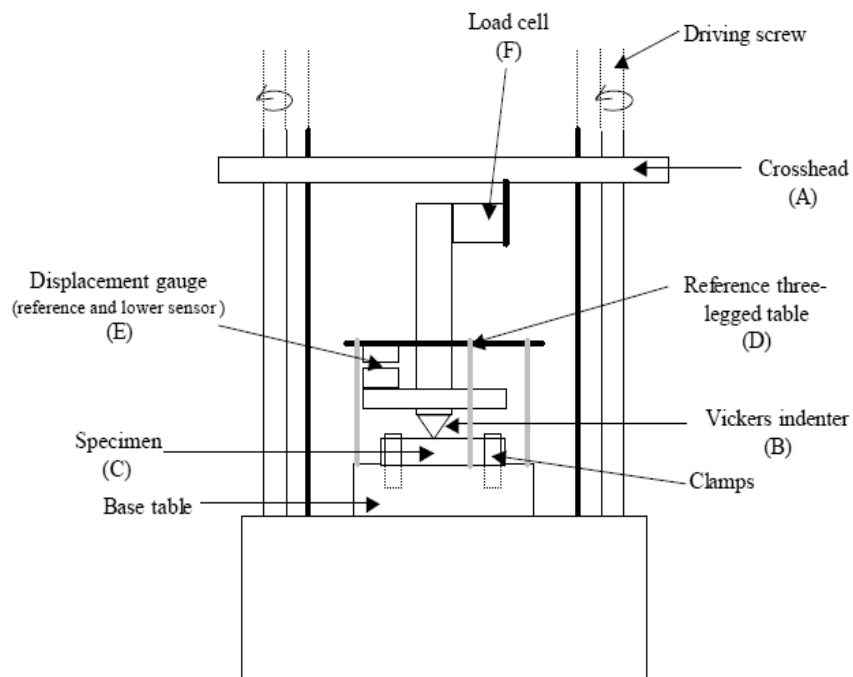


Figure 2.8.-Scheme of the instruments indentation device.

The $P-h_s$ curves were corrected for machine compliance to obtain accurate measurements of penetration depth [6, 7]. One of the most important parts of the instrumented indentation system is the probe tip. Nowadays, several indenters are made of a variety of materials. Diamond is probably the most frequently used material because its high H and E minimize the indenter deformation. Indenters can be

made of other less-stiff materials, such as sapphire, tungsten carbide, or hardened steel. Attending to their shape, indenters can be classified in four different groups:

- *Pyramidal indenters*: the most used sharp indenter in nanoindentation technique is the Berkovich indenter. It is a three-sided pyramid with the same depth-to-area relation as the four-sided Vickers pyramid commonly used in microhardness work. This indenter allows obtaining H and E . The toughness (K_c) of brittle materials can also be determined with a Berkovich tip indenter.
- *Spherical indenters*: for spherical indenters the contact stress is initially small and produces only elastic deformation. As the spherical indenter is driven into the surface, a transition from elastic-to-plastic deformation occurs, which can theoretically be used to examine yielding and work hardening, and to obtain the entire stress-strain curve. The spherical indenter can be used when one wishes to take advantages of the continuously changing strain. In principle, elastic modulus, yield stress, and strain-hardening behaviour of a material can be determined all in one test.
- *Cube-corner indenters*: a three-sided pyramid with mutually perpendicular faces arranged in geometry like the corner of a cube. The centre-line-to-face angle for this indenter is 34.3° whereas for the Berkovich indenter is 65.3° . The sharper cube-corner produces much higher stress and strain in the vicinity of the contact, which is useful in producing very small, well defined cracks around residual impression in brittle materials; such cracks can be used to estimate K_c at small scales.
- *Conical indenters*: the conical indenter is interesting due to the non existence of stress concentrations at the sharp edges of the indenter. It is difficult to manufacture conical diamonds with sharp tips, making them of little use in nanoindentation technique.

The indenters most frequently used in nanoindentation are the Berkovich and spherical tip indenters. Both allow characterizing the plastic, elastic, and the elasto-plastic deformation range.

On the other hand, the most important factors that can be controlled in a nanoindentation test are:

- *Choosing an appropriate indenter*: this step requires considering a number of factors. One consideration is the strain the tip imposes on the test materials. Although the indentation process produces a complex strain field beneath the indenter, it has been proven to be useful to quantify this field with a single quantity, often termed the characteristic strain. There are problems, however, in obtaining accurate measurements of H and E with cube-corner indenters [26]. Although not entirely understood, there are two main difficulties: firstly, as the angle of the indenter decreases, friction in the specimen-indenter interface and its influence on the contact mechanics becomes increasingly important; secondly, to obtain the relation between contact stiffness (S), contact area ($A(h_c)$) and

effective or reduced Young's modulus (E_{eff}) corrections are required, and the magnitude of the correction factor depends on the angle of the indenter.

- *Environmental control*: to take full advantage of the fine displacement resolution available in most IIT systems, several precautions must be taken with the testing environment. Uncertainties and mistakes in measured displacement arise from two separate environmental sources: vibration and variation in temperature. To minimize vibration, testing system should be located on quite, solid foundation and mounted on vibration-isolation system. Thermal stability can be provided by enclosing the testing apparatus in a thermally buffer cabin and controlling room temperature to within ± 0.5 °C.
- *Surface preparation*: mechanical properties are obtained from the measured contact depth and area function. Thus, control of the surface roughness of the samples is extremely important during nanoindentation tests because the contact area, from which the area function is computed, depends on the measured displacements.
- *Testing procedure*: to avoid interference from previous tests, and ensure the independence of the measurements, successive indentations should be separated up to 20 to 30 times the maximum penetration depth (h_{max}) when Berkovich or Vickers indenters are employed. For other geometries, the rule is to perform indentation separated from 7 to 10 times the maximum contact radius.
- *Detecting the surface*: the most important part of any good nanoindentation test procedure is an accurate identification of the location of the specimen's surface. For hard and stiff materials, such as hardened metals and ceramics, the load and/or contact stiffness, both of which increase upon contact, are often employed. However, for soft compliant materials (such as polymers and biological tissue), the rate of increase in load and contact stiffness is often too small to allow for accurate surface identification. In these situations, a better method is sometimes offered by dynamic stiffness measurement [27, 28].

2.3. Residual imprint characterization

2.3.1. Field Emission Scanning Electron Microscopy, FE-SEM

SEM provides information on surface topography, crystalline structure, chemical composition, and electrical behaviour of the top of the surface of a specimen. The electron beam interacts with the surface material, causing a variety of signals: secondary electrons, backscattered electrons, X-Ray, Auger electrons, cathodoluminescence. In this work secondary electrons were used in order to inspect all the residual imprints, measure the size of the contact impression, and the lengths of the cracks emanating

from its corners. Also X-Ray photons were used in order to chemically characterize the carbides in tool steels. Furthermore, using an EBSD detector coupled to the FE-SEM, crystal orientation of each tested WC grains in hardmetal samples, and crystal orientation of Si needles in Al-Si alloy were assessed. A scheme diagram of typical FE-SEM is given in Figure 2.9.

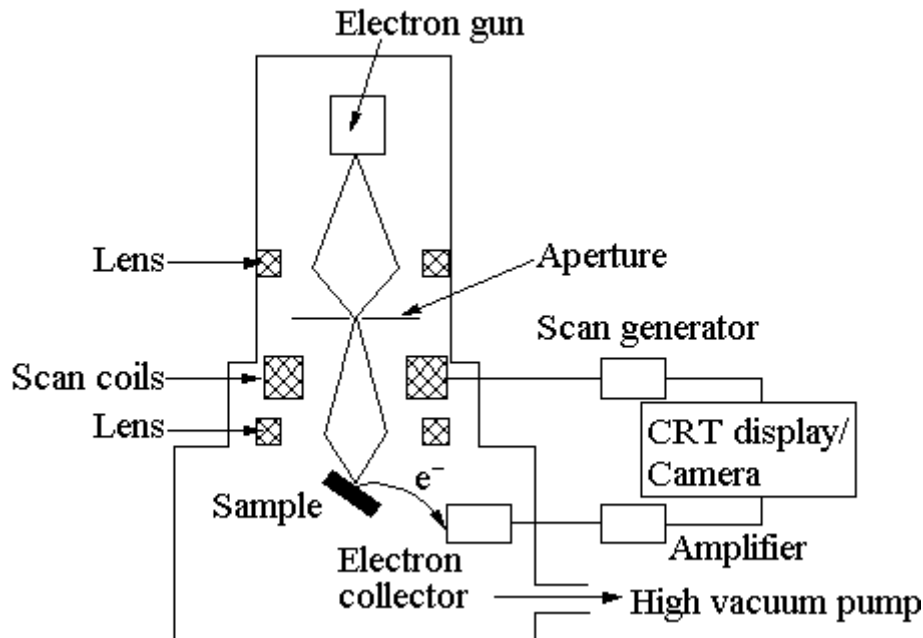


Figure 2.9.- Scheme diagram of typical FE-SEM.

A field-emission cathode in the electron gun of a scanning electron microscope provides narrower probing beams at low as well as high electron energy, resulting in both improved spatial resolution and minimized sample charging and damage. Under vacuum, electrons generated by a FE-SEM are accelerated in a field gradient. The beam passes through electromagnetic lenses, focusing onto the specimen. As a result of this bombardment, different types of electrons are obtained, and an image of the sample surface is constructed by comparing the intensity of these secondary electrons to the scanning primary electron beam. Finally, the resulting image is displayed on a monitor.

SEM images were obtained by a Zeiss Ultra Plus equipment under different conditions depending on the sample. It was not necessary coating ceramic samples with a thin conductive layer because the equipment has a local compensation system for non conductive samples. In EBSD tests the scan was carried out with an acceleration voltage of 15-20 kV, a working distance of 10.5-12.5 mm, a detector distance of 174 mm, scanning a field corresponding to a magnification of x400 with a step size of 1-0.4 μm for Al-Si and hardmetal samples respectively. The EBSD detector (brand hkl) uses the “Chanel 5” software suit for data acquisition and processing.

2.3.2. Focused Ion Beam, FIB

Focused ion beam (FIB) is a special SEM using a gallium Liquid Metal Ion Source (LMIS) instead of a focused beam of electrons to image the sample (Figure 2.10). In a Gallium LMIS, gallium metal is placed in contact with a tungsten needle and heated. A large electric field causes ionization and field emission of the gallium atoms. These ions are then accelerated and focused onto the sample by a set of electromagnetic lenses. Unlike the electron microscope, the FIB is inherently destructive for the specimen. When the high-energy gallium ions strike the sample, they will sputter atoms from the surface. Gallium atoms will also be implanted into the top few nanometers of the surface thus creating an amorphous layer. Applications of the FIB ranges from micro-machining to deposition of metal layers through Chemical Vapor Deposition (CVD) and also TEM lamella preparation.

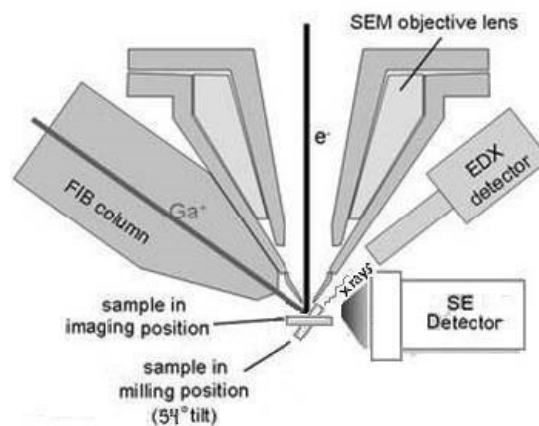


Figure 2.10.-Scheme diagram of a typical FIB-SEM.

FIB was used to study the crack morphology induced by cube-corner tip in soda-lime glass, Si (100), SiC-6H (0001), WC in hardmetal and carbides of 1.2379 and UNIVERSAL tool steels. FIB images were obtained by a Zeiss 40 equipment of the Centre de Recerca de Nanoenginyeria of the Universitat Politècnica de Catalunya (CRnE-UPC) at 30 KeV and 200-500 pA depending on the material. SEM images were taken every 2, 3, 4 o 5 sections, depending on the imprint size and the material analysed.

2.3.3. Sequential polishing technique

In order to analyse crack morphologies, FIB would be the proper technique due to its accuracy in the measurements. Nevertheless, there are accessibility limitations in its use, thus sequential polishing was taken as an alternative technique for evaluation of the crack morphology.

All the samples were sequentially polished under appropriate conditions for each type of materials. In order to control the amount of removed material fine abrasive powders such as alumina or diamond suspensions up to 9 μm were used. Because the samples were observed by SEM a good surface finishing was needed, thus, the final polishing step was carried out by colloidal silica suspension of 0.04 μm

In order to control the amount of removed material, a Vickers microindentation was done as a control imprint. Knowing the geometry of a four sided Vickers pyramid, the diagonal of this control imprint can be used to evaluate its penetration depth in each polishing step through the following equations:

$$\begin{aligned} h &= \frac{a}{2} (\tan 68)^{-1} \\ a &= \frac{1}{2} (d_1^2 + d_2^2)^{1/2} \end{aligned} \quad (2.5)$$

where h is the penetration depth of the residual imprint, a is the length side and d_1 and d_2 are the imprint diagonals.

During sequential polishing it has been taken into account that most ceramics present stress-corrosion cracking (SCC) that is, a sub-critical crack growth by the combined and synergistic interaction of mechanical stress and corrosion reaction. The term SCC is frequently used to describe any type of environmentally induced or assisted crack propagation. In oxides such as silica (SiO_2) and alumina (Al_2O_3), there is a direct reaction between the water molecule and the solid that produces a transfer of the proton of the water molecule to the solid.

In some materials, cracks induced by sharp indenters may propagate under sequential polishing in presence of water due to the residual stresses generated during the indentation process. In order to avoid such SCC effect on glass and ceramic polished samples, alumina powder dissolved with ethanol was used. On the other hand, diamond suspension was used to polish metallic samples in which SCC effects induced by the polishing materials have been not reported.

As the amount of removed material was increased, the crack became thinner doing its detection by SEM more difficult. In order to reveal the crack, anhydrofluoric acid was used in the final polishing steps to etch the crack. With this controlled etching, the thinner cracks were revealed doing its monitoring by SEM possible.

2.3.4. Crack morphology identification

Once the crack morphology is revealed either by means of FIB or sequential polishing, it should be identified as one of the typical crack system observed during sharp indentation: Palmqvist - radial cracks (see Figure 1.8b), median - radial cracks or half-penny cracks (see Figure 1.8d). The main characteristics of these crack morphologies are the following ones:

2.3.5. Atomic Force Microscopy, AFM

Atomic force microscopy (AFM) is a very high-resolution microscope that forms images of surfaces using a physical probe that scans the specimen. The AFM uses very sharp tips, often less than 10 nm diameter, mounted on a cantilever to scan the surface of a sample. As the tip traverses the surface, attractive and repulsive forces arising between the atoms on the surface and the tip induce forces on the probe that bend the cantilever. The amount of bending is measured and recorded, providing a map of the surface. Atomic force microscopes can achieve magnification factors of 5×10^6 , with a resolution of 0.2 nm.

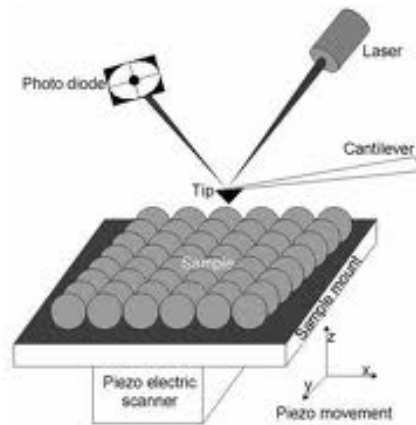


Figure 2.11.-Scheme diagram of a typical AFM.

AFM images were obtained by AFM Dimension 3100 (Veeco) in CRnE-UPC. AFM measurements were performed in order to evaluate the crack opening displacement from which K_c will be computed using equation (1.30) as an alternative method to the IM.

**Influence of crack morphology on nanoindentation
fracture toughness**

If you want to learn about nature, to appreciate nature,
it is necessary to understand the language that she speaks in.

Richard Feynman (1965)

The IM method was developed for four-sided Vickers pyramids; however, Berkovich and cube corner indenters are generally used in nanoindentation. Thus, it is necessary to check the applicability of the existing fracture toughness equations to nanoindentation. The application of IM by nanoindentation is highly interesting to extract mechanical properties of small volumes as thin films or micro-sized hard particles because offers the possibility to evaluate thoroughly H , E , K_c and the residual stresses in one single test. It has been observed that sharper indenters, as cube-corner, displace a much larger volume of material for a given load than a Berkovich tip (more than three times) producing higher stresses beneath the indenter [29, 30]. Hence, cracks with cube corner tip can be generated at lower loads than those used for Berkovich indenters, which allows characterizing even smaller material volumes [13, 15, 30]. Since the use of cube-corner indenters is highly interesting from a micromechanical point of view, the applicability of the equations for computing K_c when a cube-corner is used is studied in this chapter.

Over the years, different fracture toughness equations have been empirically developed. These equations are mainly based on two factors:

- Theoretical assumptions related with the stress fields generated by sharp indenters.
- Crack morphology system generated by sharp indenters.

Thus, in order to choose the most appropriate equation to compute K_c by means of nanoindentation, it is important to know which kind of crack system is generated by three-sided pyramids (Berkovich and cube-corner indenters). In this manner, in this chapter crack morphologies generated by different tip geometries and their influence on fracture toughness equations are studied.

The experimental observations on the fracture sequence in brittle materials made by Cook and Pharr show that at least radial (and median when observed) crack systems align themselves with the symmetry of the indenter [16]. Accordingly, Vickers and Berkovich/cube-corners indenters are likely to generate different crack morphology systems. While the half-penny morphology, with cracks connected underneath the hardness impression, is the most common morphology for brittle materials when a Vickers indenter is used, Palmqvist cracks are developed at low indentation loads or in high-toughness materials whatever the indenter is used. Transition between both crack configurations takes place when the indentation load is increased. Therefore, the final indentation crack morphology will depend on the indentation load, the tip geometry and the material toughness.

3.1. Crack morphology evaluation

In this section crack morphology generated by three different tip geometries, Vickers, Berkovich and cube-corner are studied. Crack morphology sequence and fracture toughness of soda-lime glass have been widely studied because its transparency helps to easily monitoring the crack sequence, and is also an accessible and cheap material. Consequently this material was the first one to be studied in this work.

Nevertheless, it has been experimentally observed that indentation cracks in soda-lime glass are very different from the majority of brittle materials, in both morphology and sequence, due to its low E/H ratio [16]. Taking into account this setback, soda-lime glass was chosen to prove that crack morphology depends on the geometrical symmetry of the indenter used. Vickers and Berkovich tips were used at the same indentation load and the results were carefully studied and compared. Moreover, further observations and conclusions related with crack morphologies generated by three-sided sharp indenters were also made using different single crystals.

From the crack morphology sequence obtained using Vickers and Berkovich tips onto a soda-lime glass sample it can be observed that (see Figure 3.1 and Figure 3.2).

- i. There is chipping around the imprints (see Figure 3.1e and 3.1f). This effect could be due to either the emergence of lateral cracks to the surface during polishing [31] or as a consequence of the hydrofluoric acid etching that could act as a crack opener. The chipping observed could also be a consequence of the combination of the two former effects.
- ii. It can be observed that the crack morphology generated by a Vickers indenter is indeed half-penny, i.e., a semi-circle crack that joint beneath the hardness impression. Whereas the crack morphology generated by a Berkovich indenter is semi-elliptical. Additionally, lateral cracks were also present. Hence, at the same applied load a symmetrical four-sided Vickers indenter pyramid generates different crack morphology than a non-symmetrical three-sided Berkovich indenter pyramid.
- iii. In both crack morphologies, a plastic zone was also observed. Within this plastic zone, which is a characteristic of an elasto-plastic sharp indentation, compressive stresses prevail during the indentation cycle and cracks cannot grow into this zone. Thus, to achieve the final crack morphology, the induced plastic zone must be totally removed (see Figure 3.1g and Figure 3.2g).

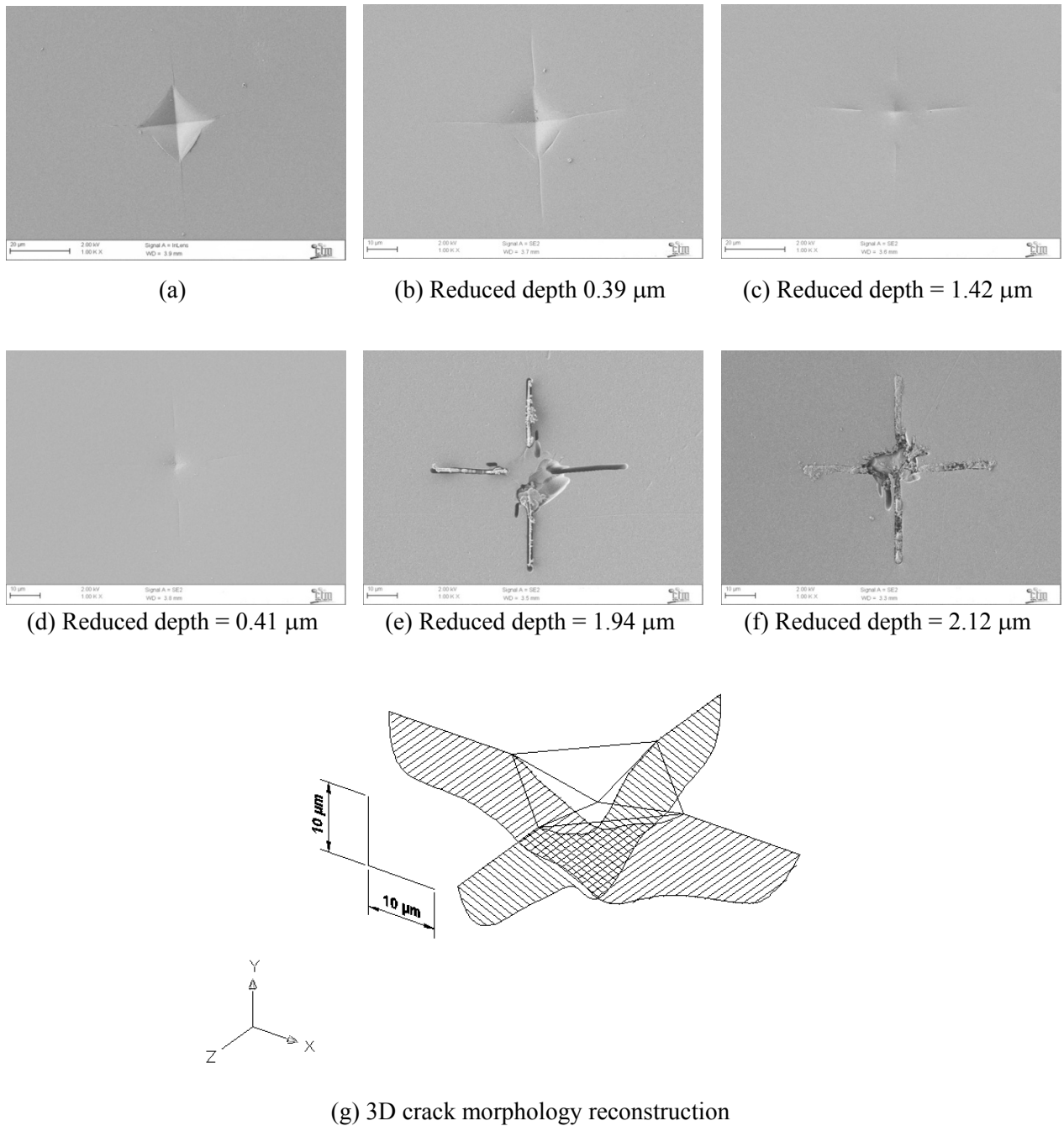


Figure 3.1.—Crack evolution SEM images of a Vickers indentation in soda-lime glass at 2 N using the sequential polishing technique (a, b, c, d, e, f). In the final steps and 5% HF etching has been applied (e, f) and (g) shows the 3D crack morphology reconstruction.

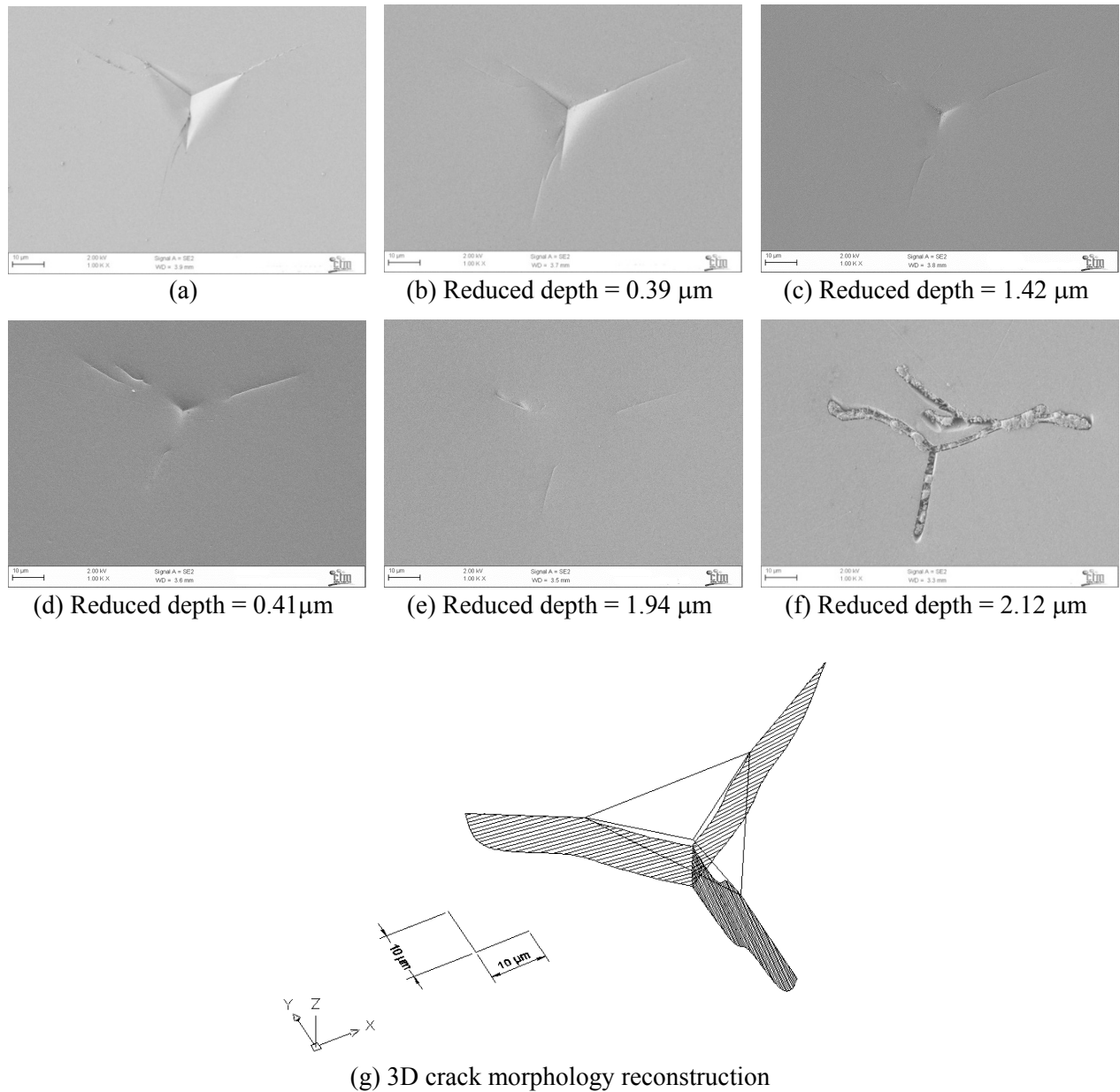


Figure 3.2.—Crack evolution SEM images of a Berkovich indentation in soda-lime glass at 2 N using the sequential polishing technique (a, b, c, d, e, f). In the final steps and 5% HF etching has been applied (e, f) and (g) shows the 3D crack morphology reconstruction.

From the aforementioned results, it was proved that the tip geometry has an important influence in the crack morphology and for Berkovich indenters the typical Palmqvist crack is not observed.

With reference to cube-corner indentation Figure 3.3 shows a FIB tomography image at 5, 10, 20, 50 and 100 mN performed in soda-lime glass. In addition, Figure 3.4 shows a cube-corner indentation in Si (100) at 20 mN whereas Figure 3.5 shows a cube-corner indentation in SiC-6H (0001) at 50 mN. The reason to extend the study to crystalline materials that one of the aims of this work is to extend the

knowledge of fracture toughness evaluation by means of Berkovich and cube-corner indenters to small hard crystalline particles.

In Figure 3.3 it can be observed that as the load is increased the length of the crack at the surface increases and lateral cracks appear. The increasing in surface crack length with the applied load alters the crack morphology from a semi-elliptical shape to a quarter-penny crack. The final dimensions of the indentation cracks are dominated by the residual stress field, if the residual stresses increases due to the increase in the applied load a change in the crack morphology is likely [29].

A comparison between the length measured by FIB tomography and SEM is shown in Table 3.1. It can be observed that there is a reasonable agreement between both values. However, FIB tomography induces local changes in the residual stress state of the material examined [32]. The reason is that by using FIB tomography it is necessary to perform a FIB trench, and the process of cutting relieves residual stresses at the new free surface. Thus, without the presence of residual stresses, existing cracks can open up; consequently, both crack length and the indentation plastic zone size could change. For that reason, in order to evaluate K_c , in this thesis crack length measurements by SEM have been used since reliable values than that measured by FIB are expected.

Additionally, FIB tomographies allow a direct measurement of crack surface and plastic zone. Since plastic zone radius is linked with yield stress, this parameter is useful in order to mechanically characterize the studied material. Otherwise, the compressive stresses are not practically relieved during the polishing steps [32]. Hence, it is likely to obtain a more reliable plastic zone size value with sequential polishing than by FIB tomography. Nevertheless, this is an interesting issue that will be discussed during the chapter.

Table 3.1.-Comparison of crack lengths measured by FIB and SEM in microns.

Tip geometry	P (mN)	$l_{\text{FIB}} (\mu\text{m})$	$l_{\text{SEM}} (\mu\text{m})$	$a_{\text{FIB}} (\mu\text{m})$	$a_{\text{SEM}} (\mu\text{m})$
Cube-corner	5	0.6 ± 0.1	–	0.73 ± 0.04	–
	10	1.2 ± 0.4	–	1.1 ± 0.1	–
	20	1.9 ± 0.1	1.6 ± 0.1	1.4 ± 0.1	1.47 ± 0.05
	50	4.0 ± 0.2	3.3 ± 0.2	2.2 ± 0.1	2.3 ± 0.1
	100	5.1 ± 0.7	6.4 ± 0.9	3.1 ± 0.4	3.3 ± 0.1

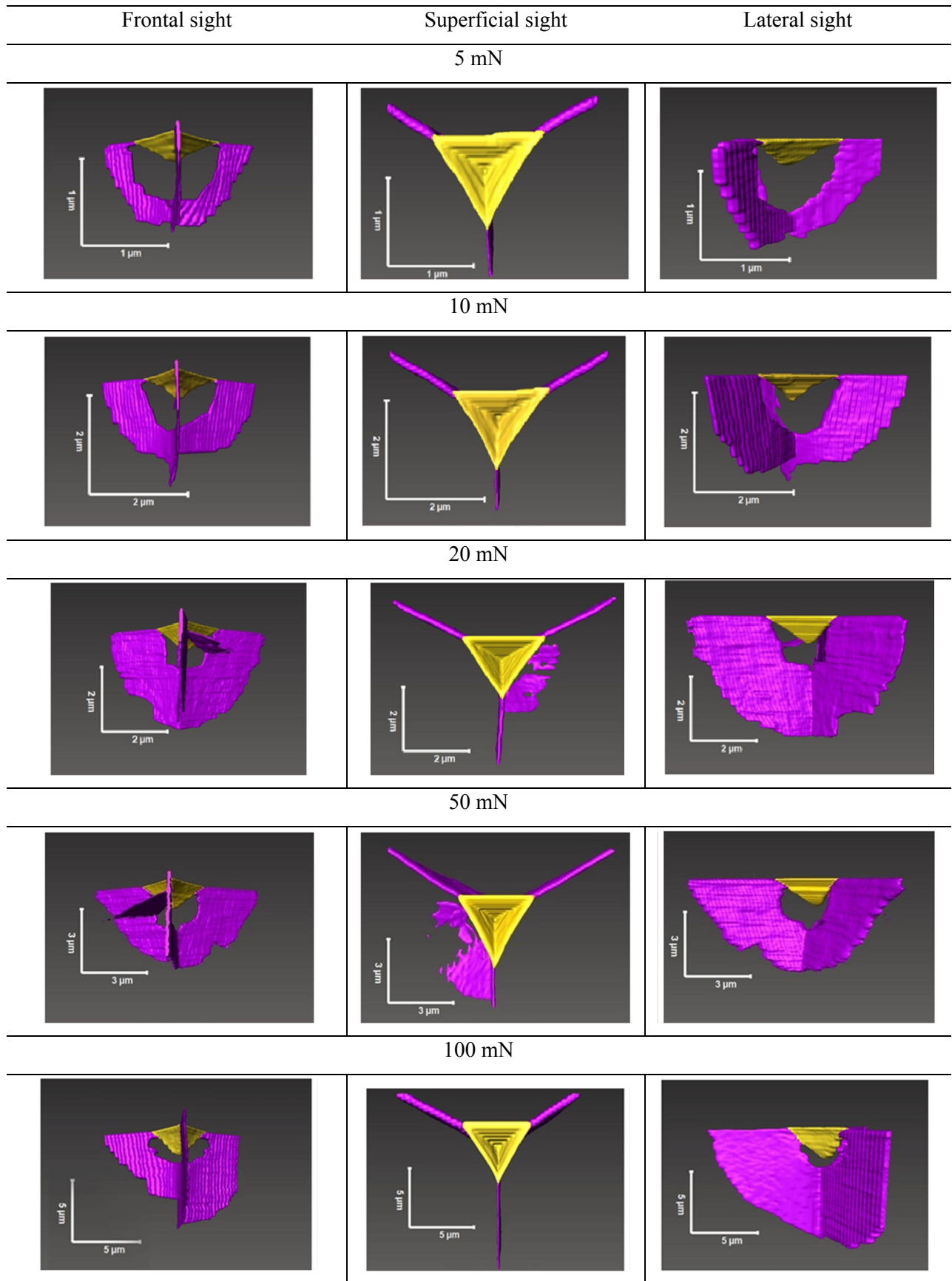


Figure 3.3.- Crack morphology system for a cube-corner indentation in soda-lime glass using FIB tomography at (a) 5 mN, (b) 10 mN, (c) 20 mN, (d) 50 mN and (e) 100 mN. Yellow area corresponds to the indentation impression, violet indicates the crack morphology.

When FIB tomography images are analysed for crystalline materials, it can be observed that Si (100) and SiC-6H (0001) present a more complicated crack system. Because of the crystallographic nature of Si (100) cracks are deviated following preferential directions whereas lateral cracks follow the stress field and are not influenced by the crystallographic orientation (Figure 3.4). In crystalline materials, anisotropic cleavage, plasticity and elastic modulus strongly influence the stress field around an indentation and subsequent cracking events.

Figure 3.5 shows that shallow lateral cracks are also formed. These crack deviations and extra crack systems could affect the K_c value obtained because of the extra energy spent in the process. Therefore, less energy is available for the extension of radial cracks so that it is likely they grow less. In addition, any of the existing equations for calculating K_c by means of IM do not take into account these effects. Nevertheless, K_c was computed idealizing the crack system to be radial cracks. For any of the single crystal studied, an ideally radial crack was never observed, only semi-elliptical cracks in the form of quarter-penny cracks. Thus, the effect of having a radial or a quarter-penny crack (both semi-elliptical but the radial crack located near the surface, while the quarter-penny crack initiated in the plastic zone boundary) in the K_c computation was studied. Besides, crystallographic effects on K_c computation were also studied in this investigation since, as observed in Figure 3.4 and Figure 3.5, it clearly affect the morphology and consequently the K_c computation.

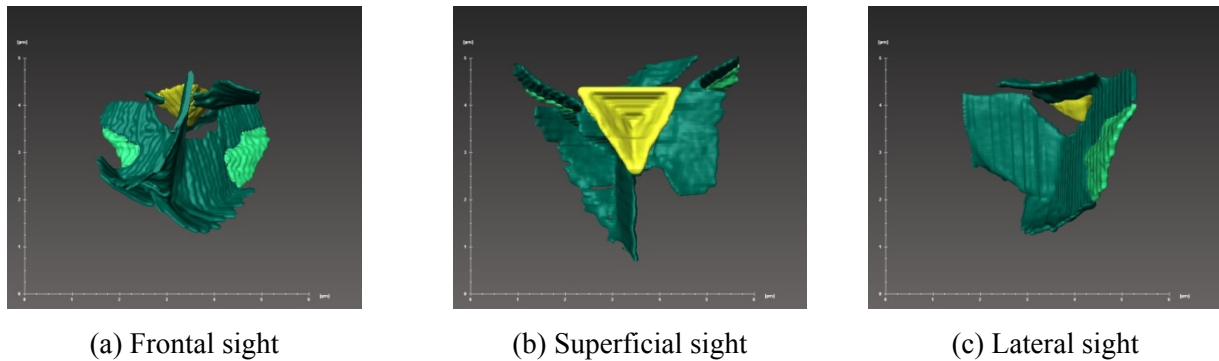


Figure 3.4.–Crack morphology of a cube-corner indentation in Si (100) at 20 mN using FIB tomography. Yellow area corresponds to the indentation impression, green indicates the crack morphology.

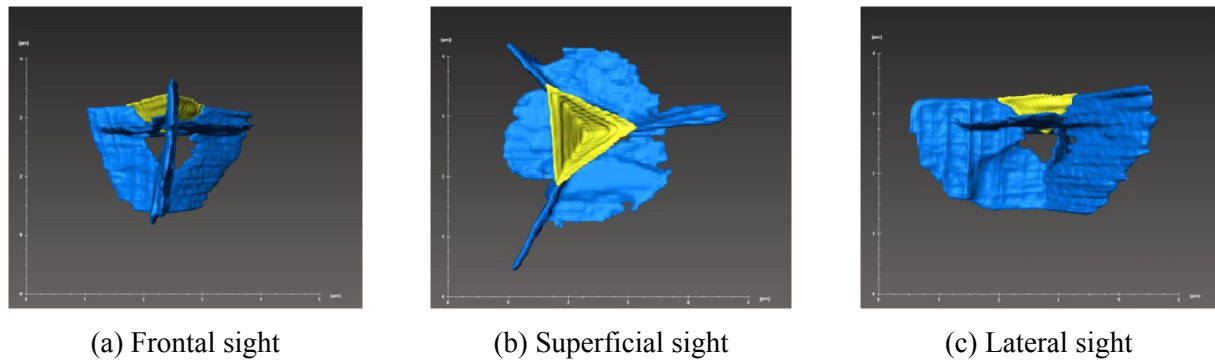


Figure 3.5.-Crack morphology of a cube-corner indentation in SiC-6H (0001) at 50 mN using FIB tomography. Yellow area corresponds to the indentation impression, blue indicates the crack morphology.

3.1.1. Crack morphology observations

One significant experimental observation in both glass and crystalline materials is that the plastic zone exhibits a hemispherical symmetry, as expected for brittle materials [29]. Chiang, Marshall and Evans (CME) analysis predicted that lateral cracking is dictated by the σ_{zz} stress at a distance beneath the surface of approximately half the plastic zone [29]. This behaviour is observed here when lateral cracks appear. The form of the stress field also predicts that radial and median cracking are dictated by the σ_{yy} stress component, as a consequence crack morphologies as that shown in Figure 1.8b and 1.8d are developed. This behaviour is also observed here when a sharp indenter is applied onto brittle materials.

Crack morphologies generated by Berkovich and cube-corner indenters (see Figure 3.1 to Figure 3.5) do not match completely with Palmqvist or half-penny crack configurations (see Figure 1.8b and 1.8d). Notwithstanding, cracks observed here are semi-elliptical without being radial cracks since they are not located near the surface but in the plastic zone boundary. Hence, the crack system observed can be depicted as quarter-penny cracks. These observations are in agreement with those made by Shiffmann [14] and Cook and Pharr [16] and with CME predictions [29]. Cook and Pharr's work showed that when a Vickers indenter is applied in a soda-lime glass at low loads radial cracks nucleate from flaws at the deformation zone boundary. Radial cracks are driven by the residual stress field arising from the strain mismatch of the plastically deformed zone embedded in the surrounding elastically restraining matrix (Figure 1.8b). Cook and Pharr observed that as the peak load increases, median cracks initiate beneath the deformation zone (Figure 1.8c). Median cracks are nucleated by flaws at the deformation zone boundary, but are driven by the stress field arising from the elastic loading of the indenter onto the surface. On unloading, the median cracks spread outward along the surface to leave half-penny geometry at complete unload, which wedge open by the residual field (Figure 1.8d). Cook and Pharr also observed that at high peak loads, lateral cracks are nucleated. In their work both crystalline materials and amorphous materials were studied. In all materials examined in which half-penny cracks were observed, they were formed by the coalescence beneath the contact impression of radial cracks. They concluded that half-penny

geometry was never directly produced; they were always formed by the coalescence beneath the contact impression of radial cracks. Thus toughness evaluation analyses based on radial rather than on half-penny geometry may be more appropriate for many brittle materials particularly at low loads. Furthermore, the corners of the indenters result in a localized elevation of the tangential stress during load application, encouraging the formation of radial cracks at these locations since they exhibit the lowest threshold load [29].

Experimental work developed in the present thesis has shown that crack morphology for the studied materials is in the form of three cracks emanating from the plastic zone boundary and spreading outward the surface. Additionally, depending on the indentation load and the tip geometry, lateral cracks are also present. These observations are in agreement with other recent works [14]. Thus, cracks generated by three-sided pyramid indenters (as Berkovich and cube-corner geometries) are semi-elliptical, instead of being semi-circular, which is the typical morphology for four-sided pyramid indenters (as Vickers geometry).

3.1.2. Crack morphology analysis from the $P-h_s$ nanoindentation curves

The experimental $P-h_s$ curves for the studied materials, soda-lime glass, Si (100) and SiC-6H (0001) are shown in Figure 3.6 for Vickers, Berkovich and cube-corner indenters. It can be observed that the pop-in excursions in the $P-h_s$ curves, which are typical of fracture of brittle materials, are not always detected; while pop-out events are often observed (Table 3.2 summarizes the pop-in and pop-out events observed during the $P-h_s$ curves).

Table 3.2. -Summary of the pop-in and pop-out events observed in the experimental $P-h_s$ curves.

Observed event	Soda-lime glass	Si (100)	SiC-6H (0001)
VICKERS INDENTER			
Pop-in	NO	NO	YES
Pop-out	NO	YES	NO
BERKOVICH TIP			
Pop-in	YES	YES	YES
Pop-out	NO	YES	NO
CUBE-CORNER TIP			
Pop-in	NO	NO	NO
Pop-out	NO	ONLY AT 20 mN	NO

Although fracture was always induced in the three studied materials, pop-in events were not always detected, mainly when Vickers indentations were performed onto soda-lime glass and Si (100) samples and when the cube-corner indenter was used. The lack of pop-in events in the soda-lime glass sample agrees with the observations made by Cook and Pharr. They observed that in contrast with crystalline materials which showed radial crack formation in the loading part of the indentation cycle, soda-lime glass exhibited no radial cracks on loading but they formed on the unloading step. On the other hand, the

observed pop-out events indicate either a change of volume in the material or the initiation of lateral cracks [16, 20, 33]. Pop-out events were only detected in Si (100) sample where an indentation phase transformation was induced, causing a change of volume in the material [34-36].

Nevertheless, since the fracture experiments were performed in load control other explanations for the absence of pop-in and pop-out events could be given as the equipment has a low sensitivity in the displacement channel in this control mode:

- i. The extra displacement caused during the fracture process was too small to be detected.
- ii. Data acquisition system is not fast enough to capture crack initiation and discern it from crack growth.

In fact, other studies agree with these observations. When larger loads are applied the P-h_s curves show discrete events during the indentation contact (pop-in events), indicating the formation and slippage of shear faults, whereas at small loads like that used in the nanoindentation range, these events are not usually observed using load-control mode [37].

On the other hand, an option for monitoring the fracture process during the indentation test is using coupling acoustic emission equipment. In this investigation it was not possible to have any acoustic emission equipment but it seems worthy to perform this kind of experiments as it could be helpful to understand the crack sequence in brittle materials.

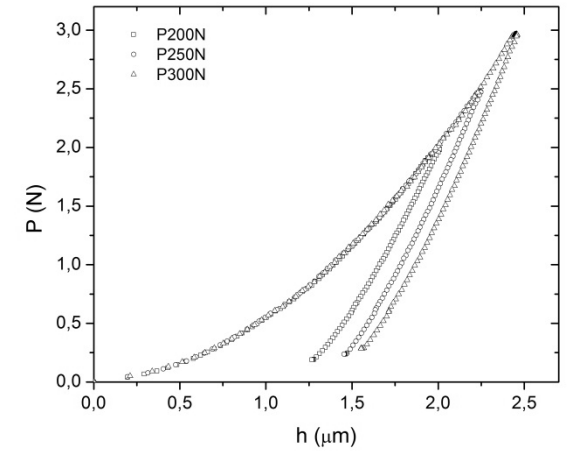
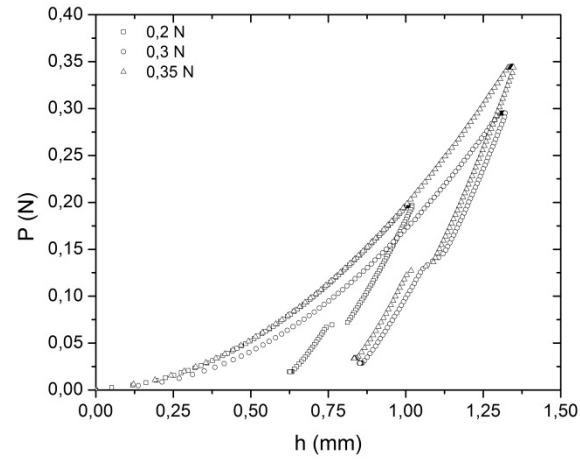
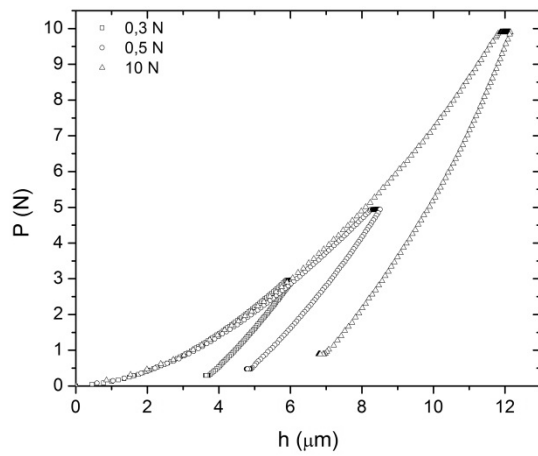
Tip

Soda-lime glass

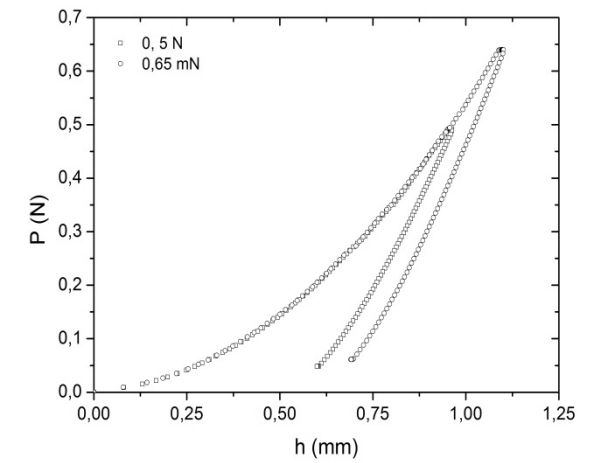
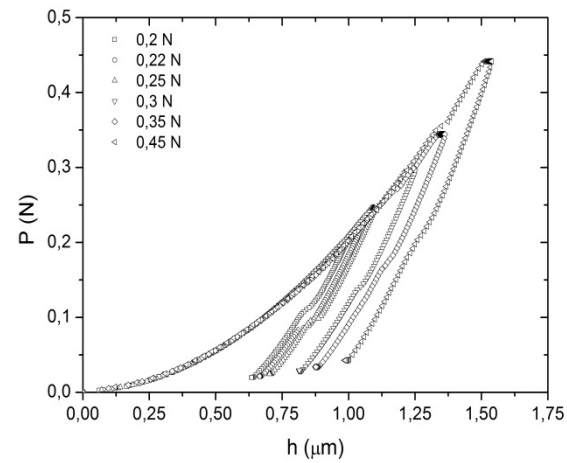
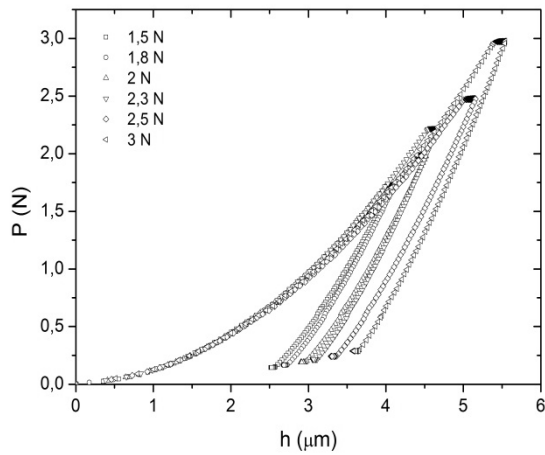
Si (100)

SiC-6H (0001)

Vickers



Berkovich



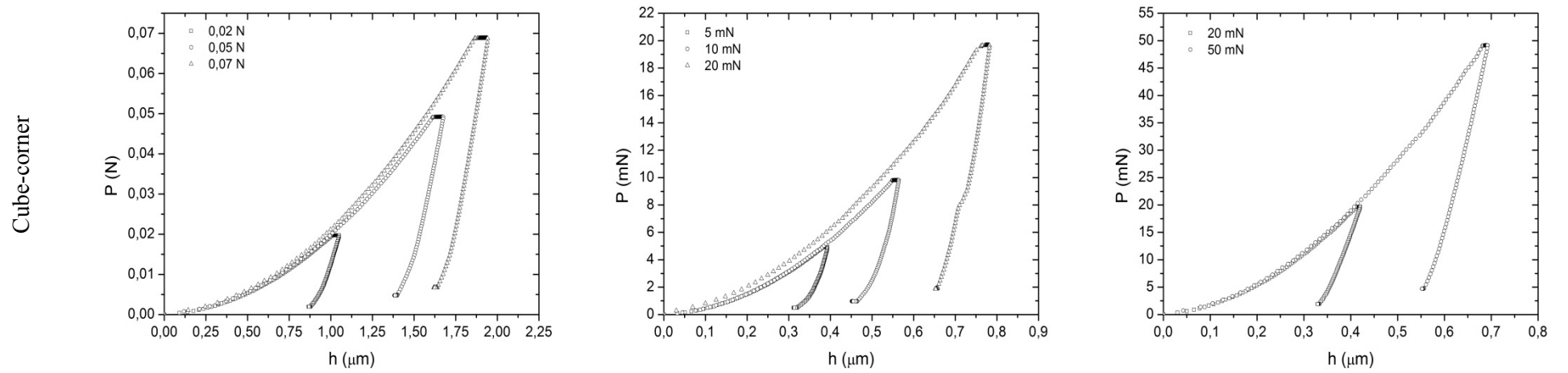


Figure 3.6.- Experimental $P-h_s$ curves for Vickers, Berkovich and cube-corner indenters and soda-lime glass, Si (100) and SIC-6H (0001) samples.

Even with the experimental difficulties encountered, using the information depicted by $P-h_c$ curves and crack morphology, the crack sequence for Berkovich and cube-corner indenters, seems to be as follows: radial cracks are formed during the load cycle and spread out during unloading cycle until Palmqvist or quarter-penny cracks are formed. Because of the triangular symmetry of the tips radial cracks cannot coalesce beneath the contact impression to form a half-penny as with Vickers indenters [16]. The transition between Palmqvist and quarter-penny cracks depends on the material fracture toughness; the crack morphology tends to be Palmqvist as K_c increases. Thus, as half-penny morphology was never achieved, the toughness evaluation analyses based on radial rather than on half-penny geometry may be more appropriate for many materials, particularly at low loads and in nanoindentation tests.

3.1.3. Indentation plastic zone size and crack morphology

A characteristic feature of indentation experiments is the development of a plastic zone, whose size increases during load application. Among other aspects, knowledge of the plastic zone size allows [38-41]

- i. Calculation of the yield strength.
- ii. Examination, within a continuum mechanics framework, of discrete deformation processes occurring at small loads.
- iii. Assessment of possible influence of substrate effects on the contact response of thin films and small-volume structures.

In addition, the shape of the plastic zone is indicative of the plastic flow features underneath the indenter. In this work the calculation of the yield strength is of interest since full mechanical characterization, in terms of hardness, Young's modulus, fracture toughness and yield strength, of the micro-sized particles analysed could be achieved.

Mechanistic interpretations of indentation experiments have long been based on the analogy between indentation and the expansion of a spherical cavity [1, 29]. This analogy provides useful relationships between contact parameters, such hardness and plastic zone size, and the elasto-plastic mechanical properties of the material. Two models that allow predicting the yield strength from the plastic zone size are analysed:

1) JOHNSON'S MODEL

$$\sigma_{ys} = \frac{E \tan \theta}{6(1-\nu)} \left[\left(\frac{c}{a} \right)^3 - \frac{2}{3} \left(\frac{1-2\nu}{1-\nu} \right) \right]^{-1} \quad (5.1)$$

2) CHIANG, MARSHALL, EVANS'S MODEL

$$\sigma_{ys} = \frac{E}{3(1-\nu)\beta^3 - 2(1-2\nu)} \quad (5.2)$$

where c is the plastic zone size, a is the radius of the imprint (which is equivalent to the radius of the spherical cavity), E is the Young's modulus, σ_{ys} is the yield strength, ν is the Poisson's ratio. In Johnson's model, θ is the angle between the indenter flank and the surface, and in Chiang, Marshall and Evans's model (CME's model) β is the relative indentation dimension defined as:

$$\beta = \frac{c}{\bar{a}} \left(\frac{\sqrt{2\pi}}{\cot \Psi} \right)^{1/3} \quad (5.3)$$

where $2\bar{a}$ is the indentation diagonal and 2Ψ is the included angle between opposite faces of the indenter pyramid.

Both Johnson and CME's models ignore strain hardening effects, as they are derived for elastic-perfectly plastic solids. Although both analysis are based on the Hill's solution for an expansion of a spherical cavity Johnson's models replaces the cavity by an incompressible hydrostatic core beneath the indentation and neglects the free surface present on an indentation experiment, whereas in CME's model the core has an explicit significance by its direct association with the indentation volume and takes into account the free surface.

Table 3.3.-Yield strength evaluation from Johnson's model and CME's model using the plastic zone size computed by FIB tomographies.

Material	σ_{ys} (GPa)		
	Johnson's model	CME's model	Literature
Soda-lime glass	8	8	2.8 [42]
Si (100)	28	29	8 [43]
SiC-6H (0001)	16	23	21 [44]

In order to attempt evaluating the yield strength from the indentation test, FIB tomographies were used to measure the plastic zone size of soda-lime glass, Si (100) and SiC-6H (0001) samples when cube-corner indenters are applied. Table 3.3 shows the yield strength computed using Johnson's model and CME's model, and the values found in the literature. It can be observed that both models give similar results but very different from the values found in the literature with the exception of SiC-6H (0001). From these results it seems that the evaluation of σ_{ys} from nanoindentation in ceramic materials is not feasible. Some reasons could be elucidated from these results:

- i. Indentation size effect affects the results as the models were developed for deformations greater than that generated by nanocontacts.
- ii. The local strain in the plastic zone is highly anisotropic in single crystals [41].
- iii. The plastic zone is not simply spherical, because of either the anisotropy of the crystal or the pyramidal shape of the indenter [8, 41, 45].



Figure 3.7.-TEM images of microindentations in SiC-6H showing the dislocation density around it at 50 mN (Adapted from [45])

3.2. Crack morphology effect on K_c with Berkovich and Vickers indenters.

Final morphology of the indentation cracks depends on the indentation load; tip geometry and material toughness (see section 3.1). Additionally, expressions to evaluate K_c depends on the crack morphology thorough the constants ζ_r (equation 1.22), k^p (equation 1.25), and Niihara constants (equation 1.23 and 1.24). Hence, it is clear that accurate K_c measurements require a proper knowledge of the crack morphology. In this sense, one of the aims of this work is focused on the experimental calibration of the constants of the fracture toughness equations 1.22, 1.23, 1.24 and 1.25 in order to correctly assess a correct evaluation of K_c by means of nanoindentation based in the study of the influence of the indenter geometry and the generated crack morphology.

In order to carry out this investigation soda-lime glass, Si (100) and SiC-6H (0001) single crystals were tested using both Vickers and Berkovich tips. Table 2.1 shows the reported values of K_c for these materials.

Si (100) and SiC-6H (0001) show a well-defined-crack pattern in the range of the applied loads. Only well-developed cracks, emerging from the impression corners, were used. Cracks appearing from the indentation edges or indentation showing chipping were not considered (see Figure 3.8).

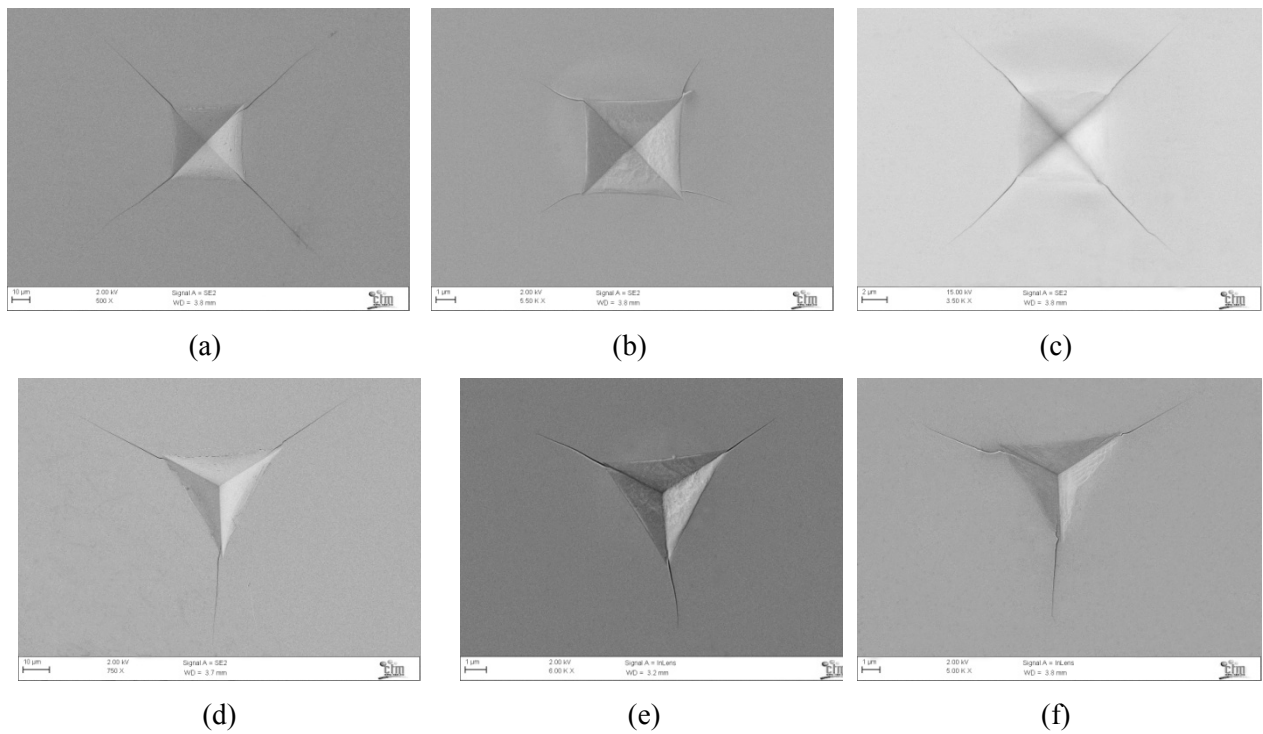


Figure 3.8.-Vicker indentation on:(a) soda lime glass at 10 N, (b) Si (100) at 200 mN, (c) SiC-6H (0001) at 1,5 N; Berkovich indentation on: (d) soda-lime glass at 0,5 N, (e) Si (1000) at 177 mN, (f) SiC-6H (0001) at 650 mN.

The three different expressions for K_c that have been analysed in this thesis are the equations of: Anstis *et al* (equation 1.22), Laugier (equation 1.25) and Niihara (equations 1.23 and 1.24). In a first step, Anstis *et al.* and Laugier equations were deeply analysed since both only deal with one crack configuration. Once it was clear the effect of the ellipticity of the crack on the result obtained for K_c by using the first two equations, Niihara formulation was analysed. The latter included both types of crack morphologies, semi-circular and semi-elliptical, and this is the reason to be treated separately.

The constants ξ_R and k^p for Anstis *et al.* and Laugier equations respectively, were determined for Berkovich indenters by fitting the experimental values of H , E , the mean crack length and the reported value of K_c for each material (Table 3.1) versus the indentation load for Berkovich indenters (Figure 3.9 and Figure 3.10). The experimental values obtained for ξ_R and k^p proposed for Berkovich indenter geometry are shown in Table 3.4. It can be observed from Figure 3.9 and Figure 3.10 that the equation which presents the best fit for the analysed materials is Laugier's equation.

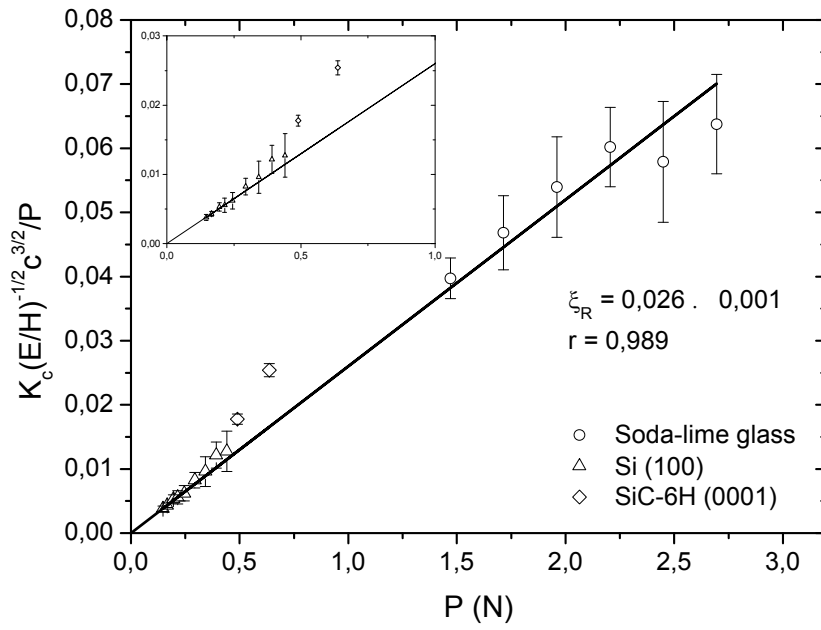


Figure 3.9.- Experimental calibration fitting of the constant ξ_R in Anstis *et al.* equation (equation 1.22) for a Berkovich indenter.

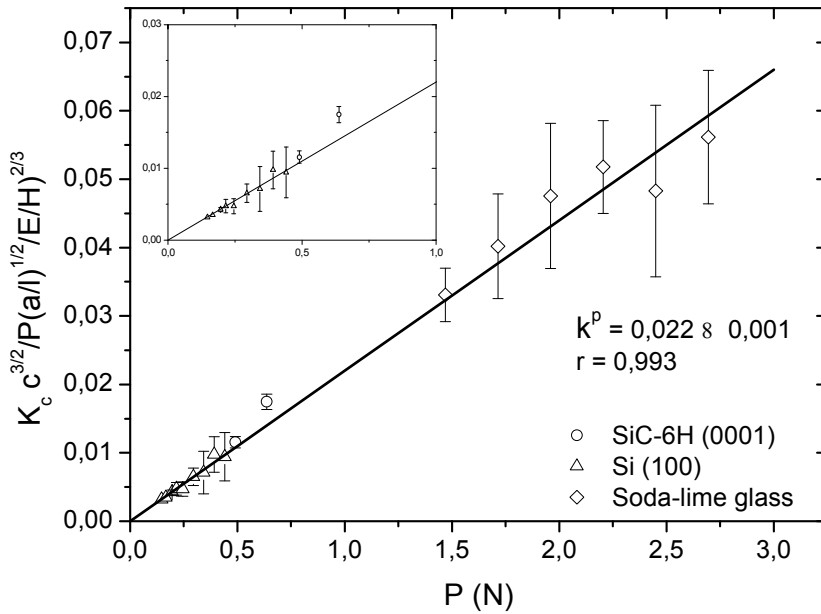


Figure 3.10.- Experimental calibration fitting of the constant k^p in Laugier equation (equation 1.25) for a Berkovich indenter.

Table 3.4.- Experimental calibration of the constants ξ_R and k^p for a Berkovich indenter for Anstis *et al.* and Laugier equations.

Crack morphology	Indenter geometry	Equation	
		Anstis <i>et al.</i>	Laugier
Half-penny	Vickers	0.016 ± 0.004	-
Radial or Palmqvist	Vickers	-	0.015 ± 0.026
Radial or Palmqvist	Berkovich	0.026 ± 0.001	0.022 ± 0.001

Table 3.5.- K_c values computed using Anstis equation (equation 1.22) and Laugier equation (equations 1.25) for Vickers and Berkovich indenters.

Material	Conventional (SENB)	Anstis <i>et al.</i> equation (MPa·m ^{1/2})		Laugier equation (MPa·m ^{1/2})	
		Vickers- Half-penny ($\xi_R=0.016$)	Berkovich- Half-penny ($\xi_R=0.026$)	Vickers- Palmqvist ($k^p=0.015$)	Berkovich- Radial/Palmqvist ($k^p=0.022$)
		Soda-lime glass	0.7	0.59 ± 0.04	0.6 ± 0.1
Si (100)	0.95	0.24 ± 0.04	0.9 ± 0.2	0.3 ± 0.1	1.0 ± 0.3
SiC-6H (0001)	3.4	1.5 ± 0.1	2.3 ± 0.1	1.6 ± 0.2	3.0 ± 0.3

Table 3.5 shows the computed K_c values, when Anstis *et al.* or Laugier equations were used, taking into account the tip geometry and the crack morphology generated. From the results shown in Table 3.5 some observations can be made:

- i. Soda-lime glass: it is well known, and it has been also proved in this work (section 4.1), that when a Vickers indenter is applied into a soda-lime glass sample half-penny cracks are generated [16]. Anstis *et al.* equation was developed for Vickers indenters and half-penny cracks; consequently this equation gives a K_c value closer to the well accepted one. On the other hand, as Laugier equation was developed for Palmqvist cracks and this is not the crack morphology observed for soda-lime glass, this equation does not give a proper value for K_c .
- ii. Si (100) and SiC-6H (0001) single crystals: it can be observed that whatever equation is used, the computed K_c value does not match with the referenced values (see Table 3.1), neither for Si (100) or SiC-6H (0001). In Si (100) single crystals, this is expected since the minimum requirement for validity of Anstis *et al.* equation, $c \geq 2a$, is not obeyed. On the other hand, if half-penny cracks are not generated ($c < 2a$) the cracks should be Palmqvist but Laugier equation neither gives a proper value for K_c . When the original correlation plot between indentation toughness and fracture toughness by standardized tests of Anstis *et al.* is carefully examined, the results for silicon single

crystals show a great dispersion which may be related to their anisotropy [11]. However, even when the effect of anisotropy is taken into account, the experimental values of K_c obtained by means of Vickers indentations, are in a wide range from $0.45 \text{ MPa}\cdot\text{m}^{1/2}$ to $1.0 \text{ MPa}\cdot\text{m}^{1/2}$ [46]. Thus it seems that the constant ξ_R has not a reliable value for this material. Laugier used the same experimental values obtained by Anstis et al to calibrate k^p , thus, it is likely that the same dispersion observed in Si (100) single crystals are affecting K_c results obtained by using equation 1.25. Accordingly, this might be the reason why the results concerning Si (100) are not good enough. In the case of SiC-6H (0001) single crystal, the material used by Anstis *et al.* to perform the experimental calibration of the equation was a polycrystalline sample and its toughness value determined by indentation ($2.4 \text{ MPa}\cdot\text{m}^{1/2}$) does not agree with that evaluated by means of standardised fracture tests ($4.0 \text{ MPa}\cdot\text{m}^{1/2}$).

- iii. When Berkovich results were analysed for soda-lime glass and Si (100) single crystal, it was observed that the two equations used, i.e. Anstis et al. and Laugier equation, report the same value of K_c for each material. Furthermore, when a proper value for the constant ξ_R and k^p were chosen regarding the tip geometry used, the equation 1.22 and equation 1.25 computed K_c values closer to the well accepted ones. This results shows that a proper value for the calibration constants that include tip geometry considerations is crucial in order to compute a reliable value of K_c . However, crack morphology not seems to have a significant effect on the computation of K_c in materials which present low fracture toughness. On the other hand, in the case of SiC-6H (0001) single crystal, Laugier equation gives a K_c value closer to the well accepted ones. This result indicates that the crack morphology generated when Berkovich tip was applied onto a SiC-6H (0001) sample was likely to be Palmqvist or at least to have a semi-elliptical shape.

To sum up, this work shows the need of a proper selection of the equation used to calculate fracture toughness for each tip geometry with a proper value for the constants ξ_R and k^p (Table 3.5). The used expression should be adequate for the observed crack morphology. From a phenomenological point of view Laugier's equation would be more adequate for evaluating K_c when Berkovich indenters are used.

On the other hand, the equation developed by Niihara is widely used and is based in a fit of Evans and Charles data. Niihara proposed two representations of this fit depending on the crack morphology, distinguishing between half-penny and Palmqvist cracks (equation 1.23 and 1.24 respectively). In order to perform an experimental calibration of the constants in Niihara equation for Berkovich indenters, the same methodology follow to find ξ_R and k^p was applied. Thus, a fitting of H, E, imprint size, the mean crack length, the constrain factor ($\phi = 3$) and the reported value of K_c for each material (Table 3.1) versus the ratio $(l/a)^{-1/2}$ or $(c/a)^{-3/2}$ depending on Palmqvist or half-penny morphology, respectively, were performed (Figure 3.11).

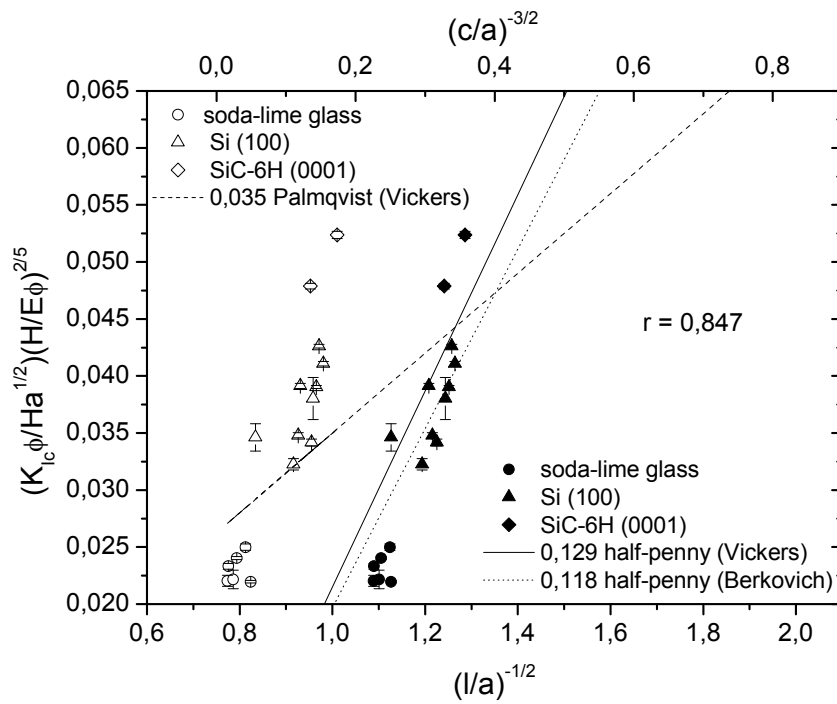


Figure 3.11.- Experimental calibration fitting of the constant in Niihara equation (equation 1.24) for a Berkovich indenter.

It can be observed from Figure 3.11 that the calibration constant presents a better fit to the experimental data when half-penny morphology is considered. Thus, in order to adjust Niihara equation when a Berkovich indenter was used, equation (1.24) was taken into account. The experimental values for the constant in Niihara equation proposed for Berkovich indenters are shown in Table 3.6.

Table 3.6.- Experimental calibration of the constants in Niihara equation for a Berkovich indenter.

Crack morphology	Indenter geometry	Niihara equation
Half-penny	Vickers	0.129
Palmqvist	Vickers	0.035
Half-penny	Berkovich	0.118 ± 0.004

Table 3.7 shows the K_c values computed using Niihara equations (equation 1.23 and 1.24) for different indenter geometry and the corresponding generated crack morphology. It can be observed that Niihara equations reported the same values for each material whatever tip geometry was used and whatever crack morphology was considered. Only when SiC-6H (0001) was analysed Niihara equation gives a different K_c value when Vickers or Berkovich indenter was considered. However, only when Vickers indenters were used the computed value for K_c is closer to that evaluated by SENB for both half-penny and Palmqvist cracks. Differences observed between the results reported by SENB and IM method

are likely to be as a consequence of the sensitivity on the constrain factor of the later method. The constraint factor was taken as a constant with a value of 3, which could not be accurate enough since it is the value calculated by Tabor for metallic materials. The constraint factor is a difficult parameter to evaluate in brittle materials since it depends on its plasticity behaviour as well as on the indenter geometry used, thus a constant value for all cases was taken. Moreover, Niihara equation was developed from an experimental fitting, which add uncertainty to the reported values.

For Berkovich indenters it has been observed that the experimental data fits well when the crack morphology is assumed to be half-penny. However, sequential polishing images (Figure 3.2) show that the generated crack morphology is radial. Thus, as can be seen in Table 3.7, Niihara equation does not work properly when Berkovich indenters are used.

Table 3.7.- K_c values computed using Niihara equation (equations 1.23 and 1.24)

Material	K_c (MPa·m ^{1/2})			
	Conventional (SENB)	Vickers		Berkovich
		Half-penny	Palmqvist	Radial/Palmqvist
Soda-lime glass	0.7	1.0 ± 0.1	1.0 ± 0.1	1.2 ± 0.1
Si (100)	0.95	1.5 ± 0.3	1.4 ± 0.1	1.5 ± 0.3
SiC-6H (0001)	3.4	3.2 ± 0.5	3.4 ± 0.1	4.3 ± 0.6

Consequently, it has been proved the need of a proper selection of the equation to compute K_c when the IM method is used in nanoindentation. It has been seen that Niihara equation does not work properly when Berkovich indenters are used because the equation does not account for the crack morphology generated by a three-sided pyramid. Since the application of a Berkovich indenter into brittle materials generates radial or Palmqvist cracks, Laugier equation seems to be the most appropriate one from a phenomenological point of view. In this work it is proposed to use Laugier equation with the proposed constant calibration value of 0.022 ± 0.001 for a Berkovich indenter

3.2.1. R-curve behaviour effect on fracture toughness evaluated by nanoindentation

It is known that many polycrystalline ceramic materials show R-curve behaviour, as ZrO₂ or coarse grained Al₂O₃, Si₃N₄ and SiC. In this work a Si₃N₄ was analysed, performing Berkovich indentations at 10, 15, 20 and 25 N. First of all, crack morphology generated by a Berkovich indenter at 20 N in this material (Figure 3.12) was studied.

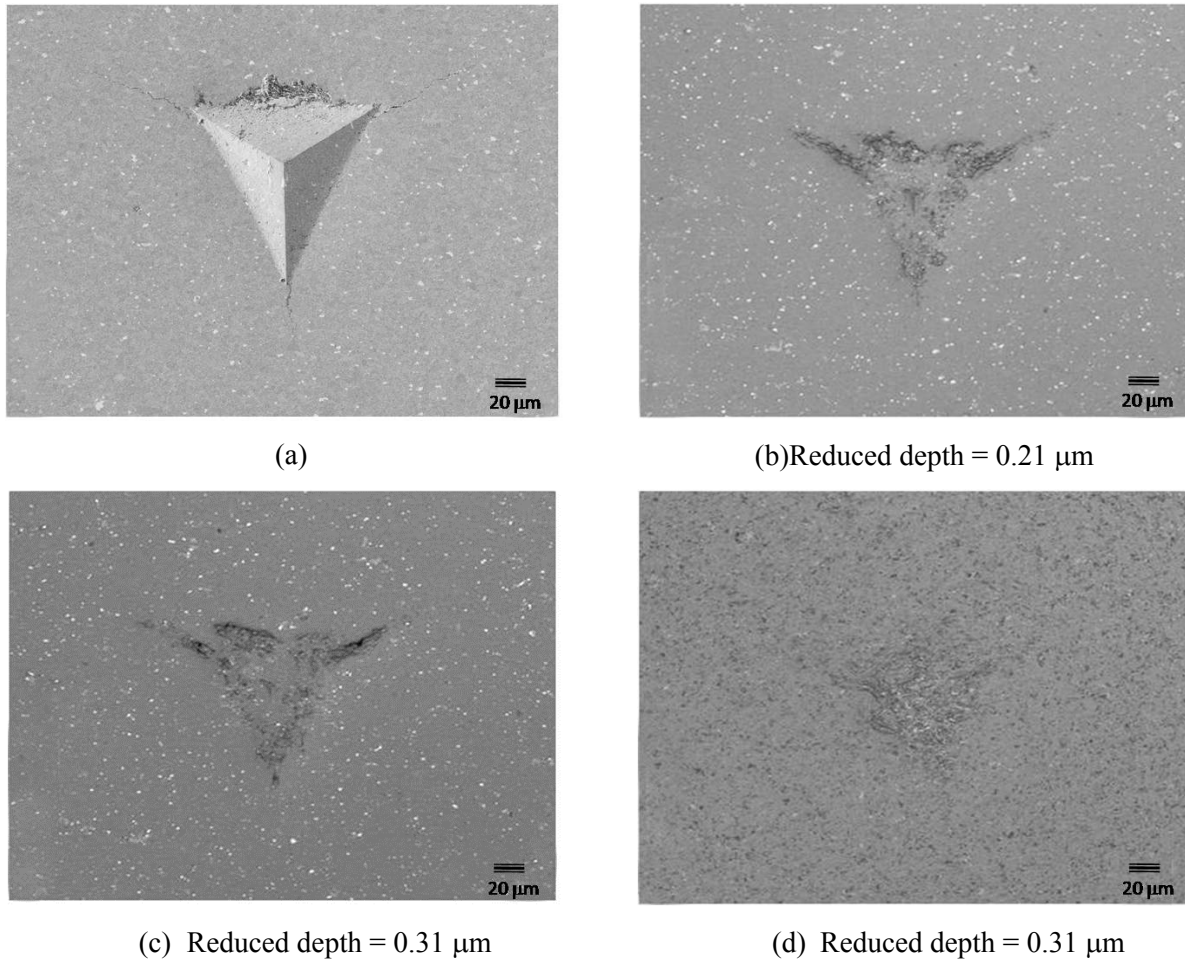


Figure 3.12.-Crack evolution SEM images of a Berkovich indentation in Si_3N_4 at 20 N using the sequential polishing technique

In Figure 3.12 can be observed that the crack morphology generated by a Berkovich indenter in Si_3N_4 is clearly Palmqvist. Since during sequential polishing the induced indentation cracks disappear before hardness impression, cracks are shallower than indentation, thus, cracks do not meet behind the hardness impression resulting in a three independent system cracks emanating from the apex of the indentation, morphology known as Palmqvist (Figure 1.8). Therefore Laugier equation (equation 1.25) with $k^p = 0.022$ was used to plot K_c versus mean crack length (Figure 3.14) in order to study the R-curve behaviour of Si_3N_4 .

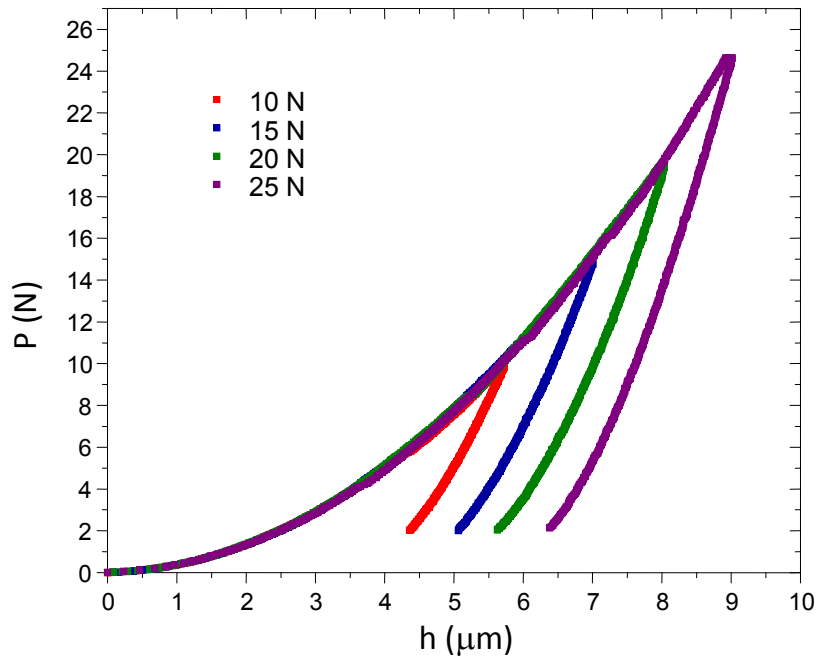


Figure 3.13. $-P-h_s$ curves for Berkovich indenters for Si_3N_4 .

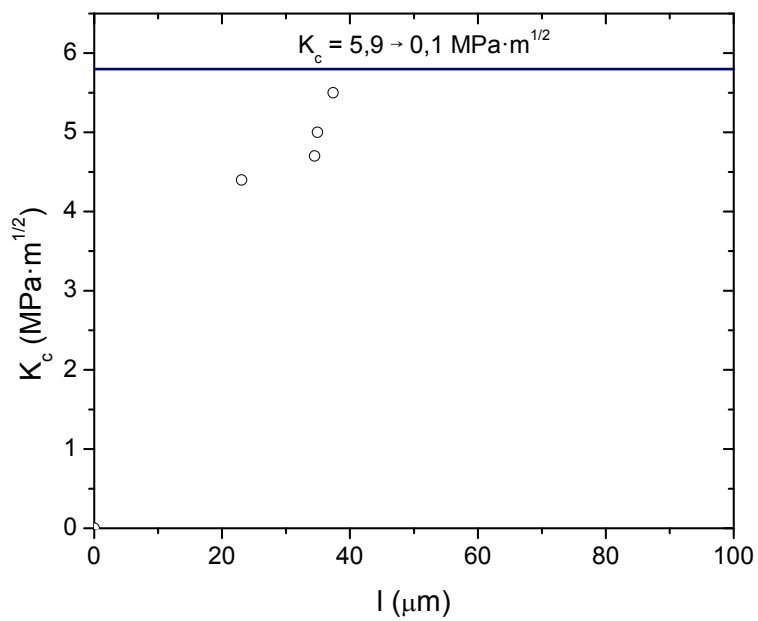


Figure 3.14. R-curve behaviour for Si_3N_4 evaluated by nanoindentation.

The fracture toughness increases with the crack size (see Figure 3.14), reaching the same value as for large cracks [47]. Thus, with R-curve behaviour the toughness of small indentation cracks is smaller

than for large cracks. This is the reason why materials with R-curve behaviour has not been chosen to determine the calibration constants ξ_R and k^p in the indentation equations studied in this thesis.

On the other hand, fracture toughness evaluation by nanoindentation technique offers the possibility of measuring the intrinsic crack-tip toughness in materials with R-curve behaviour. Intrinsic crack-tip toughness, K_{I0} , is essential to understand the strength and toughness of bridging ceramics, but the determination of accurate K_{I0} values from R-curve data is not reliable. The reason is that the range of crack length in which fracture toughness rises from K_{I0} to the saturation value is extremely short, so that an extrapolation of the measured R-curve to $l = 0$ is not accurate.

An alternative method to measure K_{I0} is through crack-opening displacement (COD) measurements [19, 48]. Further attention to COD method will be paid in Chapter 5.

3.3. Crack morphology effect on K_c with Cube-corner indenters.

In section 4.2 it has been proved that the most appropriate equation to evaluate K_c by nanoindentation with Berkovich indenters is Laugier equation with the proposed calibration constant of 0.022 ± 0.001 . Thus, in order to determine experimentally the constant k^p for a cube-corner indenter only Laugier's equation was used.

To collect more data points for the experimental calibration of the constant k^p for a cube-corner tip geometry two single crystals were also analysed, Si (111) and SiO₂ (0001). Since it is difficult to obtain accepted K_c values for single crystals, the reference values of K_c were determined by the calibrated Laugier equation for a Berkovich indenter. The indented materials show a well-defined-crack pattern in the range of the applied loads. Only well-developed cracks, emerging from the impression corners, were used. Cracks appearing from the indentation edges or indentation with chipping were not considered (see Figure 3.16).

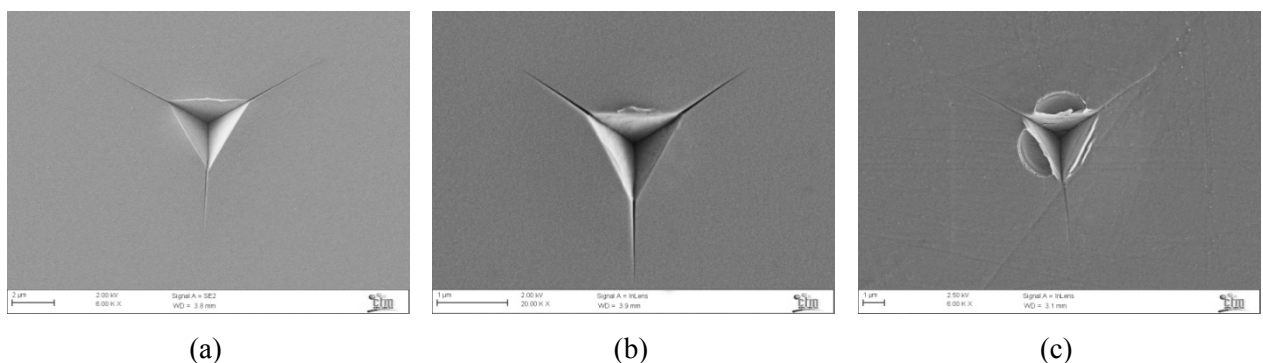


Figure 3.15.- Cube-corner indentation on: (g) soda-lime glass at 50 mN, (h) Si (100) at 10 mN, (i) SiC-6H (0001) at 200 mN.

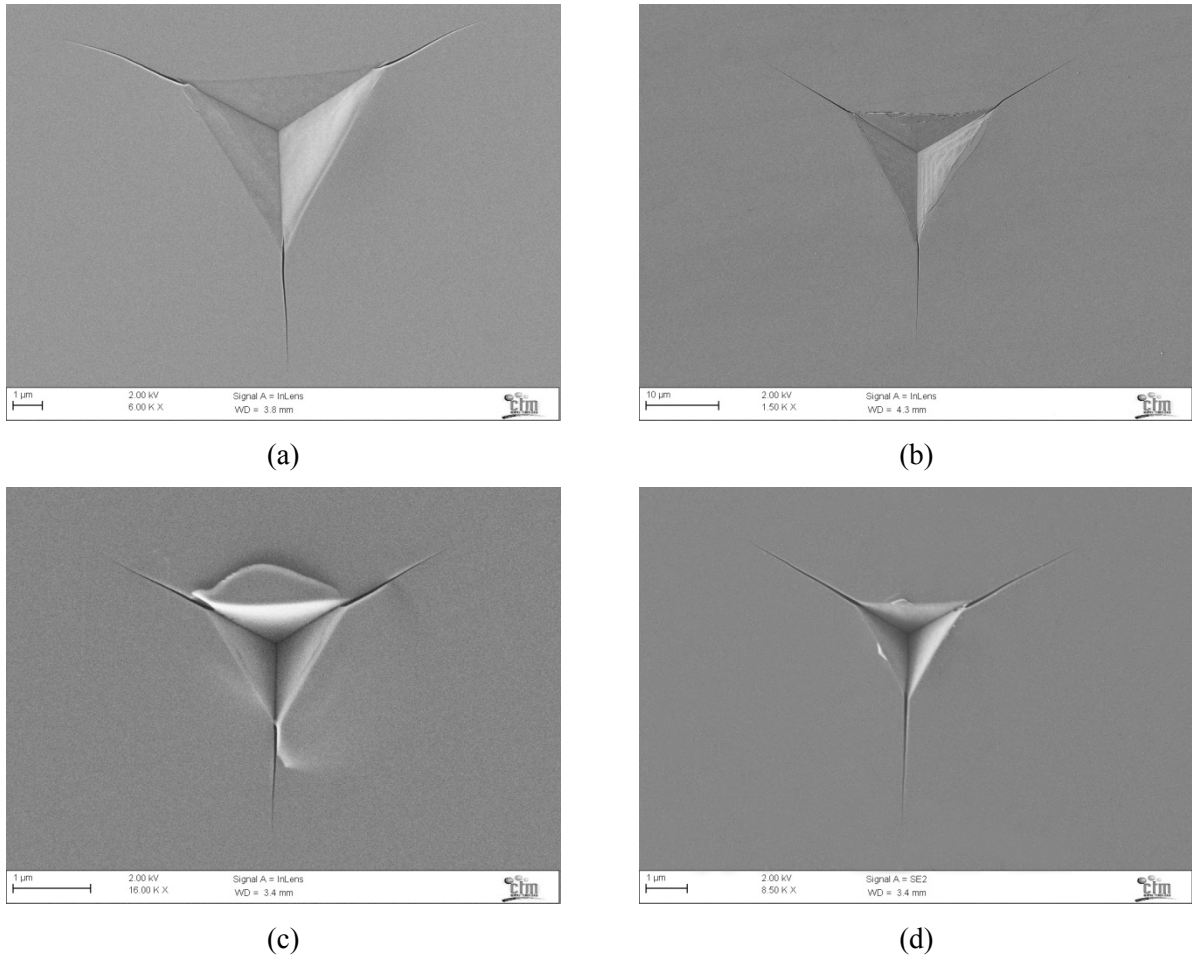


Figure 3.16.- Berkovich indentation on (a) Si (111) at 250 mN, (b) SiO₂ (0001) at 2 N; Cube-corner indentation on (c) Si (111) at 20 mN (d) SiO₂ (0001) at 50 mN.

The constant k^p was determined by fitting the experimental values of H , E , the mean crack length and the reported value of K_c for each material (Table 3.8) versus the indentation load for cube-corner indenters (Figure 3.17). The experimental value found for k^p proposed for cube-corner indenters (0.057 ± 0.002) and the K_c values obtained are shown in Table 3.8. It can be observed from Figure 3.17 that Laugier equation presents a good fit for the analysed materials.

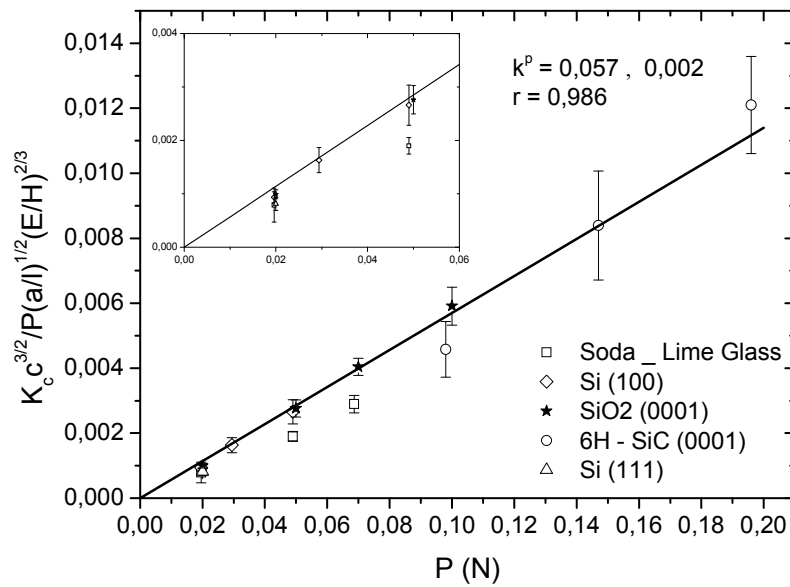


Figure 3.17.-Experimental calibration fitting of the constant k^p in Laugier equation (equation 1.25) for a cube-corner indenter.

Table 3.8.- K_c values computed using Laugier equation (equations 1.25) for Berkovich and cube-corner indenters.

Material	K_c (MPa·m ^{1/2})		
	Conventional (SENB)	Berkovich $k^p = 0.022 \pm 0.001$ Radial/Palmqvist	Cube-corner $k^p = 0.057 \pm 0.002$ Radial/Palmqvist
Soda-lime glass	0.7	0.6 ± 0.1	0.8 ± 0.1
Si (100)	0.95	1.0 ± 0.3	1.0 ± 0.1
SiC-6H (0001)	3.4	3.0 ± 0.3	3.5 ± 0.8
Si (111)	–	1.4 ± 0.3	2.0 ± 0.6
SiO ₂ (0001)	–	1.1 ± 0.1	1.0 ± 0.1

It can be seen that it is always necessary to determine fracture toughness from the equation which has been calibrated for the tip used. For instance, if we use a cube-corner indenter for calculating K_c of Si (100) but we use the equation for Vickers indenter (equation 1.25 with $k^p = 0.015$ obtained by Laugier) K_c is 0.31 ± 0.04 MPa·m^{1/2} (calculated in [14]). However, if equation 1.25 for type of indenters is calibrated and k^p for the cube-corner indenter is used ($k^p = 0.057$), K_c is 1.0 ± 0.1 (see Table 3.8). Thus, knowledge of the tip geometry used and the generated crack system is crucial to obtain accurate values of K_c by nanoindentation when using Berkovich and cube-corner indenters.

The calibration constant for cube-corner indenters obtained above differs from that found in other previous works [15, 33, 49-52]. A range of values from 0.033 to 0.040 have been reported for cube-corner indenters [15, 33, 50-52], whereas in this work a value of 0.057 was obtained. If it is assumed that the

parameter is related only to tip angle, a theoretical value of 0.033 can be expected. On the other hand, depending on the toughness range of the materials studied, values of 0.0319 [51], 0.036 [50] or 0.040 [52] are reported. The main reason for the discrepancy is the equation chosen to fit the experimental data. In the literature for cube-corner indenters the equation fitted was 1.21. However, since the crack morphology is semi-elliptical, equation 1.25 is more suitable since it takes this fact into account.

With respect to Berkovich indenters, Dukino *et al.* reported $k^p = 0.016$ (fit performed in the microindentation range, up to 5 N), whereas the value obtained here is slightly different, 0.022 [49]. Such discrepancy could arise from the different formulation of the equations used as discussed above.

Concerning the range of fracture toughness that can be measured with the proposed values of the calibration constants, this is the same as the range of fracture toughness studied, i.e. at least up to $3.4 \text{ MPa} \cdot \text{m}^{1/2}$. This range covers a wide range of glasses and traditional and engineering ceramics.

The experimental calibration of the constant in this work has been performed using a soda-lime glass and single crystals. Referring to the latter, crystal anisotropy must be considered when indenting single crystals, since it is known that indentation cracking depends on the crystallographic orientation. Ebrahimi and Kalwani studied the fracture anisotropy of Si single crystals with Vickers tips, indenting different crystallographic planes and considering the fracture along different crystallographic directions [46]. They show a clear influence of crystal anisotropy on the fracture toughness. However, K_c remains almost constant when indenting the (001) and (111) planes of Si, but larger scatter is found for the (110) plane [46]. Thus, in order to minimize the effect of crystal anisotropy on indentation cracking and to obtain reliable values of the experimental calibration constants, Si (100) and Si (111) single crystals were chosen to calibrate equations 1.21 and 1.25. After experimental assessment of the crack pattern in the tested single crystals, no evidence was found of preferred fracture directions or abrupt changes in the crack propagation for different crystal-tip orientations. Additionally, crack lengths variations in the preferred fracture directions are similar to those measured in amorphous and isotropic sample soda-lime glass. Such results show that crystal anisotropy does not significantly affect the values of the experimental calibration constants reported in this work. Nevertheless, crystal anisotropy must be kept in mind when characterizing single crystals by nanoindentation and accurate analysis of crack patterns is highly recommended, as well as consideration of the relative orientation of the indenter tip in the indented plane.

In summary, examination of the crack morphology shows that indentation cracks have a semi-elliptical shape when Berkovich and cube-corner indenters are used in nanoindentation. Therefore, from a phenomenological point of view Laugier's equation would be more suitable for evaluating K_c . The calibration constants of this equation are 0.022 ± 0.001 for a Berkovich indenter and 0.057 ± 0.002 for a cube-corner indenter. The nanoindentation fracture toughness obtained by using these constants is close to the actual fracture toughness measured by standardized methods in materials without R-curve behaviour.

Micromechanical characterization of micro-sized particles by means of Nanoindentation: Influence of Crystal Anisotropy and Residual Stresses effect.

I find your lack of faith disturbing.

Darth Vader

In single crystals almost any property of interest (including chemical resistance, elastic response or fracture toughness) is anisotropic; and almost all materials of engineering interest are polycrystals. A material property is anisotropic when it does depend on the orientation of the sample with respect to some external frame. The anisotropy of a property is related to the materials structure.

Materials science is concerned with the structure/property relations. The anisotropy in polycrystalline aggregates depends both on anisotropy of the single crystals and on the texture of the polycrystal. The anisotropy of a property is generally is related to the symmetry elements of the underlying material structure (but also depends on the property being considered).

One of the aims of this investigation is to apply the IM method onto the micro-sized particles that form most of the engineering materials. Thus, crystal anisotropy of these particles among other aspects as the residuals stresses exerted by the surrounding matrix must be taken into account in their micromechanical characterization.

Residual stresses in multiphase materials are induced by difference in the thermal expansion coefficient of each phase. Residual stresses are difficult to evaluate; therefore, it is very important to have a reliable method to measure them directly with minimum damage to the surface. There are several techniques that are used to measure residual stresses. X-ray diffraction, neutron diffraction, Raman spectroscopy or nanoindentation technique, are non-destructive methods that allows the measurement of residual stresses in isolated spots. Nanoindentation offers the advantage of computing E , H , K_c and σ_{res} from a single test and in very localized areas.

In this chapter, the effect of crystal anisotropy and residual stresses on the fracture toughness measurement obtained by nanoindentation will be studied. A hypereutectic Al-Si alloy was chosen to perform this study on primary silicon particles as Si (100) and Si (111) single crystal samples were available for comparison. In this way, the effect of the metal matrix on silicon can be assessed. Moreover, different hardmetal grades were examined in order to investigate both the effect of crystal anisotropy and the effect of WC particle sizes on the fracture toughness measurements.

4.1. Crystal anisotropy on single crystals

In single crystals physical and mechanical properties often differ with orientation. The atomic planes forming the crystalline structure slip only in some crystal directions. Anisotropy becomes evident observing the planes on which fracture of sapphire (Al_2O_3) and magnesium oxide (MgO) single crystals takes place after indenting. The crystal structure of sapphire (Figure 4.1a) is hexagonal (rhombohedral single crystal), with lattice parameter $a = 47.58$ nm and $c = 129.91$ nm, and that of MgO (Figure 4.1b) is a FCC lattice of O ions with Mg ions occupying all the octahedral sites or vice versa and with lattice parameter $a = 22.17$ nm.

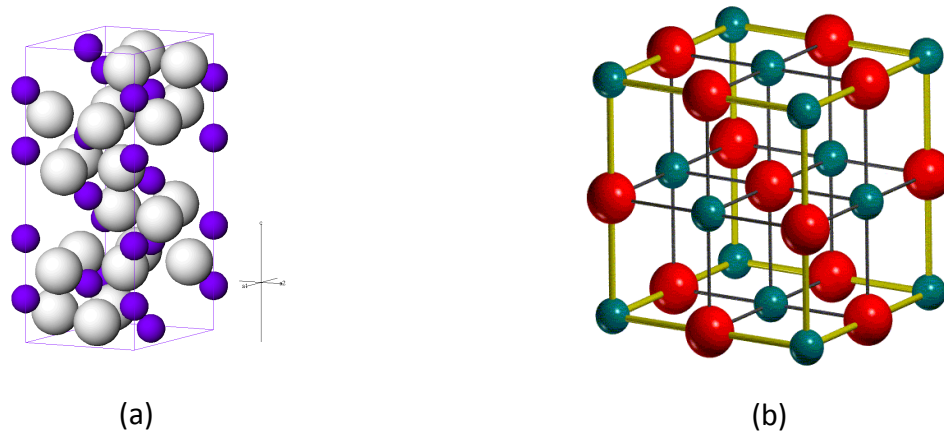
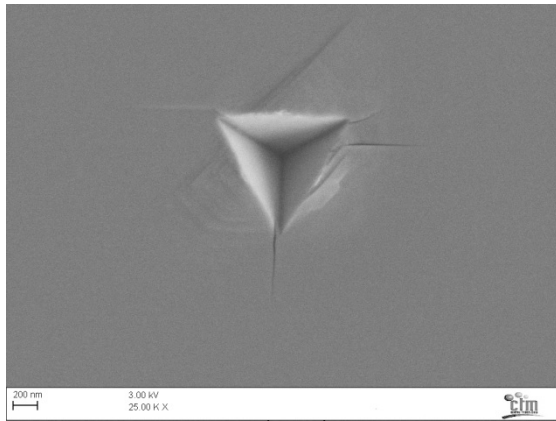


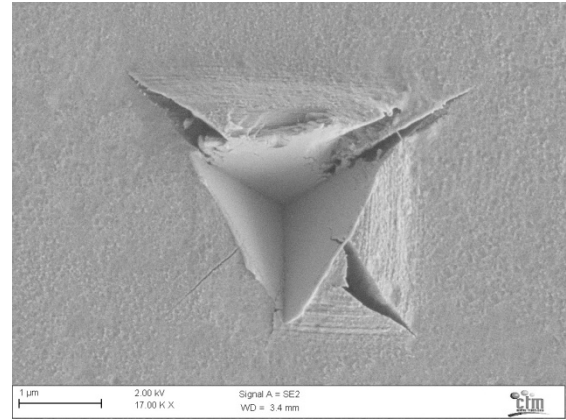
Figure 4.1.-Representation of the unit cell for Al_2O_3 ($\bar{1}\bar{1}20$) and MgO (100) single crystals.

In this thesis, indentations with a cube-corner tip were performed on the planes ($\bar{1}\bar{1}20$) and (100) in Al_2O_3 and MgO respectively. The corresponding SEM images showing fracture anisotropy can be observed in Figure 4.2a and 4.2b, respectively. Cracks in Al_2O_3 ($\bar{1}\bar{1}20$) and MgO (100) deviate following preferential directions indicating high crystal anisotropy. Fracture toughness cannot be computed by IM method as cracks should emanate from the indentation corners to satisfy the conditions of the method. On the contrary, there are anisotropic single crystals like silicon in which three cracks emanate from the indentation corners and the IM method can be applied (see Figure 4.2c). The anisotropy in fracture of single crystals will depend on bonding energy along the different crystal planes. MgO crystal has a bonding energy ranging between 600 and 1500 KJ/mol depending on the valence, and Al_2O_3 presents even a higher bonding energy, $E_{bond}(\text{Al}_2\text{O}_3) = 1.64 E_{bond}(\text{MgO})$. On the other hand Si or SiC present a lower bonding energy, 340 KJ/mol and 360 KJ/mol, respectively. Thus, Si and SiC will be easier to fracture than MgO and Al_2O_3 [53].

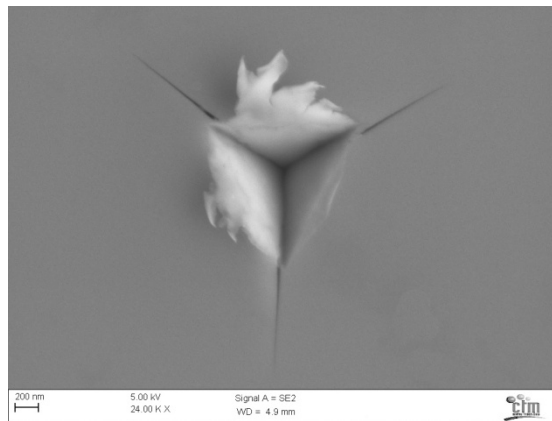
In order to study K_c anisotropy of single crystals two silicon crystallographic planes, (100) and (111), were chosen to perform cube-corner indentations.



(a) Al_2O_3 ($1\bar{1}20$), $P = 20$ mN



(b) MgO (100); $P = 20$ mN



(c) Si (100), $P = 20$ mN

Figure 4.2.-SEM images showing the anisotropic way of fracture for the single crystals analysed.

Fracture toughness for Si (100) and Si (111) samples were evaluated for random orientation of the tip faces with respect to crystal orientation, and the results of K_c in comparison with those found in the literature are shown in Table 4.1.

Table 4.1.- K_c values computed by means of IM method without any orientation consideration.

Material	K_c evaluation method	K_c at different unknown orientations ($\text{MPa}\cdot\text{m}^{1/2}$)
Si (100)	IM (cube-corner tip)	1.0 ± 0.1
Si (111)	IM (cube-corner tip)	2.0 ± 0.6
Si (100)	SENB	$0.95^{[21]}$
Si (111)	IM (Vickers tip)	$0.93 \pm 0.07^{[46]}$

As seen in Table 4.1 fracture properties reflect the underlying anisotropy of Si. The combined anisotropy of surface energy, elastic constants and plastic deformation yields a fracture toughness that also depends on crystallographic orientation. When an anisotropic elastic silicon single crystals, are

loaded, the crack path depends on the variation with orientation of the elastic energy release rate and the surface energy. Cracks may deviate from the maximum tensile stress planes and propagate through planes of lower fracture resistance [46]. Thus, K_c anisotropy will also depend on the crystal-tip orientation; for this reason, a study taking into account the crystal – tip orientation was also performed. Figure 4.3 shows the variation of K_c with crystal – tip orientation and with the applied load when a cube-corner indenter is used.

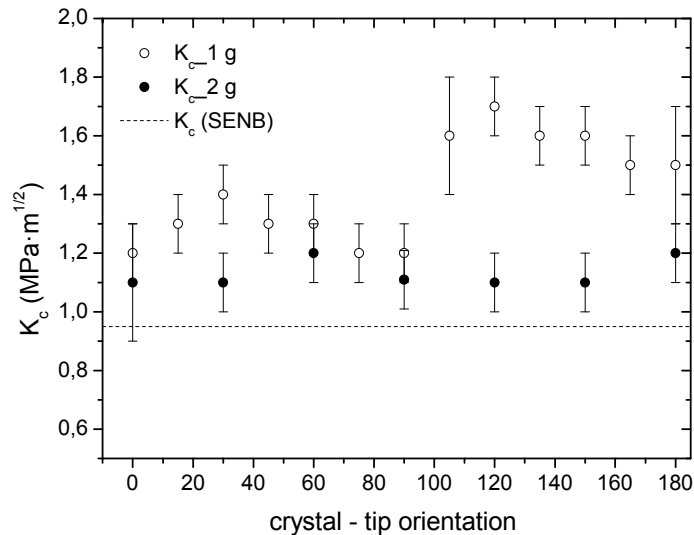


Figure 4.3.- Fracture toughness variations with crystal – tip orientation ranging from 0° to 180° with respect the <110> direction..

When K_c of single crystals is evaluated, the effect of the elastic modulus anisotropy should be also taken into account. Nevertheless, Cook showed that both elastic modulus and fracture resistance variations lead to a very small variation in fracture toughness. This author also stated that beneath indentations, elastic strain fields are multiaxial since $P-h_s$ curves or hardness do not depend significantly on the orientation of the indenter. Thus, the polycrystalline modulus is a good approximation for single crystals [34]. Although differences in elastic modulus and fracture energy should be taken into account by indenting on (001) or (111) planes of silicon, only small variations in toughness are measured, for example 0.75 MPa·m^{1/2} in (001) and 0.68 MPa·m^{1/2} in (111) plane [34]. The effect of the modulus anisotropy can be evaluated by comparing the variations in K_c . For silicon single crystals, the modulus is isotropic in (1 $\bar{1}$ 1) indent plane and did not have an effect on the variation in toughness. For the (001) indent plane the modulus varies with orientation, however, the toughness did not change significantly. Thus, it seems that there is not a direct correlation between modulus and fracture toughness anisotropy.

There are several additional effects that could influence the computed K_c value, besides the inherent of properties like the possibility of phase transformations during indentation process. One example is again silicon where pressures generated during contact may exceed a critical value for phase transformation. Silicon transforms from the semiconducting, diamond-cubic structure to metallic β -Sn structure during indentation. Accordingly, contact deformation is also influenced by metal-like flow that takes place often leading to extrusion of material from sharp indentation (see Figure 4.2c), complicating further the residual contact pattern.

In the present work, indenting either on (001) or (111) planes of silicon did not significantly affect the reported K_c values and the crack pattern in the tested single crystals showed no evidence of preferred fracture directions or abrupt changes in the crack propagation direction for different crystal-tip orientations. Additionally, crack lengths did not vary significantly; and the variations in length were similar to those measured in amorphous and isotropic sample (soda-lime glass).

On the other hand, Figure 4.3 clearly shows that K_c of Si depends both on the applied load and on the crystal – tip orientation. It can be seen that when Si (100) single crystals are indented with a cube-corner tip following $\langle 100 \rangle$ direction, crystallographic effects are greater at 10 mN than at 20 mN. Crystal- tip orientation anisotropy is not clearly seen at 20 mN, whereas at 10 mN is evidently observed. Despite these anisotropy observations, different loads and different unknown orientations between the tested sample and the tip were used for measuring a K_c for Si (100). Significant deviations from the value reported using SENB methodology were not observed (see Table 4.1), meaning that a mean value independent of the applied load is not sensible to ISE effects. On the other hand, when results at 20 mN and 10 mN are analysed, K_c values seem to be affected by ISE since when the load is decreased the toughness increases.

From a crystallographic point of view it is worth to examine the aforementioned results according to the shear stress on the possible slip plane. The shear stress is given by multiplying the axial stress by the Schmid factor which is given by:

$$\mu = \cos \varphi \cdot \cos \lambda \quad (4.1)$$

where φ is the angle between the loading direction and perpendicular to the slip plane, and λ is the angle between the loading direction and the slip direction. According to Schmid law the slip system will be that with the highest Schmid factor. In that slip system dislocations can move more easily due to the highest shear stress, and plasticity will appear soon on these planes relaxing the stress concentration induced by the indenter, so that higher fracture toughness will be measured. In Si, with a diamond cubic crystal structure, the active slip systems among the 12 possible ones were identified by calculating the Schmid factor for each system (see Table 4.2). Only two of the three possible slip systems were active on each of the unique slip planes and that four planes were active for the (001) orientation, three for (111) and two for (110).

Table 4.2. Schmid factor for the 12 possible slip systems for Si.

Slip plane	\vec{b}	Schmid factor magnitude for loading direction		
		$[00\bar{1}]$	$[\bar{1}\bar{1}\bar{1}]$	$[\bar{1}\bar{1}0]$
$(\bar{1}\bar{1}\bar{1})$	$[\bar{1}0\bar{1}]$	0.408	0.272	0.408
	$[0\bar{1}\bar{1}]$	0.408	0.272	0.408
	$[\bar{1}\bar{1}0]$	0	0	0
$(1\bar{1}\bar{1})$	$[0\bar{1}\bar{1}]$	0.408	0.272	0
	$[10\bar{1}]$	0.408	0	0
	$[110]$	0	0.272	0
$(\bar{1}11)$	$[\bar{1}0\bar{1}]$	0.408	0.272	0
	$[01\bar{1}]$	0.408	0	0
	$[110]$	0	0.272	0
(111)	$[01\bar{1}]$	0.408	0	0.408
	$[10\bar{1}]$	0.408	0	0.408
	$[\bar{1}\bar{1}0]$	0	0	0

From Table 4.2 it can be concluded that the Schmid factor on the slip planes (111) when the applied force is perpendicular to (001) is larger than when is applied perpendicularly to (111) planes. Therefore, K_c is expected to be smaller on indented (111) planes than in (001) planes. Table 4.1 shows that Si (001) and Si (111) present the same K_c value except when it is evaluated by cube-corner indentation.

4.2. Crystal anisotropy and residual stresses effects in multiphase materials

When hard particles in multiphase materials are analysed, both crystal anisotropy and the residual stresses imposed by the surrounding matrix must be taken into account. Here, this will be investigated in a hypereutectic Al-Si alloy and different WC/Co grades. In Al-Si, Si needles were indented in order to assess the influence of the residual stresses imposed by the surrounding matrix on K_c by means of nanoindentation. For WC/Co, WC carbides were indented in order to examine the influence of only crystal anisotropy on H , E and K_c .

4.2.1. Crystal anisotropy effects

Micro-sized particles can be assimilated as single crystals embedded in a softer matrix. The effect of crystal anisotropy on the mechanical properties (H , E , K_c) of these particles of Si and WC embedded in an Al matrix and in a hardmetal respectively, were evaluated by nanoindentation.

Silicon particles

Silicon needles in a hypereutectic Al-Si alloy were analysed in terms of H , E and K_c . The results were compared with those obtained in silicon single crystals. In this manner possible matrix effects on the mechanical properties evaluation can be appraised. H and E results for both Si single crystal and Si needles are presented in Table 4.3, whereas K_c results obtained by using equation 1.25 with k^p equal to 0.022 or 0.057 for Berkovich and cube-corner tips respectively, are shown in Table 4.4.

Table 4.3.- H and E of Silicon needles.

Material	H (GPa)	E (GPa)
Si (100)	12.6 ± 0.2	175 ± 1
Si needles	12.8 ± 0.2	172 ± 9

Table 4.4.- K_c of Silicon needles.

Material	K_c (MPa·m ^{1/2})
Si (100)	1.0 ± 0.1
Si needles	1.4 ± 0.2
Si (100)_SENB	0.95 ^[54]

The results in Table 5.3 indicate that the surrounding matrix in multiphase materials does not have a measurable effect on the H and E values of micro-sized particles. For K_c , there is a slight difference between the measured fracture toughness of Si needles and of Si single crystals. This disagreement could be due as a consequence of the residual stresses experimented by Si needles. Due to the difference in the dilatation coefficients between the metallic matrix and the hard particles the aluminium matrix constraints the Si needles during the cooling process. This effect will be examined in section 4.2.2.

Whit respect to crack morphology, a sequential polishing of one of the Berkovich indentations performed into a Si needle was carried out to analyse the possible effects of the matrix. Figure 4.4 shows SEM images of a Berkovich indentation performed at 0.12 N and its final polish step, and a cube-corner indentation at 20 mN. Figure 4.4b demonstrates that crack morphology does not change as a consequence of the presence of the matrix since the same kind of cracks were observed in both Si needles and Si single crystals (see Figure 3.4). Moreover, Figure 4.4a and 4.4b exhibit the same crack appearance as in Si single crystals (see Figure 3.15 and Figure 3.16), in the sense that no crack deviation were observed, meaning that any anisotropy effect appears due to the surrounding matrix.

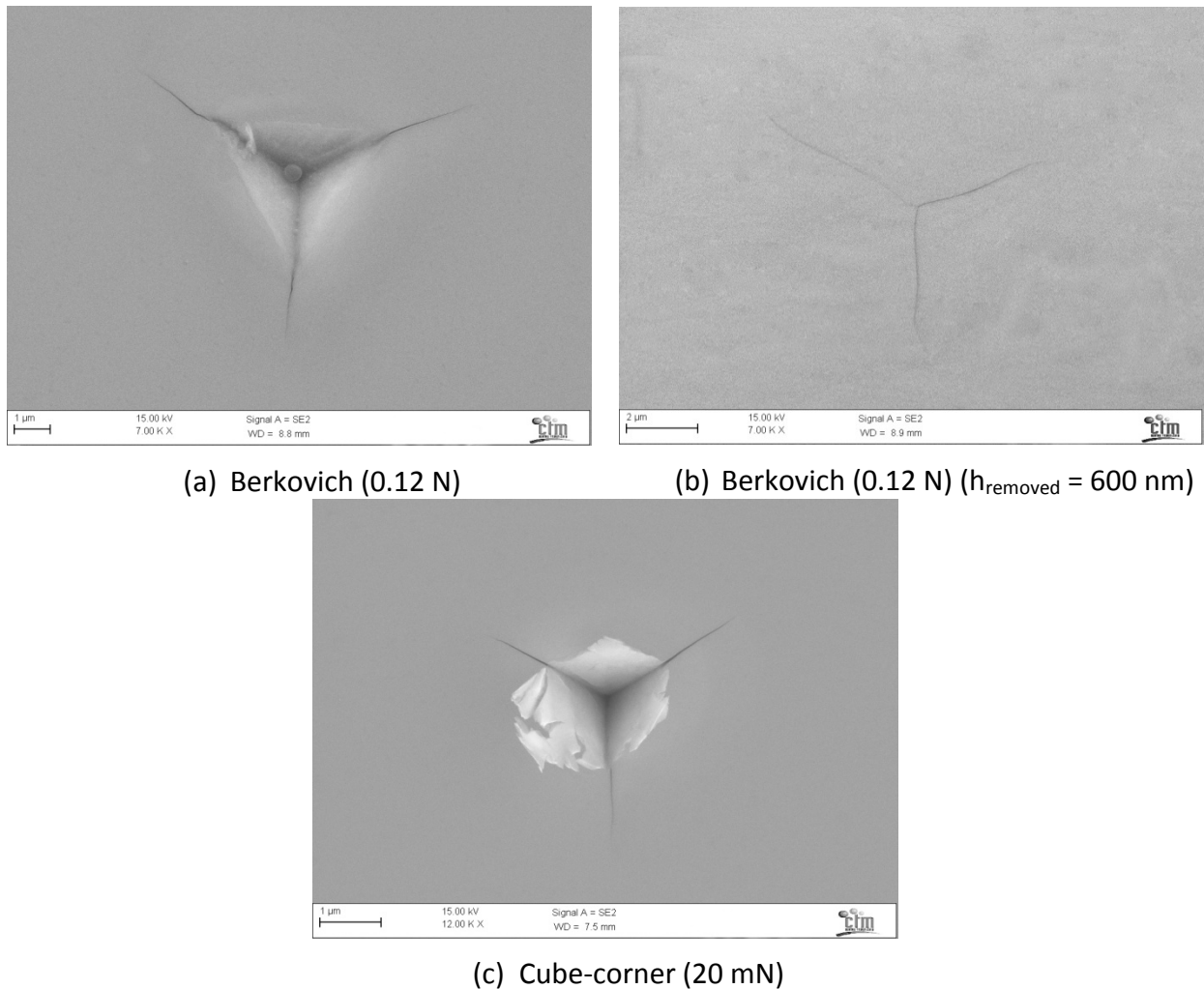


Figure 4.4.- SEM images of (a) a Berkovich indentation imprint and the generated cracks performed at 0.12 N in a Si needle, (b) the final polishing step of the Berkovich indentation imprint presented in (a), (c) a cube-corner indentation at 20 mN in a Si needle.

WC particles

The values of H and E obtained from measurements on WC single crystals are shown in Figure 4.6. Crystallographic orientation of the WC grains was assessed by means of EBDS (see Figure 4.5). A marked variation of the properties depending on the indented facet was observed which is consistent with results of previous works [24, 25, 55]. Moreover, indentation size effects (ISE) were also observed. ISE may be described as an increase in hardness as the indentation size or load is reduced. Several reasons have been suggested to explain the ISE effect, particularly in terms of an increasing difficulty in inducing plasticity as the size of indentations is reduced or a rising contribution of elastic deformation as the hardness of the materials increases for small loads [56].

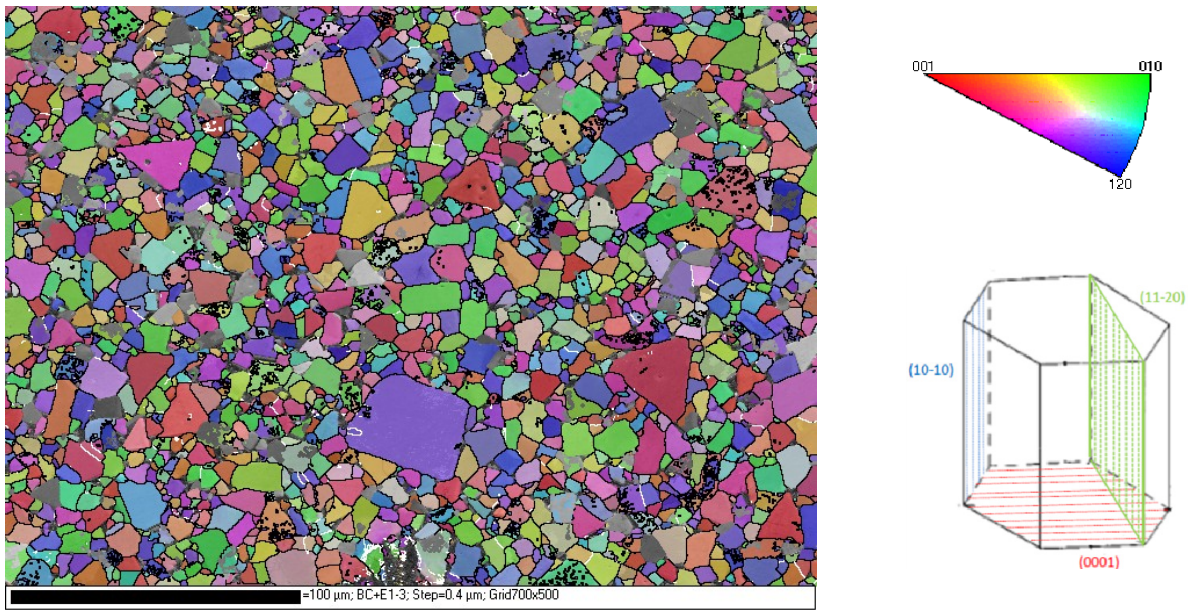
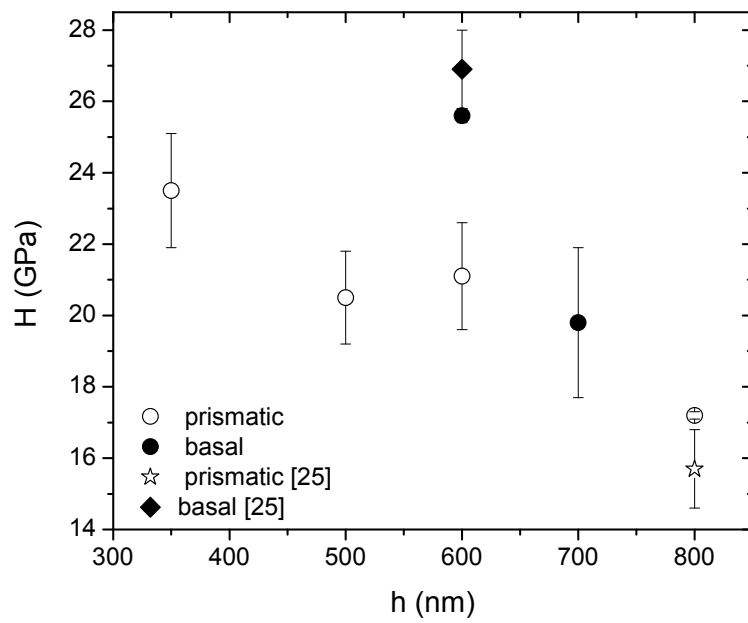
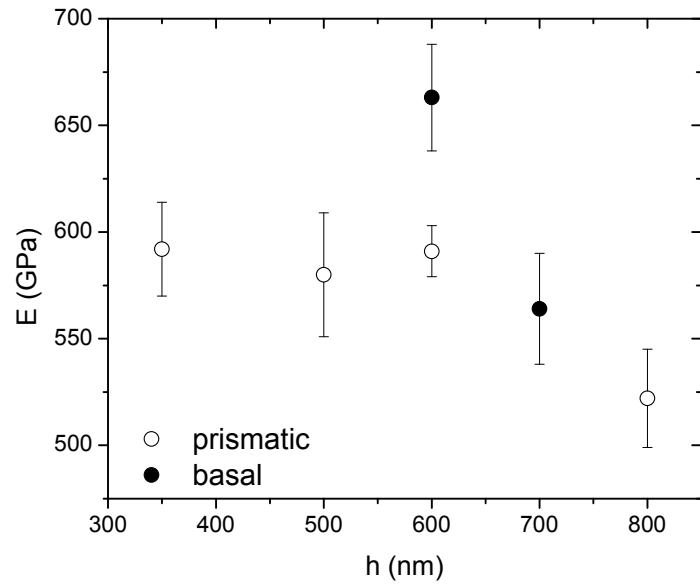


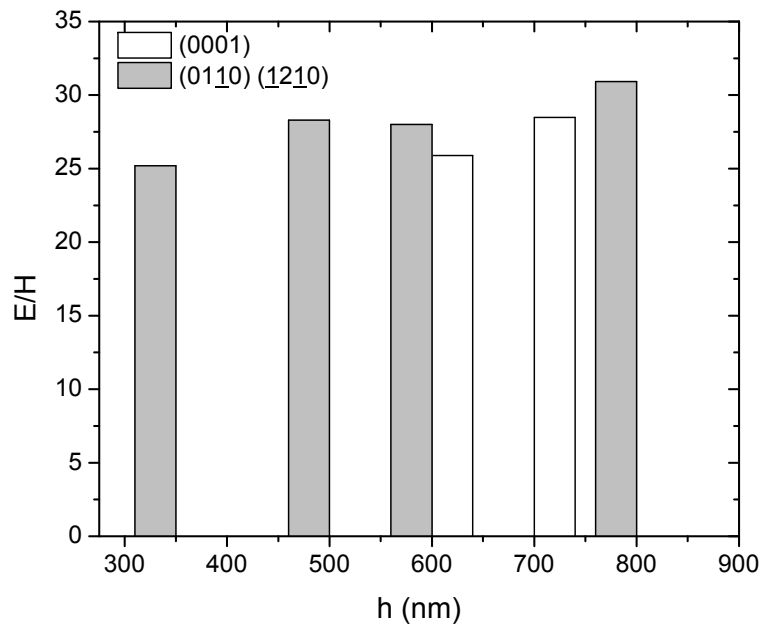
Figure 4.5.- EBSD images indicating the crystallographic orientation of each WC grain.



(a)



(b)



(b)

Figure 4.6.- Effect of the crystal anisotropy and ISE on: (a) H , (b) E (pattern bars); (c) the ratio E/H in (0001) basal planes and (10-10), (11-20) prismatic facets.

Table 4.5.- Hardness anisotropy in WC crystals.

Crystallographic orientation	HV (Kg/mm ²)[Pons]	H (GPa)	E (GPa)
Prismatic facet	1450 ± 100	17.2 ± 0.1	564 ± 26
Basal facet	2500 ± 100	25.6 ± 0.2	532 ± 23

In this thesis, it has been experimentally assessed that hardness of WC single crystals depends on the orientation of the indented crystallographic plane, as previously showed in other works [24, 25, 55, 57]. In Table 4.5 the results obtained by Pons et al. with Vickers microhardness indentation at 0,2 N are shown along with the results obtained in this work at the same load. Moreover, French et al. also reported that hardness of basal facets is twice than that determined on prismatic ones. Although hardness of basal facets shows little anisotropy, hardness of prismatic facets shows a marked orientation dependence [57]. Such marked anisotropy in hardness must be taken into account when analysing micromechanical properties of hardmetals.

The measure of K_c was experimentally difficult because either not all the indented crystals show a well-defined crack pattern or cracks propagate out of the indented grain. Thus K_c was evaluated by selecting the indented grains with well-developed cracks, in terms of size and shape. Additionally, in order to study a possible grain size effect on the K_c results computed for each WC crystal, hardmetals with different grain size were analysed (see Figure 2.2). Table 4.6 shows the results of K_c obtained by using equation 1.25 with k^2 0.057 (since a cube-corner tip was used to perform the tests) for different WC crystals indented at different loads (Figure 4.8). Evaluation of K_c following equation 1.25 depends on the ratio E/H ; hence, the different mechanical behaviour of the different facets of WC should be taken into account when computing K_c . Ideally the values of E and H for each carbide should be used to compute K_c . In this thesis, evaluation of H and E at the same penetration depth than the penetration depth required to generate fracture with a cube-corner indenter was not possible. The main reason for this is the referred ISE and the fact that a cube corner tip produces a deeper imprint than a Berkovich one. Thus, in the calculation of K_c (Table 4.6) the ratio E/H is computed taking the value of E and H given in Table 4.5 for each crystal facet. On the other hand, a K_c dependency on the grain size was observed. Figure 4.7 shows how the K_c value increases as the grain size decreases. Because grain boundaries impede dislocation movement, dislocation pile ups form at the grain boundaries whose sizes are smaller. These dislocation pile ups impede that cracks generated by nanoindentation propagate within the grain; therefore, toughness appears to be higher as the grain size diminishes. Consequently, as the grain size diminishes plasticity becomes the governing mechanism apparently increasing the K_c of the analysed crystal. This influence must be taken into account when anisotropy effects in WC crystals would be studied. For that reason, with the purpose of investigating anisotropy effects on the mechanical behaviour, only one sample with a main grain size of 20 μm were analysed

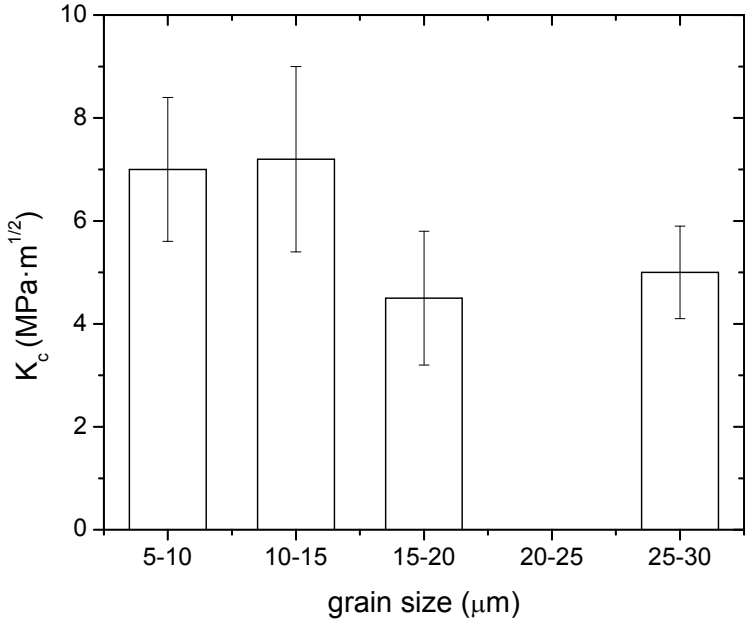


Figure 4.7.- Hall-Petch effect on K_c measured on WC crystals.

Fracture toughness of WC crystals embedded in a hardmetal is not available in the literature, only the work of Warren gives some data [58], so the comparison with the obtained values is difficult. The values of K_c found in this thesis are listed in Table 4.6 for WC. They present relatively high toughness, 7.2-9.9 $\text{MPa}\cdot\text{m}^{1/2}$, which is consistent with previous reported measurements performed in WC single crystals. In this work the computed K_c values are in the upper range of the values experimentally assessed by Hertzian indentation [58] or linearly extrapolated, to zero volume fraction cobalt, from fracture toughness data for WC-Co alloys [59, 60]. Such relatively high toughness measured by nanoindentation is also supported by the marked plastic deformation observed when indenting both prismatic and basal planes (see Table 4.6). In other metallic carbides there is brittle fracture, without evidence of plastic deformation [61]. This is a clear indication of the intrinsic tough-like character of WC crystals, which may be related to the success along the years of WC alloys as tool materials since their implementation almost one century ago.

Table 4.6.- Fracture toughness of WC at different crystal orientation

Indented plane	K_c ($\text{MPa}\cdot\text{m}^{1/2}$)
Prismatic facet	9.9 ± 2.0
Basal facet	7.5 ± 0.8

When indenting the prismatic facets, fracture is induced at both low and high applied loads (Figure 4.8a and 4.8b). The emergence of fracture to the surface when indenting basal facets is dependent upon the

applied load: in the low range (50 mN) cracks are generated (Figure 4.8d), whereas is the high one (0,15 N) these features are suppressed (Figure 4.8c). Figure 4.8e and 4.8f show a detail of the slip lines generated in a prismatic and a basal facet, respectively.

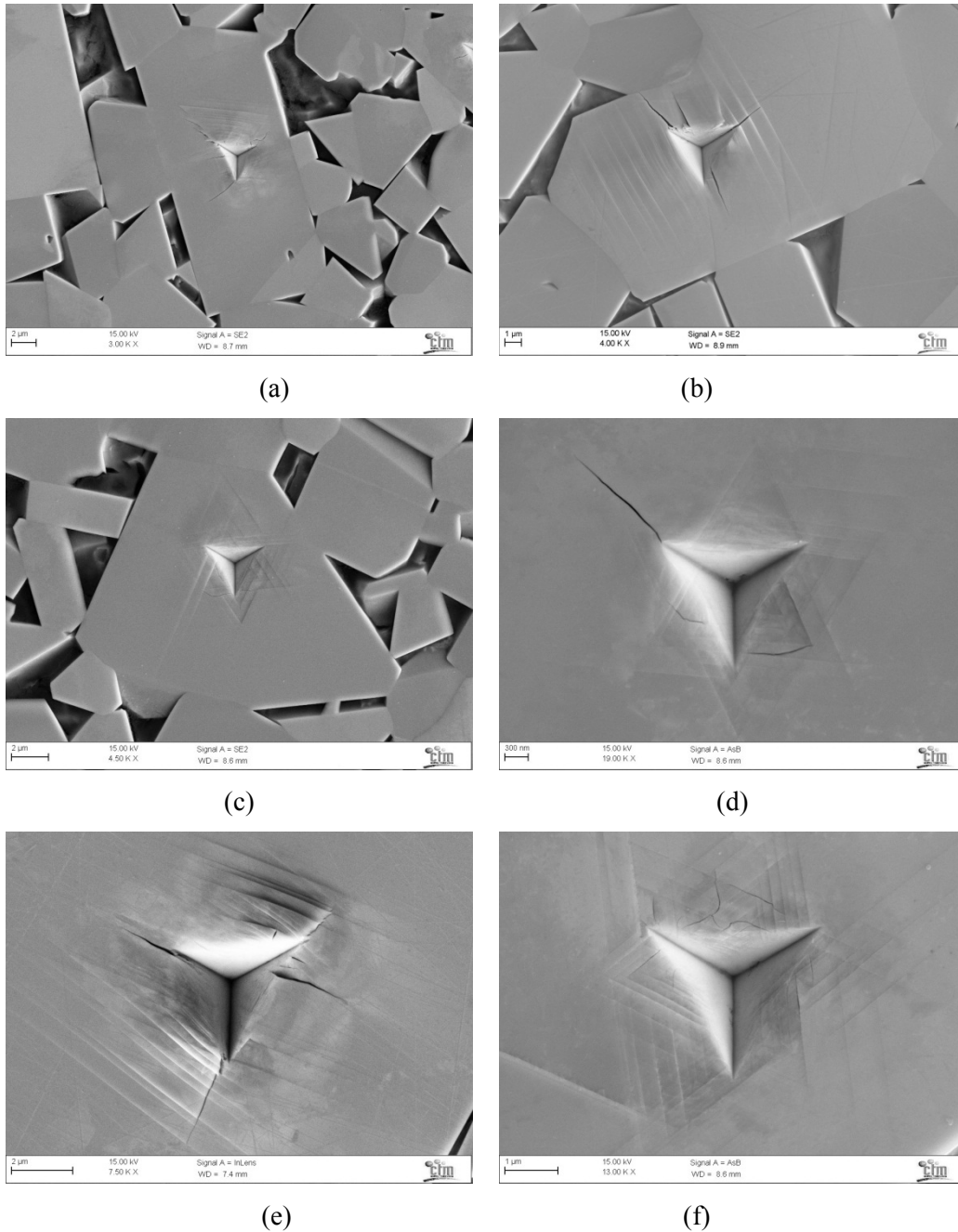


Figure 4.8.- SEM images of cube-corner indentations on different WC crystal planes in hardmetal: (a) prismatic facet (0.15 N), (b) prismatic plane (0.2 N), (d) basal facet (50 mN), (e) prismatic facet (0.25 N), (f) basal facet (50 mN).

The observed anisotropy in K_c can be rationalized on the basis of the different plastic deformation capability ascribed to each crystallographic plane. Based in the slip traces around Knoop hardness French et al. stated that in WC crystals the slip planes are $\{10\text{-}10\}$ (prism planes) with $\langle 0001 \rangle$ and $\langle 1120 \rangle$ as

preferred slip directions [57]. Considering the effective shear stress (ERSS) factor, which takes into account the most favourable slip systems adjacent to the indenter facets, it can be inferred that indentation of prismatic planes, as compared to the basal ones, should imply not only yielding at lower applied loads (and stresses) but also larger capability for developing plastic deformation before fracture [57, 62]. This would finally result in a decrease of hardness and a rise in fracture toughness. The above ideas are consistent with the measured values of H and K_c when indenting prismatic and basal planes. Figure 4.8 shows slip traces around the indentation impression, always parallel to prismatic facets.

The particular single-, double- or multiple slip scenarios are given by the effective volume of material beneath the surface affected by the applied indentation load as well as the relative orientation of the corresponding slip systems in each case. Additionally, it could explain the different plasticity/fracture behaviour found in basal and prismatic planes at different indentation load. Taking into account that active slip planes are the prismatic ones, yielding in basal planes requires even higher stresses than those needed for inducing cracks as was shown in Figure 4.8c and Figure 4.8d.

4.2.2. Residual stresses effects

In order to understand the crack behaviour on small volumes affected by residual stresses, Si needles embedded in an aluminium matrix were carefully studied by sharp indentation. The orientation of the needles was identified thorough EBSD. The results were compared with those obtained in Si (100) and Si (111) single crystals. During the cooling processing of the Al-Si alloy residual stresses appear inside the Si needles due to the different expansion coefficients of aluminium and silicon. Moreover, during the indentation process the localized plastic deformation generate residual stresses states in the surrounding elastic matrix, which can lead to initiation of cracks. Thus, these residual stresses of the indentation process will be affected by the residual stresses already present and imposed by the surrounding matrix and will affect the initiation and propagation of indentation cracks. Suresh *et al.* [63] developed a method for estimating residual stresses imposed by instrumented sharp indentation, and noticed that the indentation behaviour is affected by the presence of residual stresses. For a fixed penetration depth with tensile residual stresses there is an increase in the indentation load (Figure 4.9), whereas a decrease in indentation load takes place when compressive residual stresses are present. (Figure 4.10).

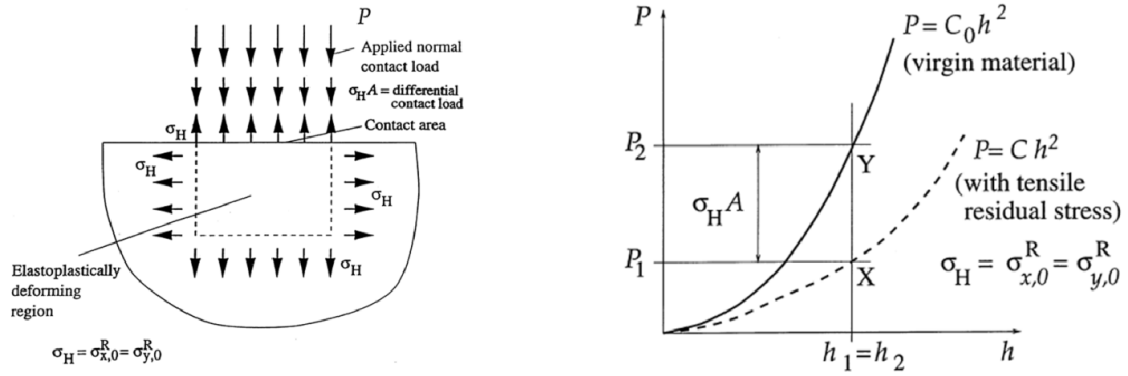


Figure 4.9.- Schematic of the role of tensile stress and $P - h_s$ behaviour under tensile residual stresses. (Adapted from [63]).

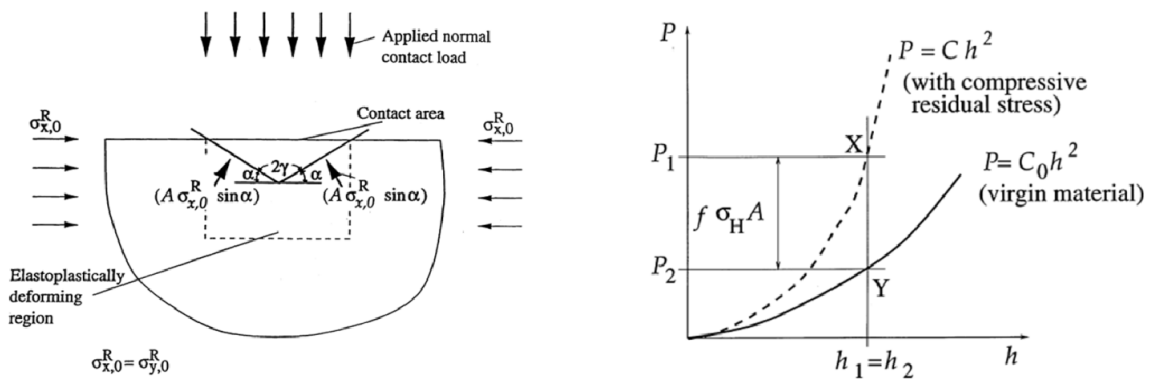


Figure 4.10.- Schematic of the role of tensile stress and $P - h_s$ behaviour under compressive residual stresses. (Adapted from [63]).

The effect of the residual stresses induced by the surrounding matrix on the $P-h_s$ indentation curve can be seen in Figure 4.13. Several Si needles with different shapes and sizes were analysed taking into account the position of the indentation test with respect to the needle. Because of the large dimensions of the needles, residual stresses vary in sign and magnitude along its length (Figure 4.13). This residual stresses also affect the final crack length induced by sharp indentation and the computed K_c by means of IM. Thus, when micro-sized particles are analysed it is important to take into account both crystal anisotropy and residual stresses.

Fracture toughness and residual stresses can be computed from the IM method by means of the measurement of the lengths of cracks that form during indentation as a function of indentation load. Indentation cracks would arrest due to the drop in indentation residual stresses intensity factor with crack extension as well as by the constraint imposed by the surrounding matrix. Hence, fracture toughness would have two components:

$$K_c = K_{indentation} + K_{res} = k^p \left(\frac{a}{l} \right)^{-1/2} \left(\frac{E}{H} \right)^{2/3} \frac{P}{c^{3/2}} + \Psi \sigma_{res} \sqrt{c} \quad (4.1)$$

where Ψ is a constant that depend on the crack geometry and σ_{res} is the residual stress imposed by the surrounded matrix.

In order to evaluate the validity of the method when σ_{res} are computed through the IM method, Berkovich and cube-corner indentations were performed along Si needles with (100) and (111) orientations since only Si (100) and Si (111) unstressed silicon material was available. Thus, the results for single crystals could be compared in an unstressed state and in a stressed state (Si needles in Al-Si alloy). EBSD images were obtained for Si needles in Al-Si alloy (see Figure 4.11), allowing crystal orientation to be known prior indentation tests.

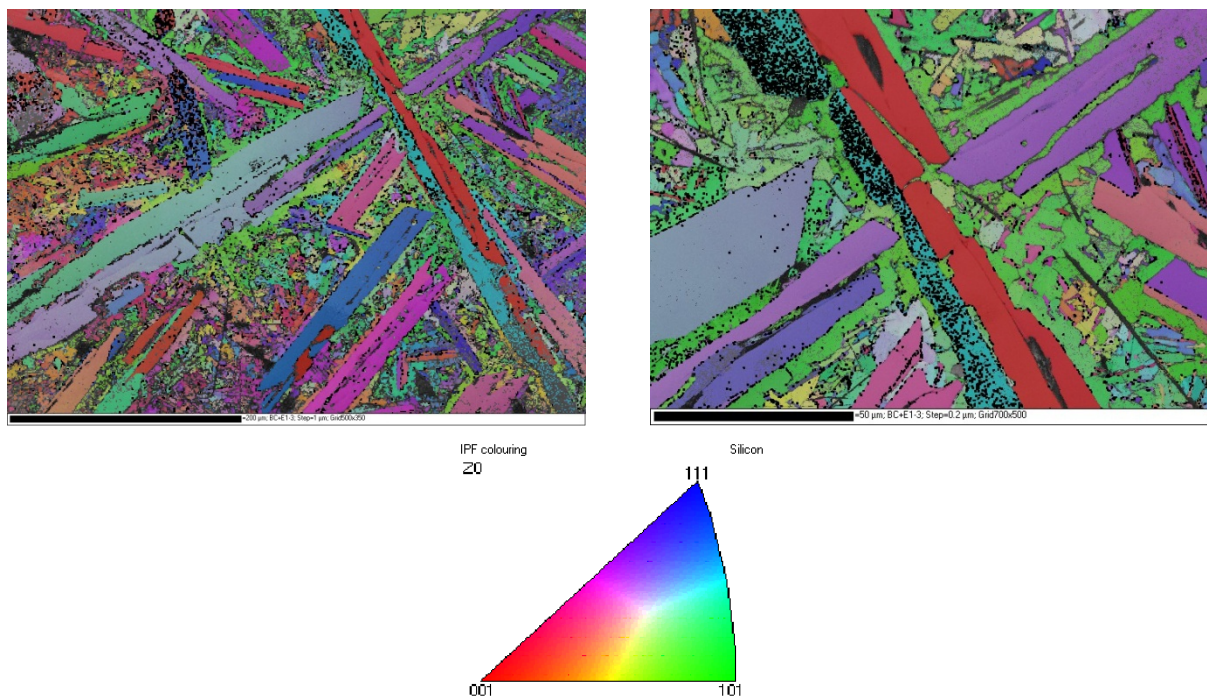


Figure 4.11.- EBSD images for Si needles in Al-Si alloy.

Residual stresses were easily computed by using equation 5.1 since reliable values for K_c measured by means of SENB are available. However, in order to investigate the possibility of using the IM method to evaluate K_c and σ_{res} from a single indentation test, equation 5.1 was used by plotting $K_{indentation}$ versus $\Psi c^{1/2}$; the intercept with the ordinate axis is K_c , whereas the slope is the residual stress. A negative slope will imply a tensile residual stress [64]. Only cracks that were longer than the plastic indentation size were used in the analysis.

As residual stresses vary along the length of Si needles, they were analysed in three different zones:

- The tips of the needle.
- The central zone of the needle.
- The middle position between central and tip zones.

Berkovich and cube-corner tip geometries were used to obtain different crack lengths for applying equation 5.1. According to the aforementioned needle division, indentation tests were performed along either (111) or (100) silicon needles. Figure 4.13 shows representative SEM images of three silicon needles indented in different regions and their corresponding $P-h_s$ curve. Table 4.7 and Table 4.8 show the σ_{res} evaluated in the different zones by using equation 5.1 and a K_c value of $0.93 \text{ MPa}\cdot\text{m}^{1/2}$ and $0.95 \text{ MPa}\cdot\text{m}^{1/2}$ for Si (100) and Si (100) respectively.

Table 4.7.-- σ_{res} evaluated for Si (111) needles.

$$(111) _ K_c = 0.93 \text{ MPa}\cdot\text{m}^{1/2}$$

Test location	σ_{res} (MPa)
Tip	-310
Centre	-518
Centre - tip	-353

Table 4.8.- σ_{res} evaluated for Si (100) needles.

$$(100) _ K_c = 0.95 \text{ MPa}\cdot\text{m}^{1/2}$$

Test location	σ_{res} (MPa)
Tip	-276
Centre	-174
Centre - tip	-121

Equation 5.1 was also applied to obtain K_c for Si (100) and Si (111) single crystals. The same experimental data points that were used to evaluate σ_{res} in Table 4.7 and Table 4.8, were fitted to satisfy equation 5.1. Figure 4.12 shows the results of the adjustment, any crystal orientation or localization along the Si needle were taken into consideration. Limitations on the applied load due to chipping effects led to the acquisition of few data point in each orientation and location. Thus, in order to get the best fitting all the data available were treated together. Although Figure 4.12 presents a poor fitting to the experimental data, the obtained results were good enough, i.e., coherent values for K_c and σ_{res} were obtained indicating that further investigations in this field would be worth to perform.

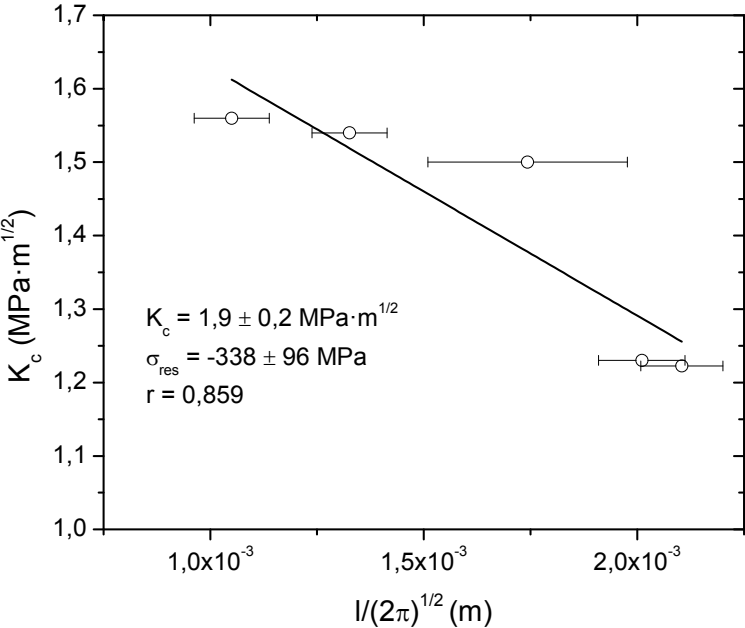


Figure 4.12. Experimental fit to equation 5.1. Data points correspond to cube-corner indentation performed at different loads and Si needles.

The above results show that the residual stresses experienced by silicon needles embedded in an Al matrix are negative in sign, i.e., they are compressive as one would expect from the $P-h_s$ behaviour. When $P-h_s$ curves corresponding to the silicon needle test were compared with those of silicon single crystals, a left shift of the curve was observed. This shifting indicates that silicon needles are affected by compressive residual stresses, this observation is also corroborated by other authors [63]

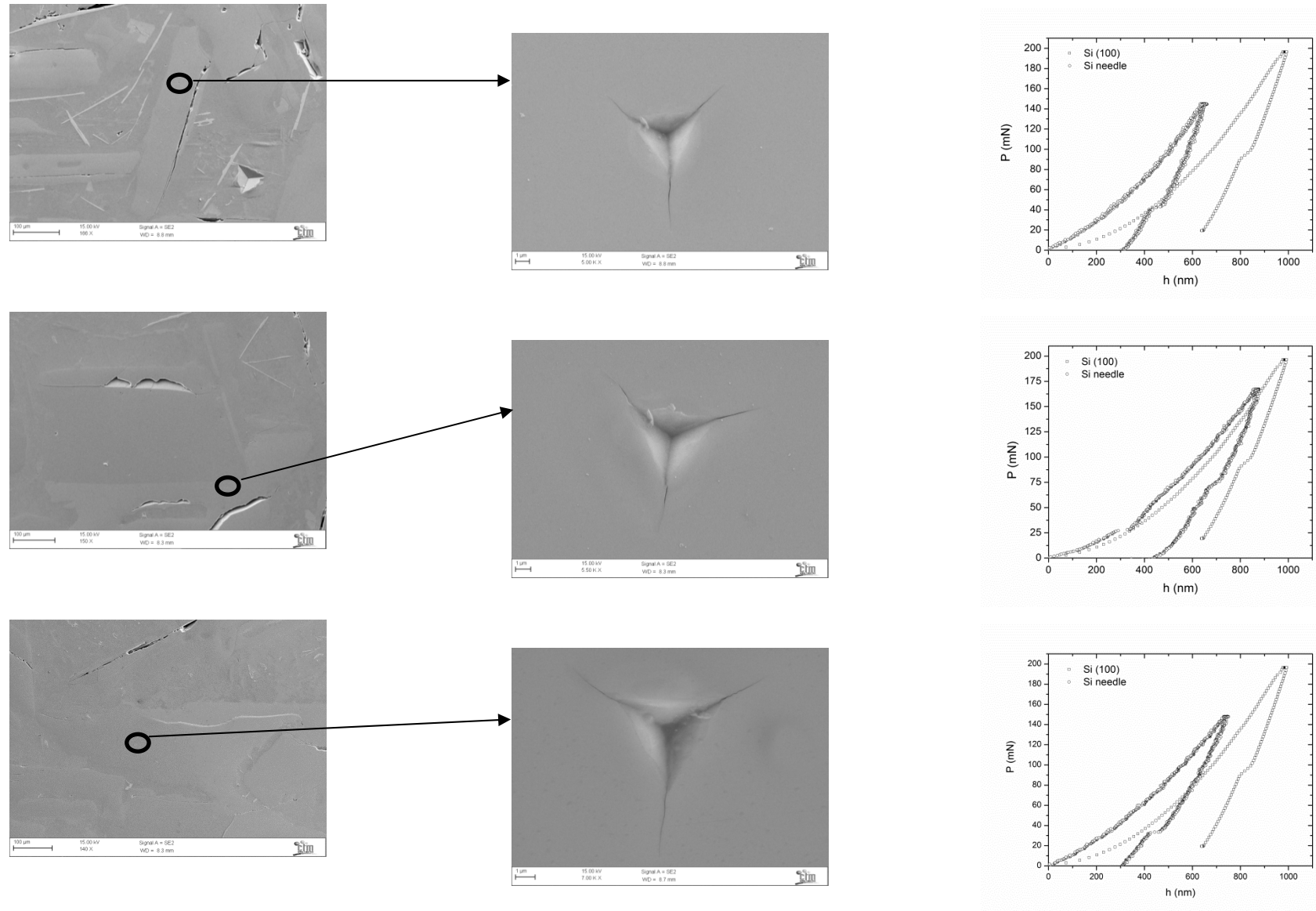


Figure 4.13.- SEM images of three Si needles indented at different locations and their corresponding $P-h$ curves in comparison with one obtained for a Si single crystal.

Table 4.7 and Table 4.8 show a wide range of values for σ_{res} , besides Figure 4.12 also reports a significant dispersion in the computed σ_{res} . The reason for such scattered results is not only attributable to anisotropy but to microstructural effects. The analysed Si needles were big enough to present a strong variation of σ_{res} in both directions along and across the needle. Some FEM simulation to illustrate the variation of the σ_{res} experimented by the Si needles during its solidification were performed. Following the equilibrium phase diagram (Figure 2.4), FEM's were performed cooling a single needle embedded in an Al matrix from 863°C to 263°C. Figure 4.14 shows the σ_{res} variations computed by FEM, in these results the Von Mises stresses are shown, thus only the magnitude of the stresses and not its sign should be taken into account. The results confirmed that a variation on the σ_{res} exists along and across the Si needles, and moreover, depending on the length of the needle σ_{res} could vary between 100 and 700 MPa.

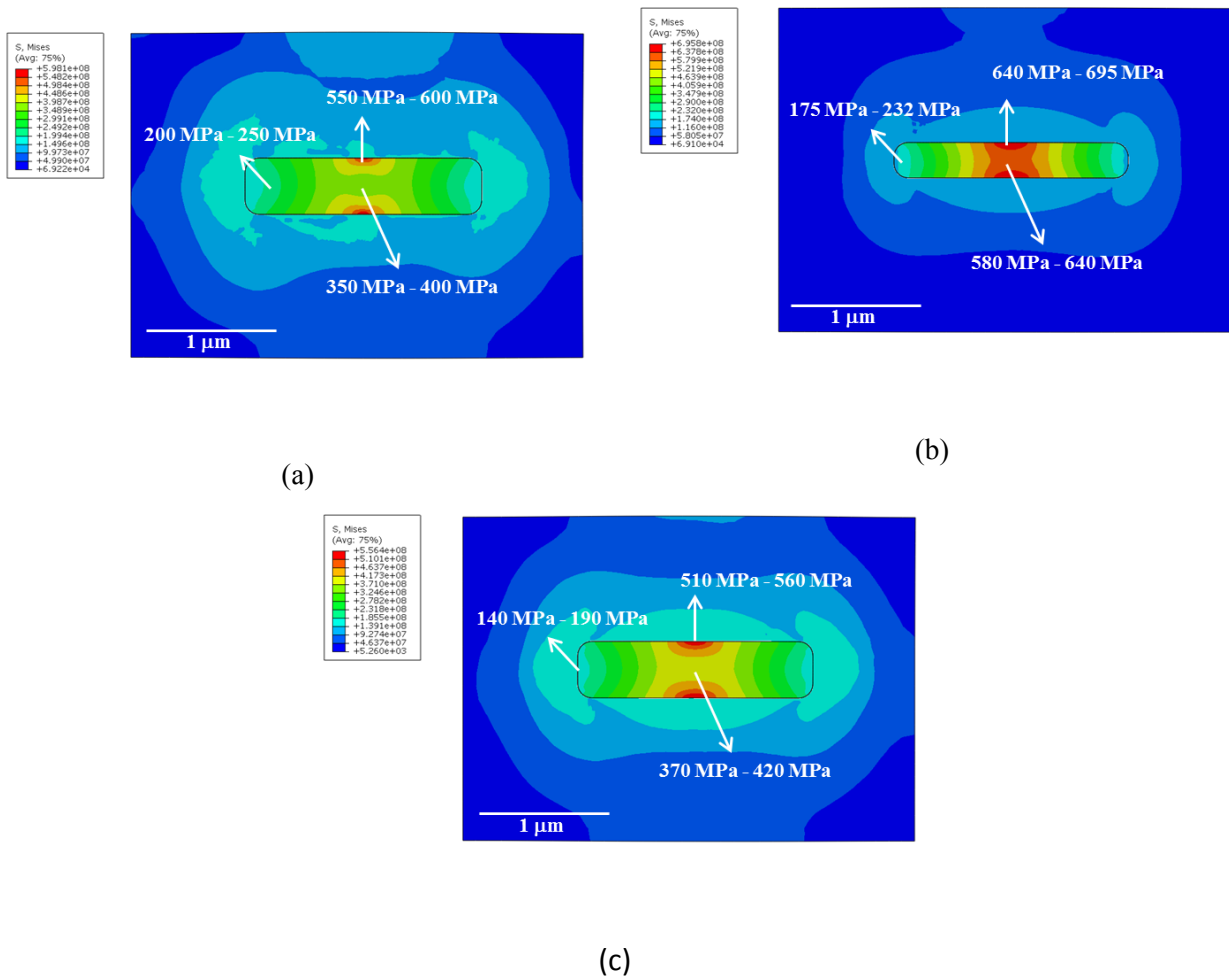


Figure 4.14.- FEM simulations of the residual stresses experimented by Si needles caused the surrounding matrix during the cooling process.

In order to decrease the uncertainty in the σ_{res} results a hypereutectic Al-Si alloy with less Si content than that used in this work should be analysed. If the weight content of Si is reduced, the size of the needle will be smaller leaving out the σ_{res} variation along its dimensions. At the same time, the size of the needle should be big enough to fit an indentation imprint and the generated cracks. For that reason an Al-Si alloy with a 20% in weight of Si is being studied. The aim of the use of this new sample is to verify if as the particle size is reduced the scatter in the σ_{res} results is lowered. In that way a methodology to evaluate both K_c and σ_{res} by a sharp single indentation test could be developed.

**Micromechanical characterization of micro-sized
particles by means of nanoindentation:
Practical applications**

The act of repeating erroneously the words of another.

Ambrose Bierce, The Devil's Dictionary (1911)

Mechanical characterization of micro-volume systems such as thin films or micro-sized phases is a critical step for optimizing and developing materials and high-performance coatings. In the course of this thesis nanoindentation has proved to be a suitable technique to characterize micro-sized materials in terms of H , E and K_c . Thus, the aim of this chapter is to apply nanoindentation technique in multiphase materials in order to mechanically characterize their constitutive phases, particularly when they are in the form of micro-sized particles.

With the aim of developing a reliable methodology to mechanically characterize hard particles by means of nanoindentation different primary carbides present in tool steels were evaluated. This kind of material was chosen since they are widely used in industry for forging tools and because they have indentable micro-sized hard particles. Tool steels are formed by carbides embedded in a metallic matrix. These carbides play an important role in the mechanical response of tool steels, since they act as hard particles and dictate the wear resistance as well as they can initiate fracture. Thus, the values of H and K_c of the carbides affect both the wear and fracture resistance of tool steels. Optimization of properties of carbides is then crucial to develop high-performance tool steels.

Additionally, in order to complete the study different suitable hard particles, as metallic borides and nitrides, to be used to design tailored steels were also analysed by nanoindentation. Finally, the fracture behaviour of a hardmetal was analysed in terms of the mechanical properties of their WC crystals.

5.1. Micromechanical characterization of carbides in tool steels

Hard particles in UNIVERSAL, 1.2379 and CAST WRA 46 were analysed by means of nanoindentation (see Chapter 3). The results, including H , E and K_c are shown in Table 5.1. Results of other hard particles were also included since they could be used to form part of multiphase materials.

Table 5.1.- Micromechanical characterization of hard particles evaluated by means of nanoindentation.

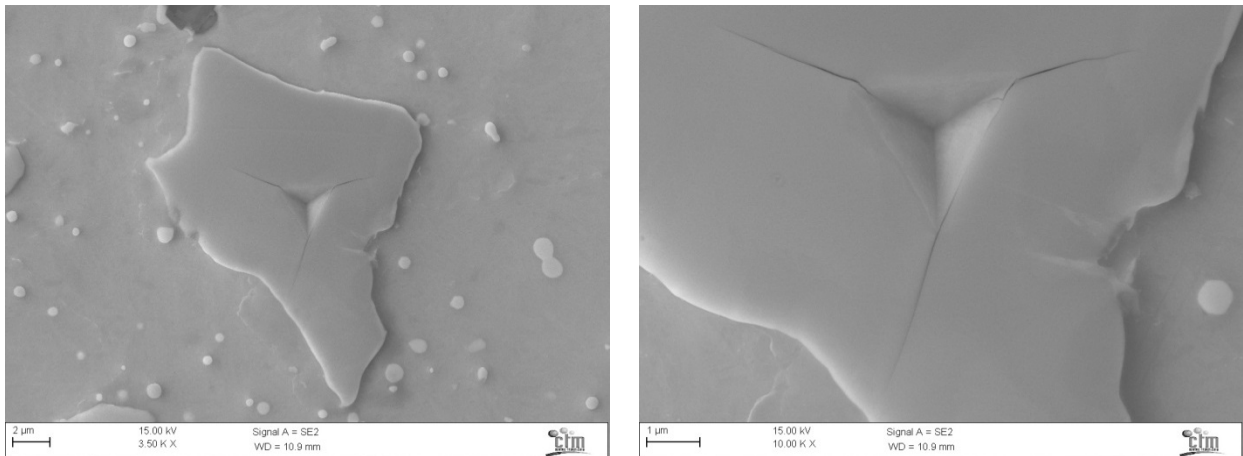
HARD PARTICLE	K_c (MPa·m ^{1/2})	H (GPa)	E (GPa)
TiB ₂	1.3 ± 0.4	28.4 ± 2.3	255 ± 20
c-BN	1.2 ± 0.4	31.9 ± 4.5	191 ± 28
c-BN	0.5 ± 0.1 ^a	31.9 ± 4.5	191 ± 28
SiO ₂	1.1 ± 0.1	14.9 ± 0.3	120 ± 15
SiC	3.5 ± 0.8	37.2 ± 0.3	478 ± 4
NbC	2.5 ± 0.6	15.8 ± 1.8	278 ± 37
WC (prismatic facet)	9.9 ± 2	17.2 ± 0.1	564 ± 26
WC (basal facet)	7.5 ± 0.8	25.6 ± 0.2	532 ± 23
M ₇ C ₃ (UNIVERSAL)	-	20.3 ± 0.9	272 ± 18
MC (UNIVERSAL)	2.3 ± 0.6	26.1 ± 0.9	316 ± 20
MC (CAST WRA 46)	1.5 ± 0.5	22.9 ± 1.9	319 ± 6
M ₇ C ₃ (1.2379)	2.5 ± 1.6	18.2 ± 2.4	294 ± 17

^a K_c evaluated in the direction perpendicular to the large edge of the nitride particle.

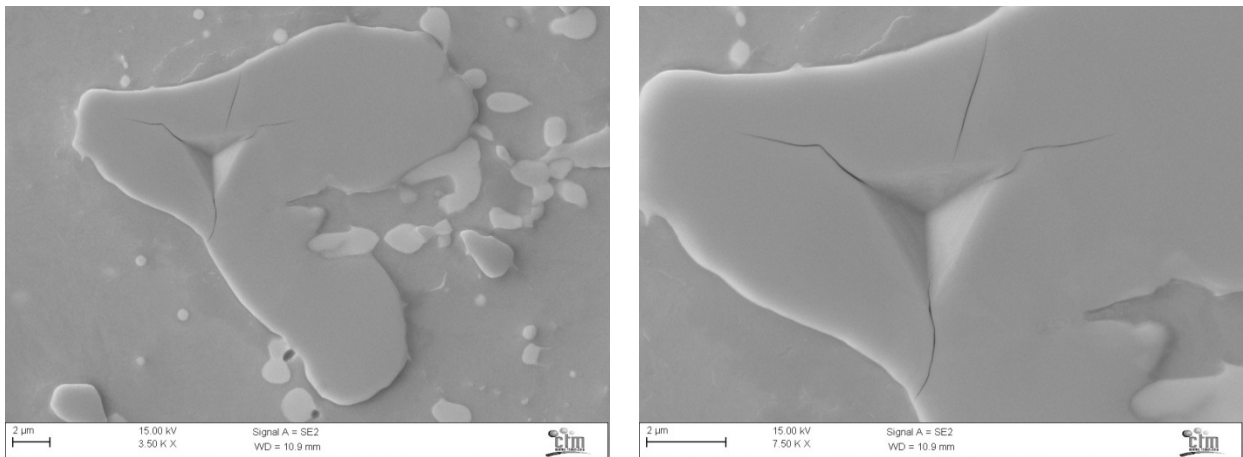
Fracture toughness values presented in Table 5.1 were computed either with a Berkovich tip or a cube-corner tip depending on the load needed to generate fracture on the analysed sample. Images showing the fracture of the primary carbides of CAST WRA 46, 1.2379 and UNIVERSAL tool steels are shown in Figure 5.3, Figure 5.1 and Figure 5.2 respectively. From these images several observations can be made:

- Tip geometry: it was experimentally assessed that when cube-corner tips are used the threshold load to achieve fracture decreases (see Figure 5.2b and 5.2c). Consequently, even smaller hard particles can be analysed since both imprint and generated cracks can be fitted into tinier volumes. Furthermore, decreasing indentation size leads to a less interaction between the grain boundary and the cracks and more reliable K_c values can be computed.
- Crystal anisotropy: as in single crystals anisotropy effects are also present in the analysed carbides. Figure 5.1a, 5.1b and Figure 5.3a exhibit carbides in which the crack path was deflected following favourable crystallographic planes. Moreover, Figure 5.1c, Figure 5.2b, 5.2e and Figure 5.3e, 5.3f show indentation imprints in which cracks emanate from only one of the corners indicating a preferential plane for cracking. Nevertheless, sometimes the observed anisotropy could be also due to the gradient of chemical composition that exists inside some carbides. This gradient could deflect or arrest the crack since act as a boundary between two different chemical regions.

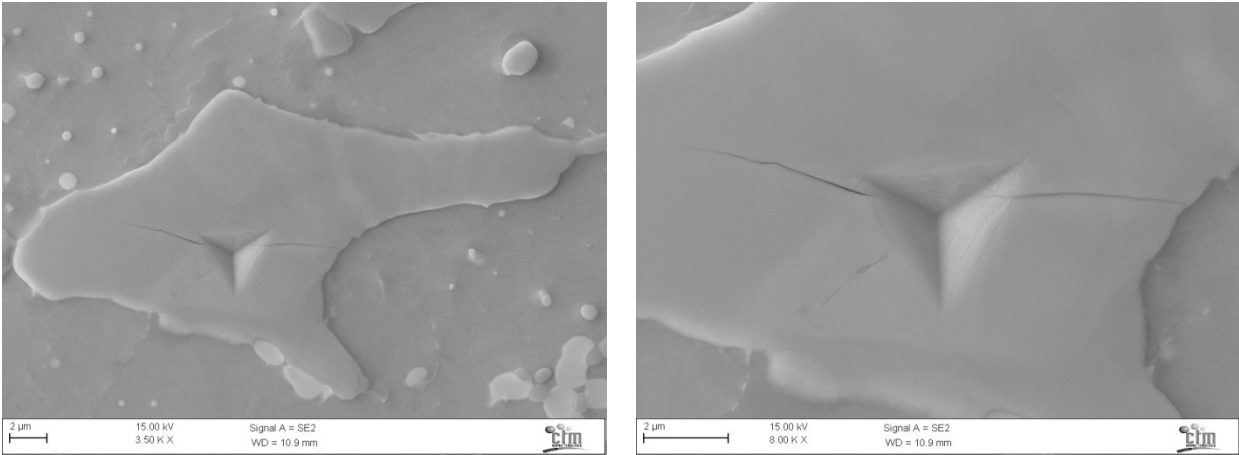
- **Plasticity:** Figure 5.1 -Figure 5.3 show that M_7C_3 carbides deform more plastically than MC carbides. This was easier to observe by using a cube-corner tip since this kind of geometry displaces a much more volume of material than a Berkovich. Thus, plastically deformed material around indentation imprints in most of the M_7C_3 carbides could be observed by using a cube corner tip. Additionally, it was observed that it was more difficult to induce fracture in these M_7C_3 carbides. Moreover, when M_7C_3 carbides fractured, hardly any plastic deformation was observed (Figure 5.2d, 5.2e and Figure 5.3e) and fracture takes place mainly in the direction parallel to the major axis of the carbide when it is oriented perpendicular to the forging direction.



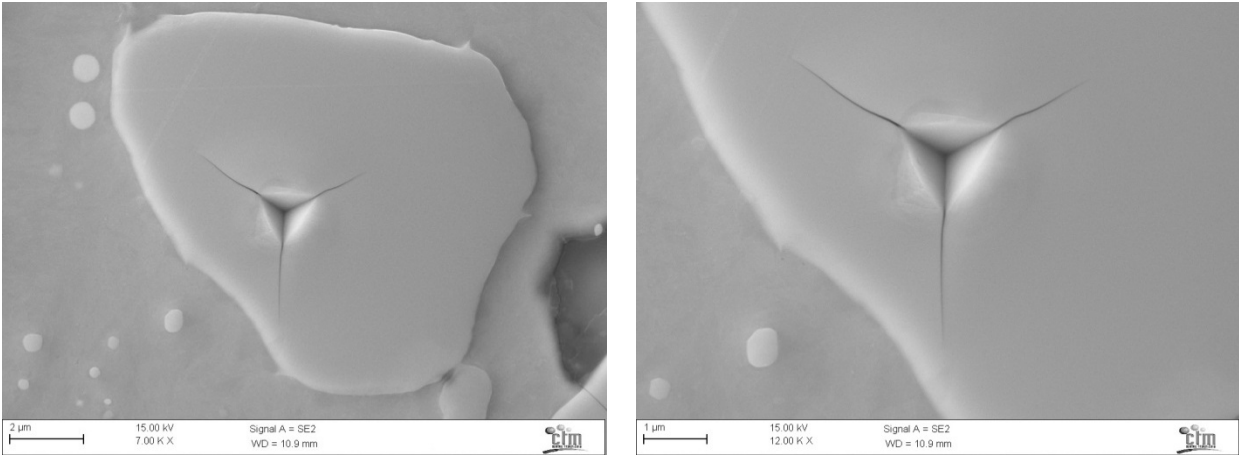
(a) MC (Berkovich at 0.12 N)



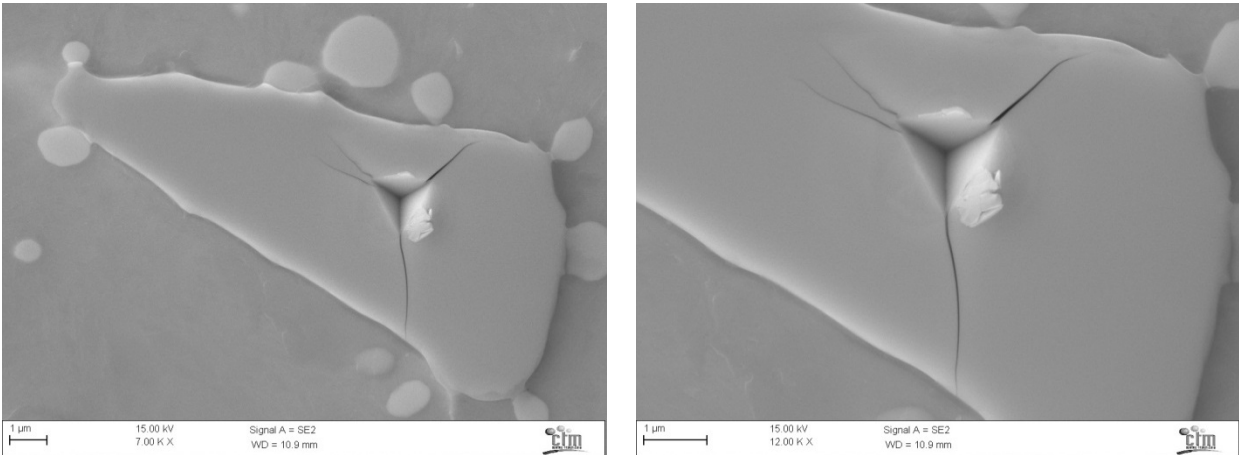
(b) MC (Berkovich at 0.15 N)



(c) MC (Berkovich at 0.17 N)

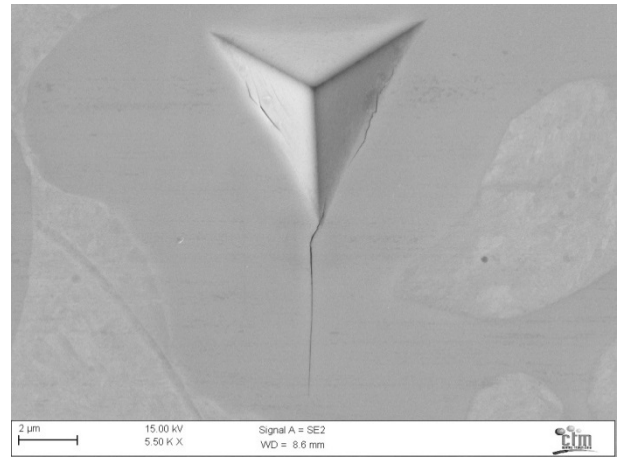
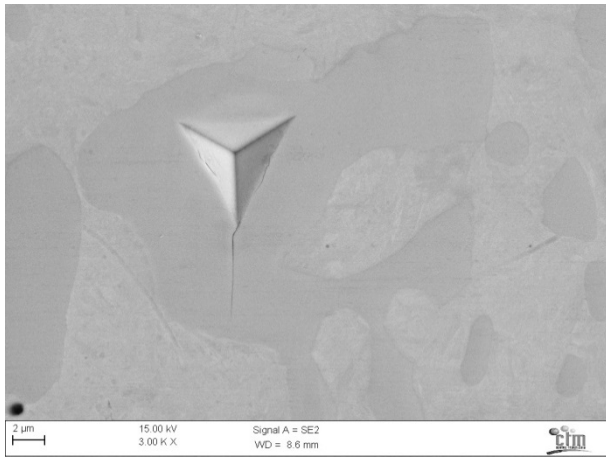


(d) MC (Cube-corner at 40 mN)

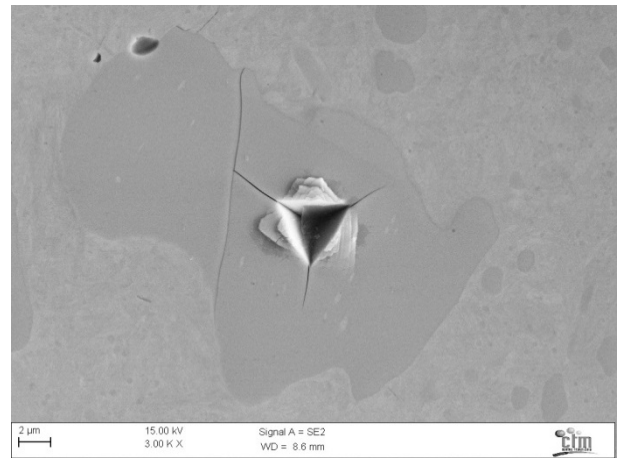
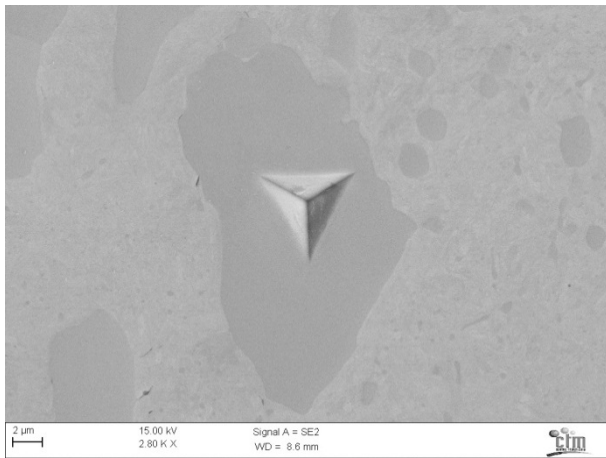


(e) MC (Cube-corner at 40 mN)

Figure 5.1.- SEM images of fracture induced by sharp indenters in MC carbides in CAST WRA 46 tool steel.

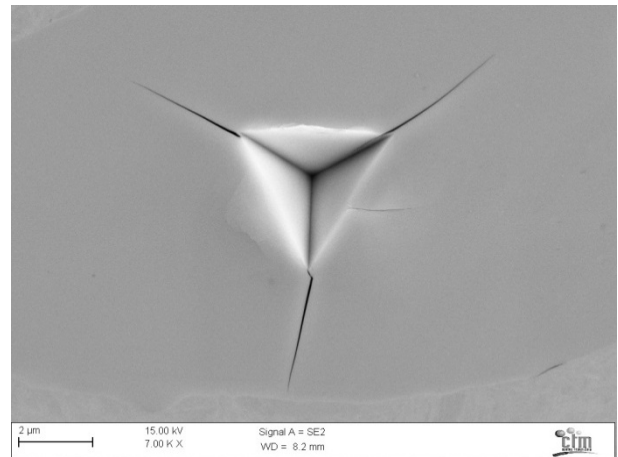
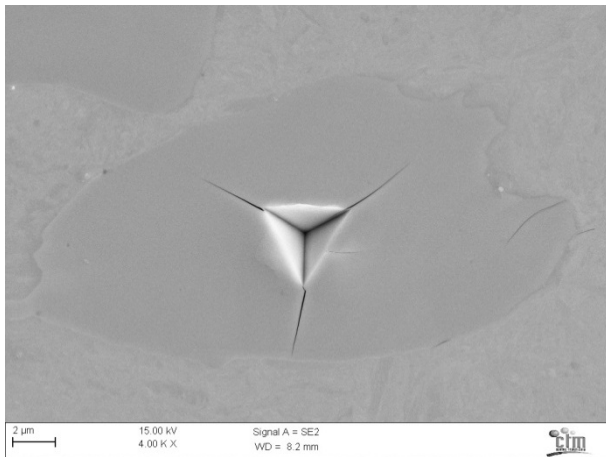


(a) M_7C_3 (Berkovich at 0.25 N)

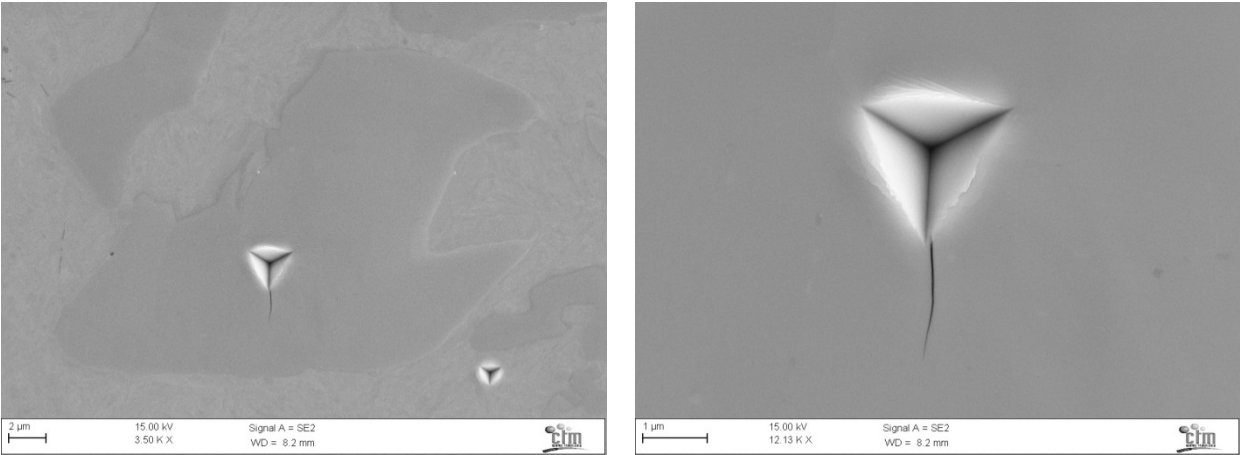


(b) M_7C_3 (Berkovich at 0.22 N)

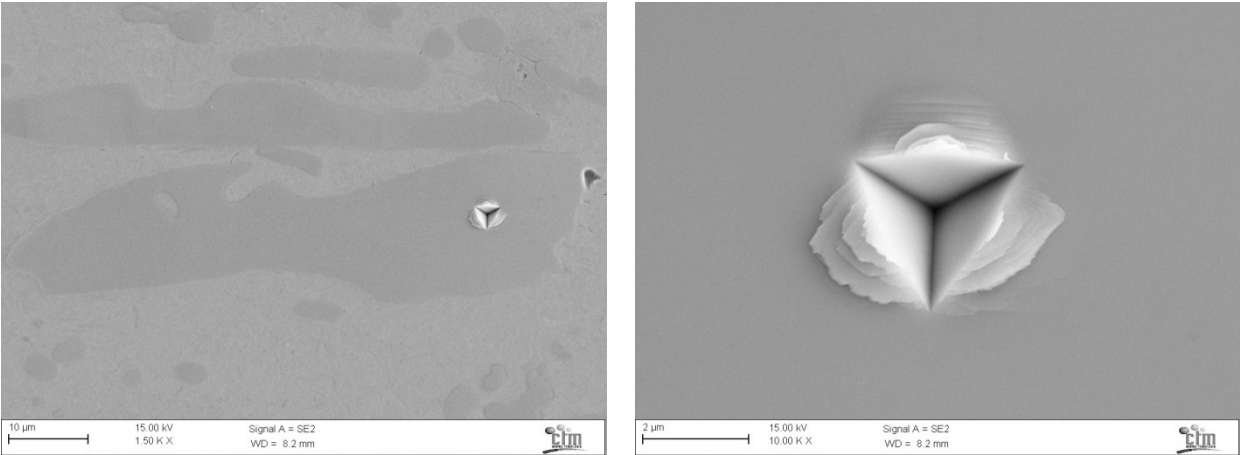
(c) M_7C_3 (Cube-corner at 0.20 N)



(d) M_7C_3 (Cube-corner at 0.1 N)

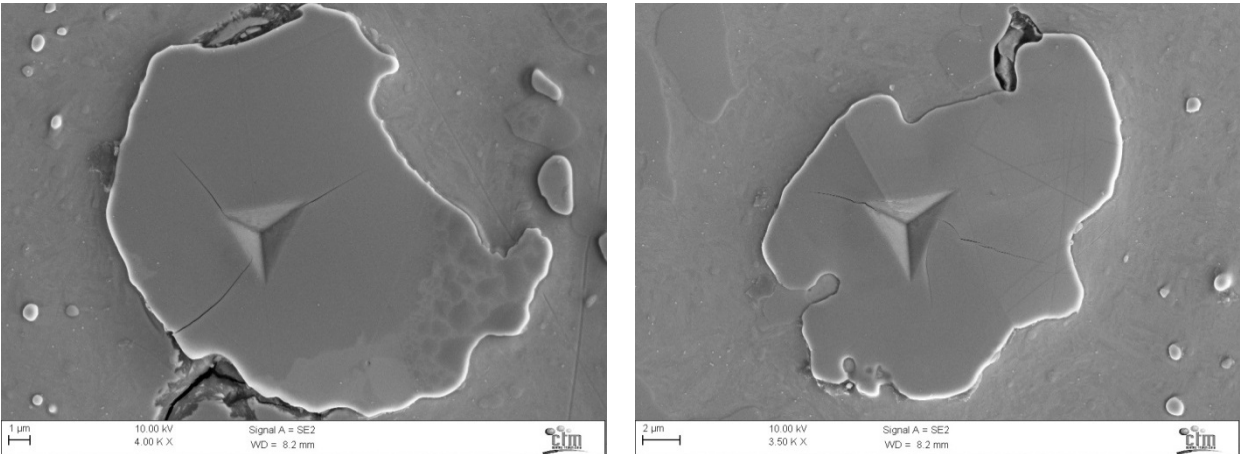


(e) M_7C_3 (Cube-corner at 50 mN)



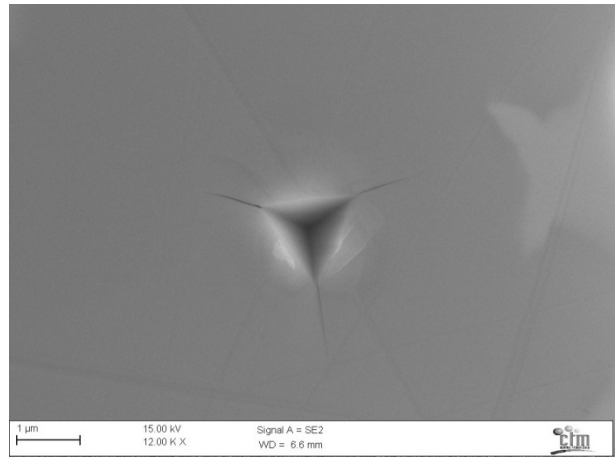
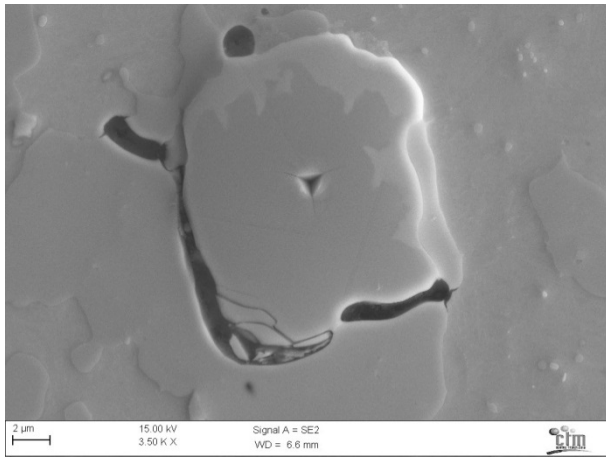
(f) M_7C_3 (Cube-corner at 0.1 N)

Figure 5.2.- SEM images of fracture induced by sharp indenters in M_7C_3 carbides in 1.2379 tool steel

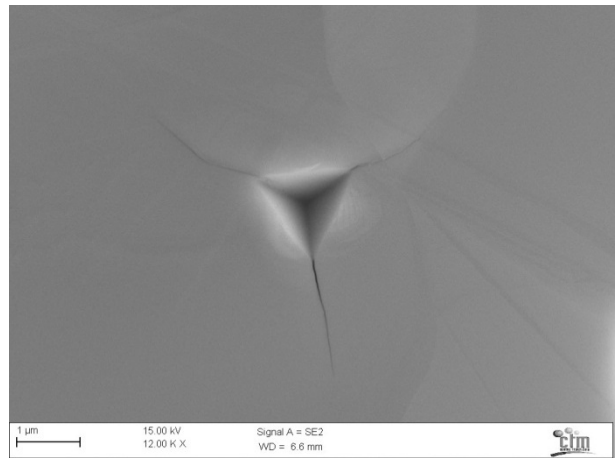
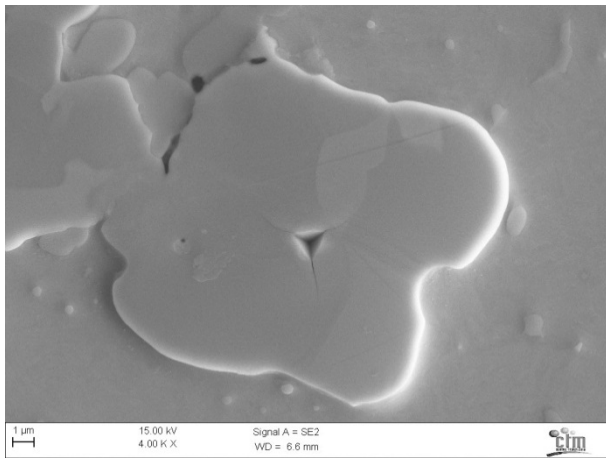


(a) MC (Berkovich at 0.2 N)

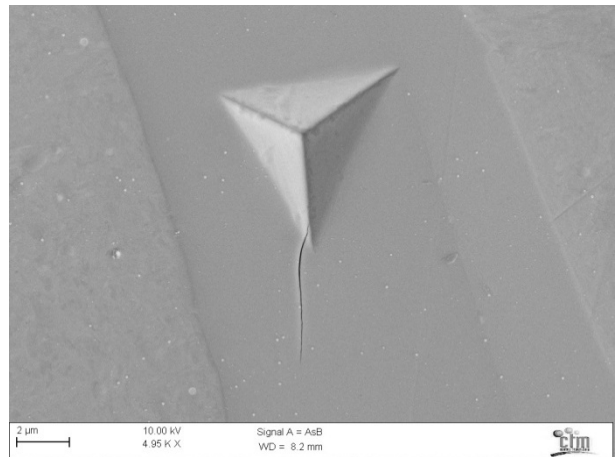
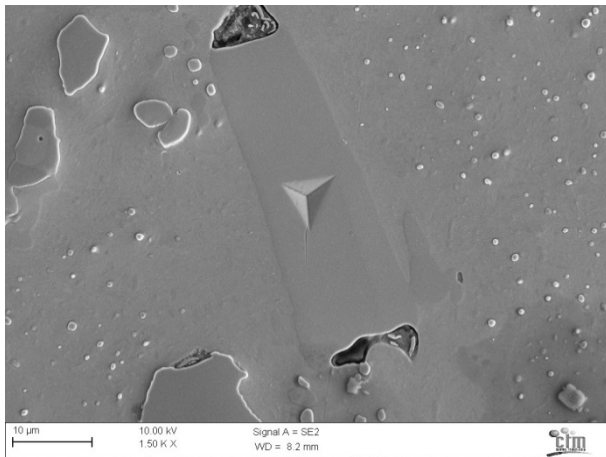
(b) MC (Berkovich at 0.27 N)



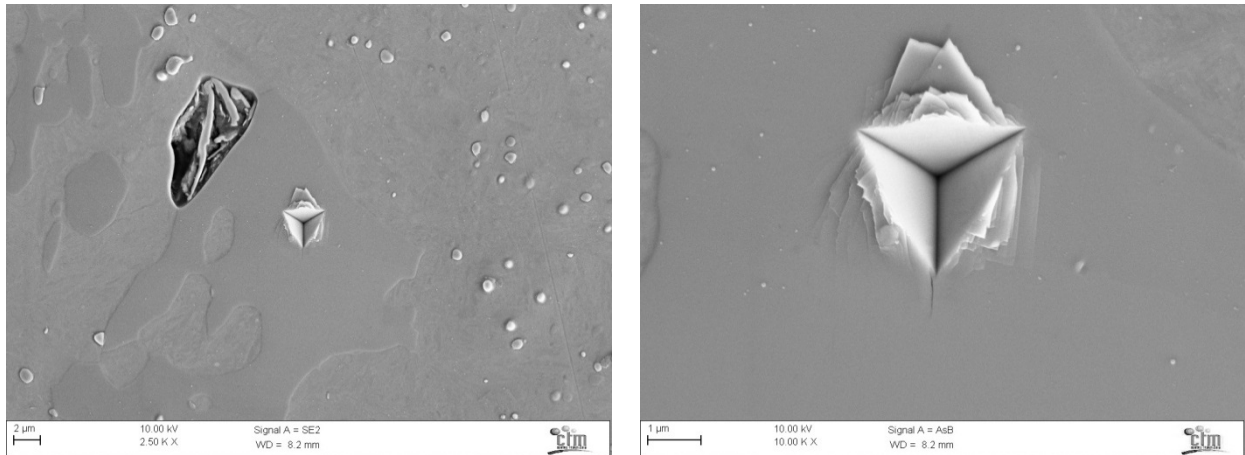
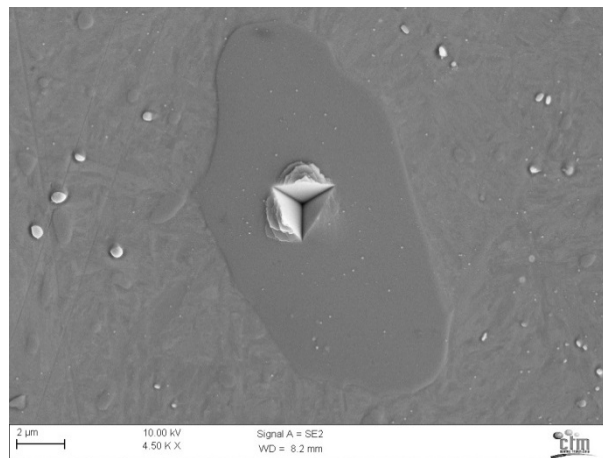
(c) MC (Cube-corner at 40 mN)



(d) MC (Cube-corner at 40 mN)



(e) M_7C_3 (Berkovich at 0.3 N)

(f) M_7C_3 (Cube-corner at 0.1 N)(g) M_7C_3 (Cube-corner at 70 mN)**Figure 5.3.-** SEM images of fracture induced by sharp indenters in MC and M_7C_3 carbides in UNIVERSAL tool steel

In order to corroborate whether in multiphase materials Berkovich and cube-corner tips would give the same results of K_c , different carbides embedded in a CAST WRA 46, 1.2379 and UNIVERSAL tool steels were indented with both indenter geometries (see Table 5.2). It is worth noticing that although three different tool steels were analysed, only two kinds of primary carbides with the same crystallographic structure were studied, M_7C_3 and MC carbides, embedded in different metallic matrix (slight differences in hardness produced by the different chemical composition and tempering treatments). This fact will permit to investigate the effect of the matrix on the mechanical behaviour of the carbides. Both M_7C_3 carbides and MC carbides were present in UNIVERSAL tool steel, whereas only M_7C_3 and MC carbides were present in 1.2379 and CAST WRA 46, respectively.

Table 5.2.- Comparison of K_c of MC and M_7C_3 carbides in CAST WRA 46, 1.2379 and UNIVERSAL tool steels computed using either Berkovich or cube-corner tips.

CARBIDE	K_c (MPa·m ^{1/2})	
	Berkovich tip	Cube-corner tip
MC (CAST WRA 46)	1.5 ± 0.5	1.9 ± 0.5
MC (UNIVERSAL)	1.4 ± 0.2	2.3 ± 0.6
M_7C_3 (1.2379)	1.4 ± 0.5	2.5 ± 1.6
M_7C_3 (UNIVERSAL)	1.5 ± 0.5	2.4 ± 0.7

From the results presented in Table 5.2 some remarks could be done:

Firstly, Table 5.2 shows that all the analysed carbides present the same K_c , except in the case of the MC carbides present in UNIVERSAL tool steel when is analysed by cube-corner tips. This result is not surprising since all of them are very similar from a chemical point of view, thus their mechanical behaviour is expected to be alike. Additionally, the fact that carbides exhibit similar mechanical properties, in terms of H , E and K_c , means that matrix effects are not relevant in its evaluation by means of nanoindentation. All the analysed tool steels, CAST WRA 46, 1.2379 and UNIVERSAL, present more or less the same kind of metallic matrix based in a tempered martensitic matrix with secondary carbides. Consequently, matrix effects on mechanical properties and on the fracture behaviour should be the same in the analysed carbides.

Secondly, differences between K_c values computed using either Berkovich or cube-corner tips were observed. In order to elucidate the reason of this discrepancy, a crack morphology study was performed. Although in previous chapters was determined that three-sided pyramids generate quarter-penny cracks, possible interactions between the carbide and the cracks must be taken into account. Figure 5.4 and Figure 5.5 show FIB tomographies of a MC carbide in a UNIVERSAL tool steel and a WC in a hardmetal, respectively. Both Figure 5.4 and Figure 5.5 show schematically the process of obtaining the crack morphology by means of FIB.

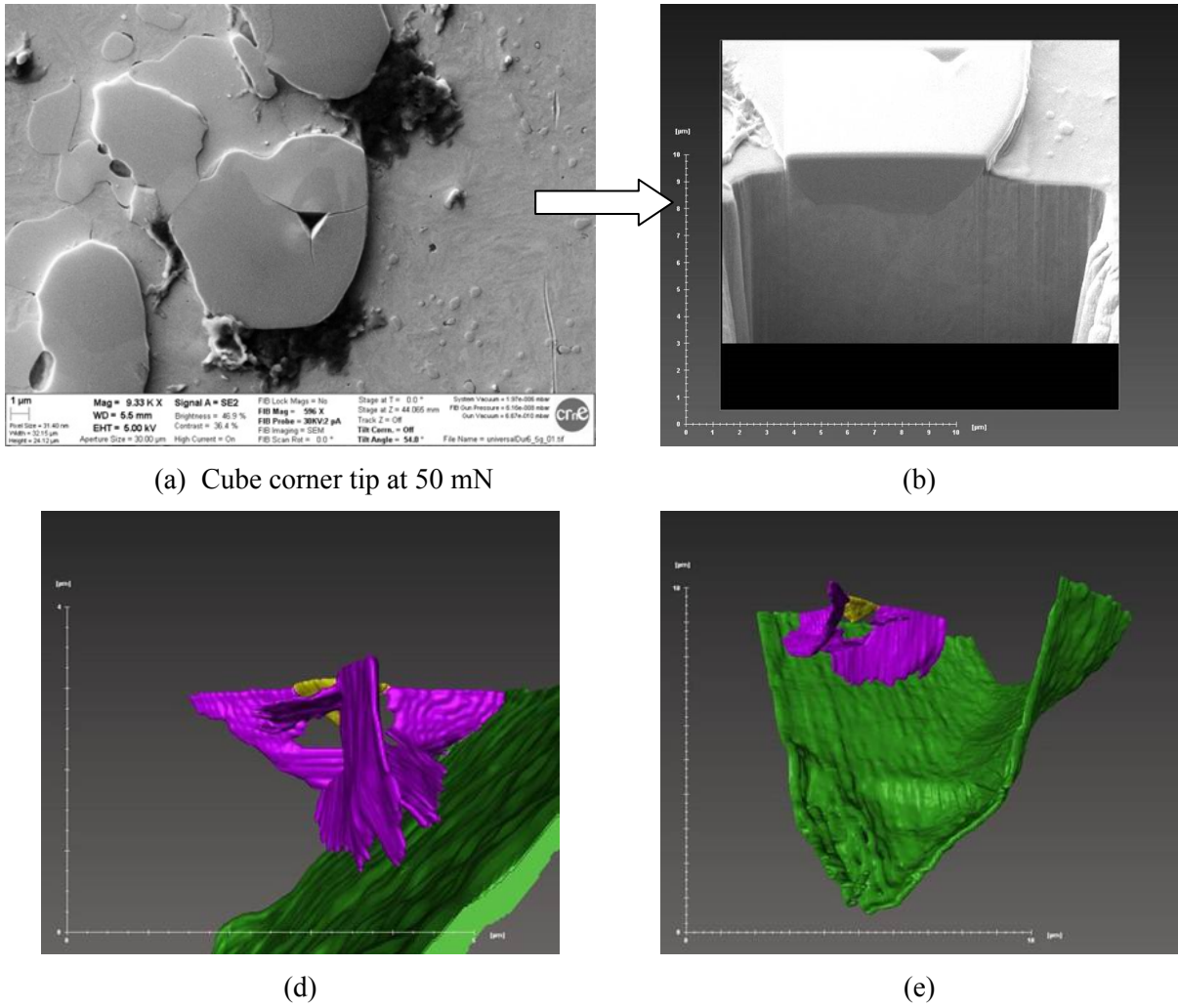
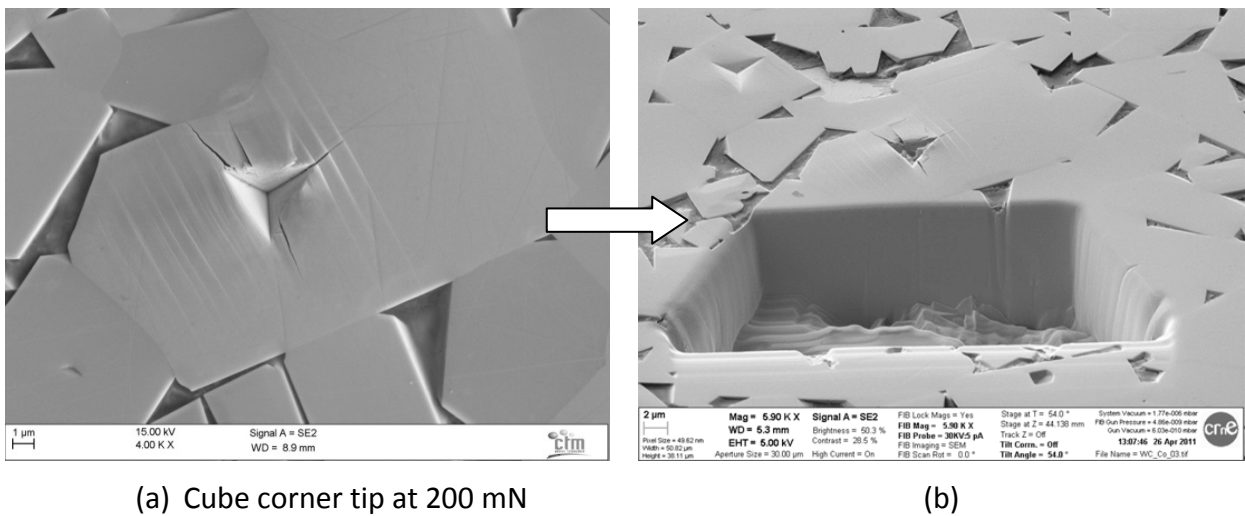


Figure 5.4.- FIB tomographies of a cube-corner indentation at 50 mN performed on a MC carbide in a UNIVERSAL sample. Yellow area corresponds to the indentation impression, violet indicates the crack morphology and green corresponds to the carbide-matrix boundary.



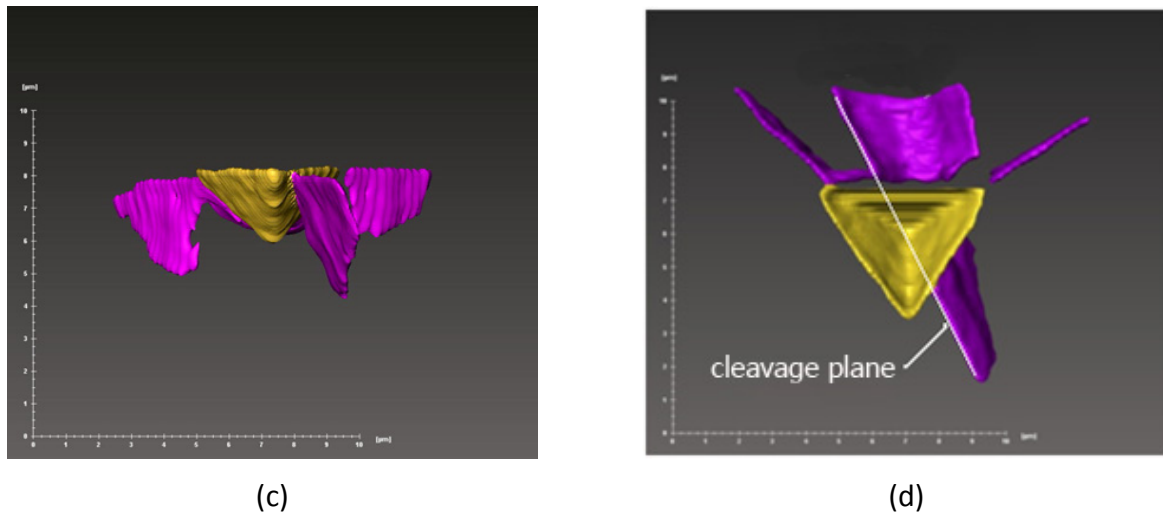


Figure 5.5.- FIB tomographies of a cube-corner indentation at 200 mN performed on a WC in a hardmetal sample. Yellow area corresponds to the indentation impression, violet indicates the crack morphology.

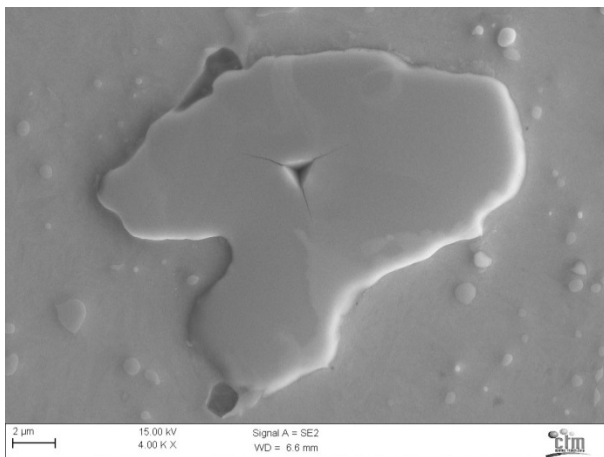
From Figure 5.4 it is noticed that indentation is well placed in the carbide and cracks are fully developed without interaction with the carbide boundaries. It is also observed that quarter-penny cracks are formed and they are deflected following preferential planes due to anisotropic effects. Also, the formation of lateral cracks was experimentally assessed. Figure 5.5 clearly shows the formation of Palmqvist cracks and the presence of anisotropic effects. WC crystals exhibit a higher K_c than MC carbides thus, as expected, crack morphology changes from quarter-penny to Palmqvist as the analysed particle increases its toughness.

With respect to crack morphology dependency on the applied load Figure 5.6 - Figure 5.8 show crack evolution, monitored by means of FIB, of three different M_7C_3 carbides in a UNIVERSAL sample indented at 40 mN, 30 mN and 20 mN respectively. Some remarks can be made from Figure 5.6 - Figure 5.8:

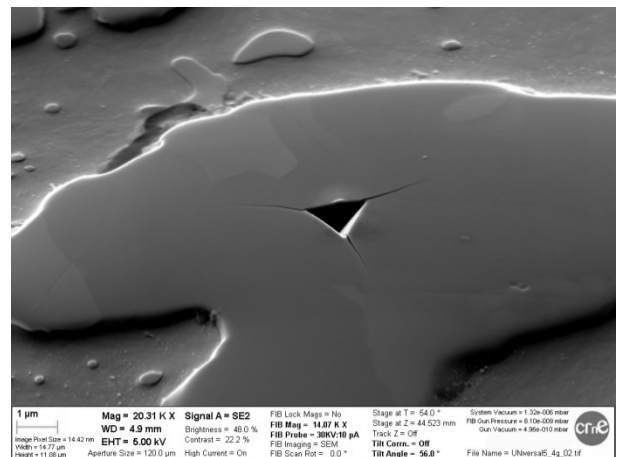
1. Crack morphology evolves from Palmqvist to quarter-penny cracks as P is increased from 20 mN to 40 mN. In Figure 5.8 crack evolution corresponding to a cube-corner indentation performed at 20 mN is shown. Figure 5.8c and 5.8d present a superficial crack as that defined in Figure 1.8b as a Palmqvist. On the other hand, FIB images of cube-corner indentations performed at 30 mN (Figure 5.7) and at 40 mN (Figure 5.6) clearly shows how cracks emanate below the plastic zone and spread to the surface (see Figure 5.6g -5.6 k and Figure 5.7i -5.7 k) as that observed in Figure 3.3 - Figure 3.5 and defined as quarter-penny cracks.

2. It was experimentally assessed that cracks do not growth inside the plastic zone (see Figure 5.6i - 5.6k and Figure 5.7i – 5.7l). It was observed that cracks were deflected due to anisotropy effects (see Figure 5.7f). Thus, complicated crack systems are formed making difficult K_c computation by equations that only take into account one single kind of crack morphology as that used here (equation 1.25).

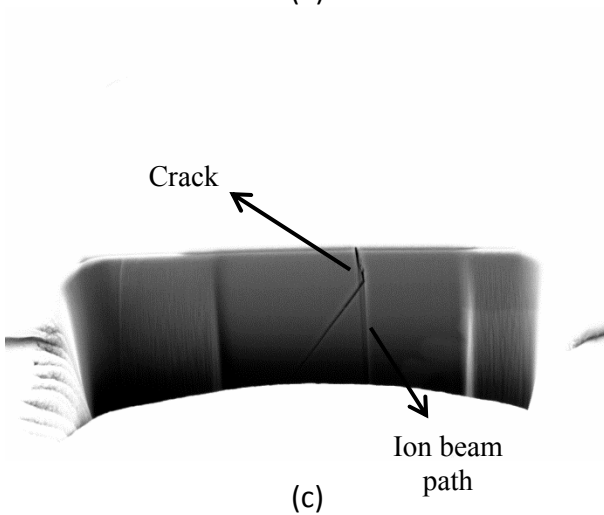
3. The presence of defects inside the carbides, as voids (Figure 5.7d), could interact with the crack system generated during the indentation process deflecting the crack path or arresting it. Chemical discontinuities within carbides would have the same effect as they act as boundaries.



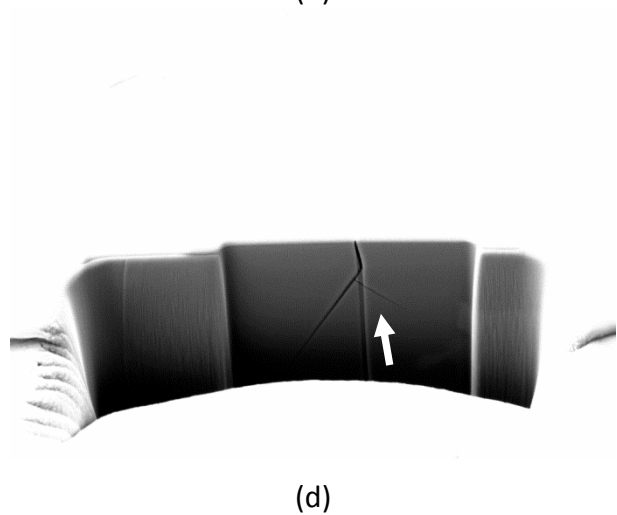
(a)



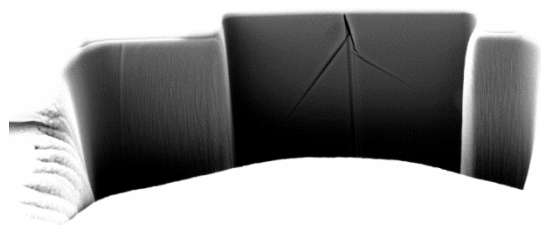
(b)



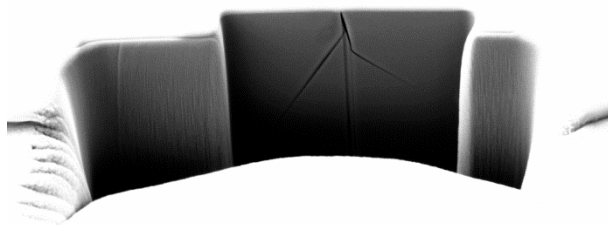
(c)



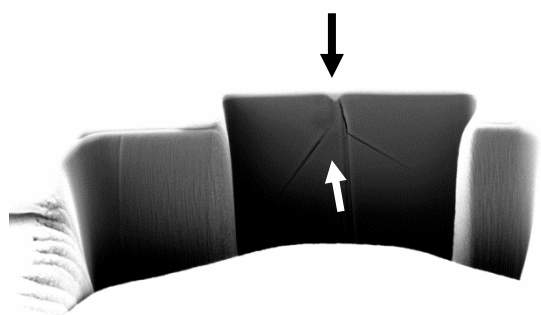
(d)



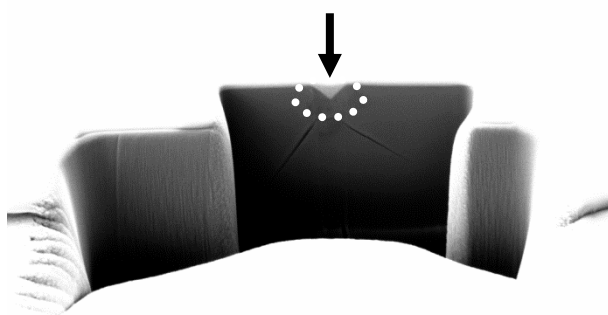
(e)



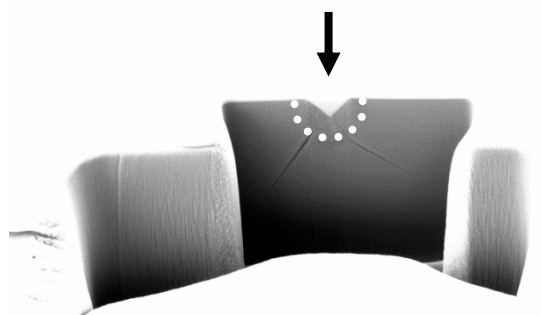
(f)



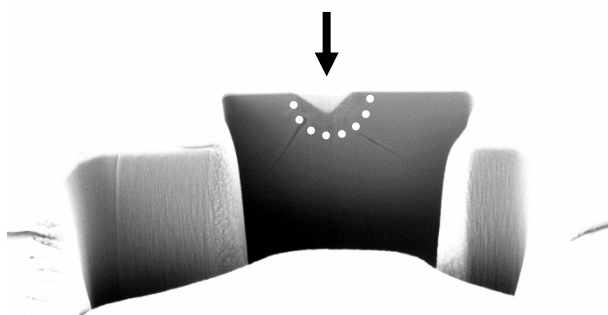
(g)



(h)



(i)



(j)

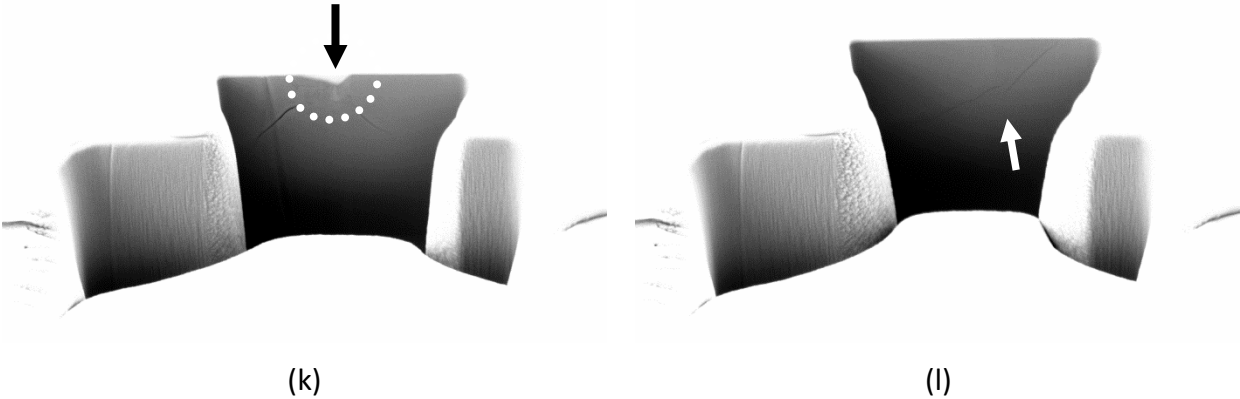
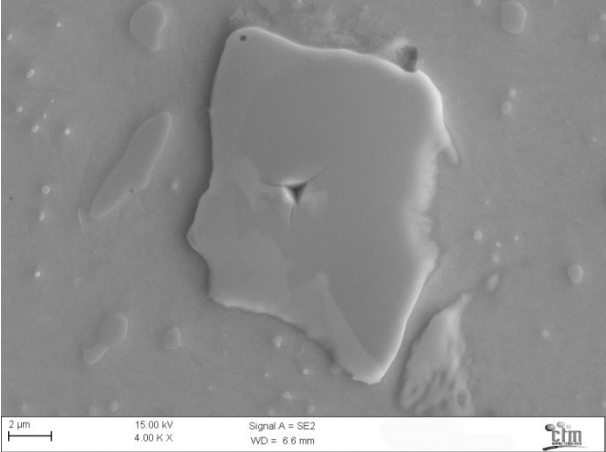
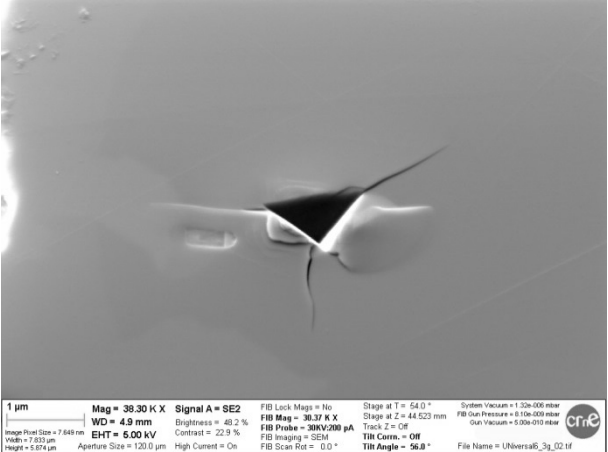


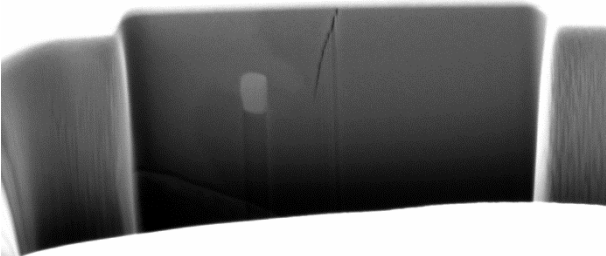
Figure 5.6.- (a) – (b) SEM images and (c)- (j) sequential FIB tomographies of a cube-corner indentation performed at 40 mN in a M_7C_3 carbide in a UNIVERSAL tool steel sample.



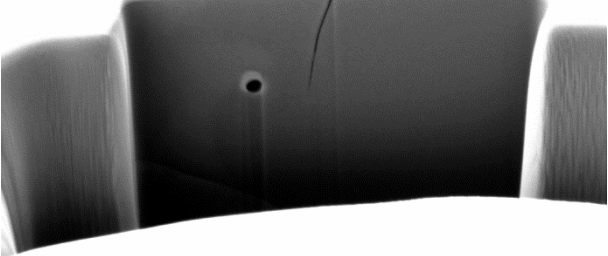
(a)



(b)



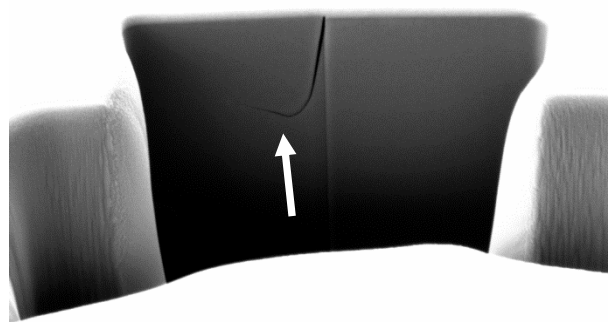
(c)



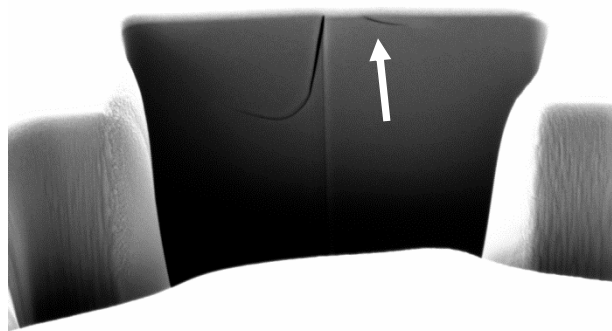
(d)



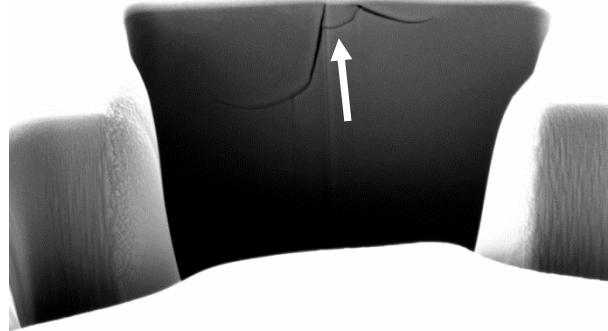
(e)



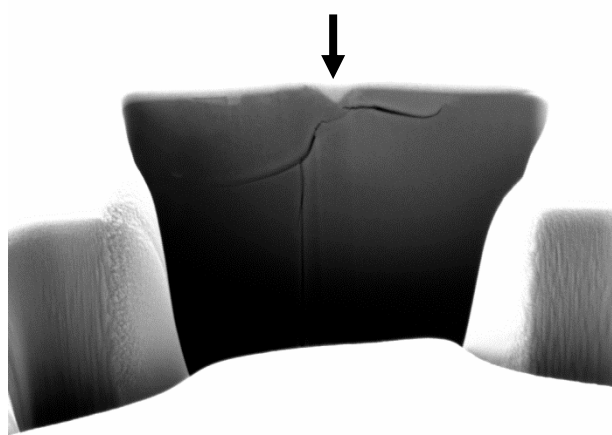
(f)



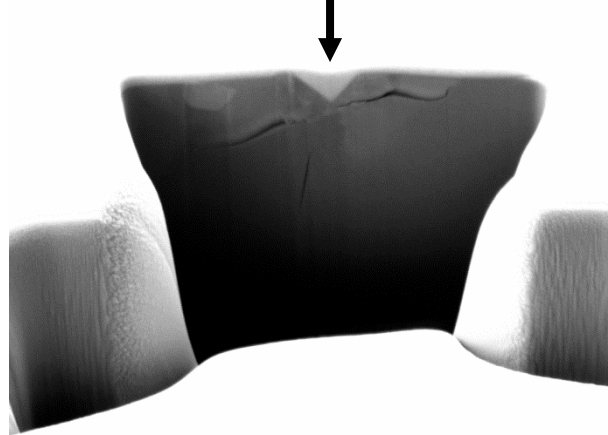
(g)



(h)



(i)



(j)

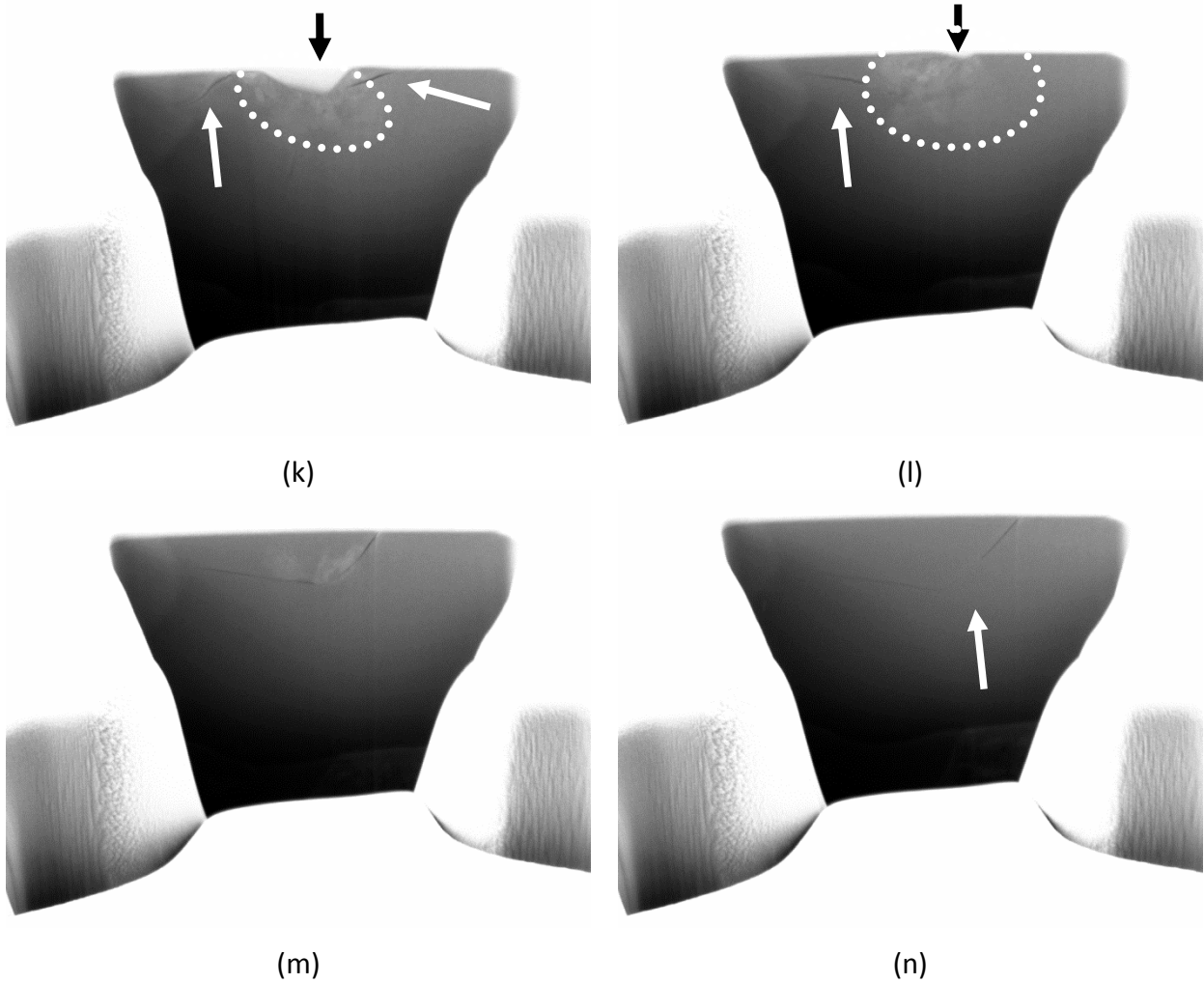
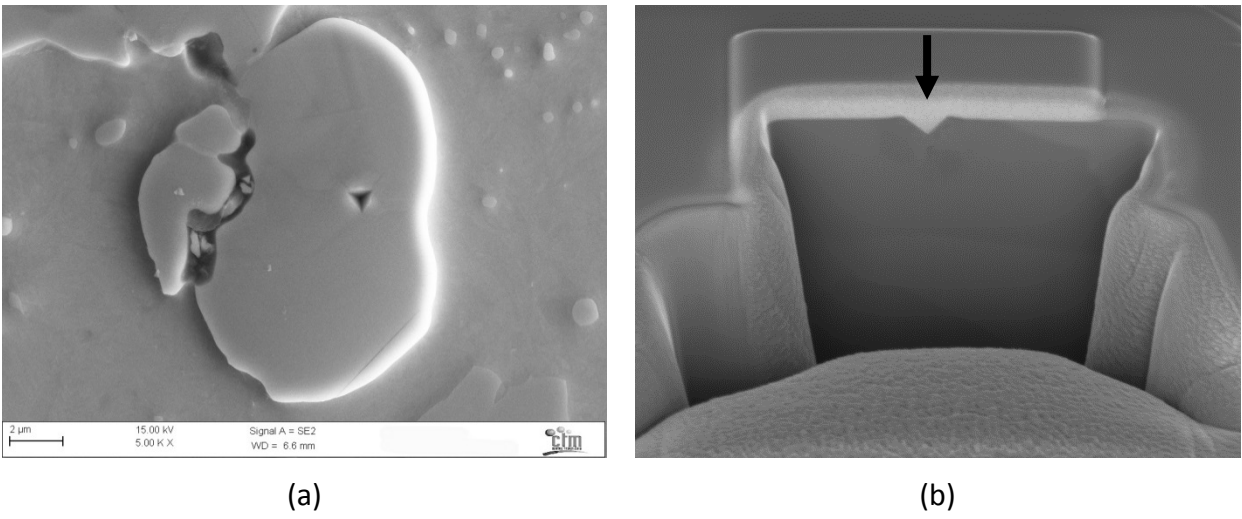


Figure 5.7.- (a) – (b) SEM images and (c)- (n) sequential FIB tomographies of a cube-corner indentation performed at 30 mN in a M_7C_3 carbide in a UNIVERSAL tool steel sample.



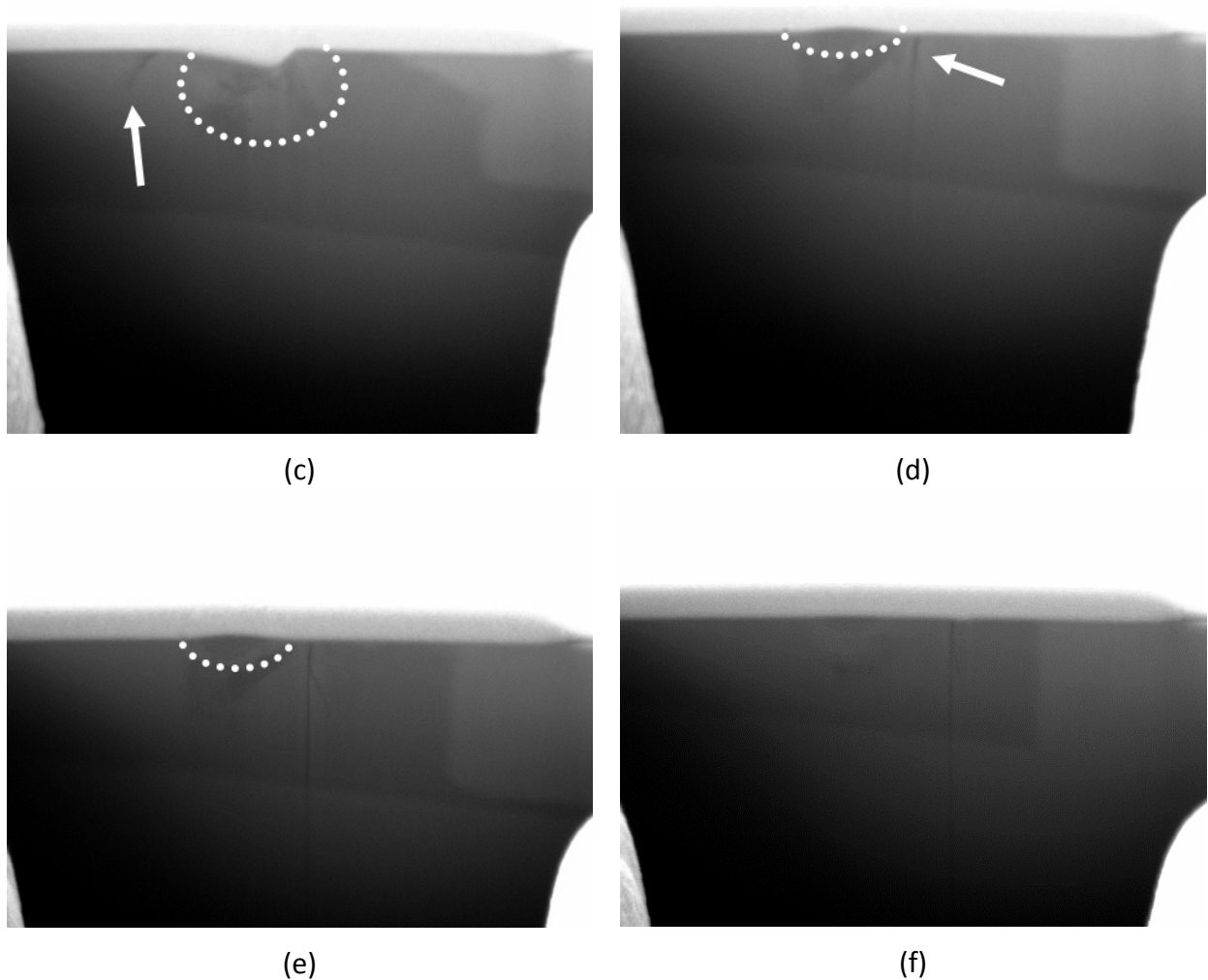


Figure 5.8.- (a) SEM images and (b)- (f) sequential FIB tomographies of a cube-corner indentation performed at 20 mN in a M_7C_3 carbide in a UNIVERSAL tool steel sample.

In order to understand the effect of load on the above observed crack evolution, from Palmqvist to quarter-penny morphology, cube-corner indentations up to 40 mN were performed. Figure 5. 9 shows K_c (evaluated by equation 1.25 with k^p of 0.057) in terms of P , which induced crack morphology changes. Only a slight variation of K_c with P was detected in the range from 20 mN to 40 mN in spite of the observed scatter. Hence, it could be said that K_c is practically the same regardless of the applied load, so that it is independent of either Palmqvist or quarter-penny crack are formed. The scatter observed in K_c can be ascribed to anisotropy effects whether caused by the heterogeneity inside the carbides or the inherent anisotropy of single crystals. With the aim to confirm these assertions sequential polishing of MC carbides in CAST WRA 46 and M_7C_3 carbides in 1.2379 was performed.

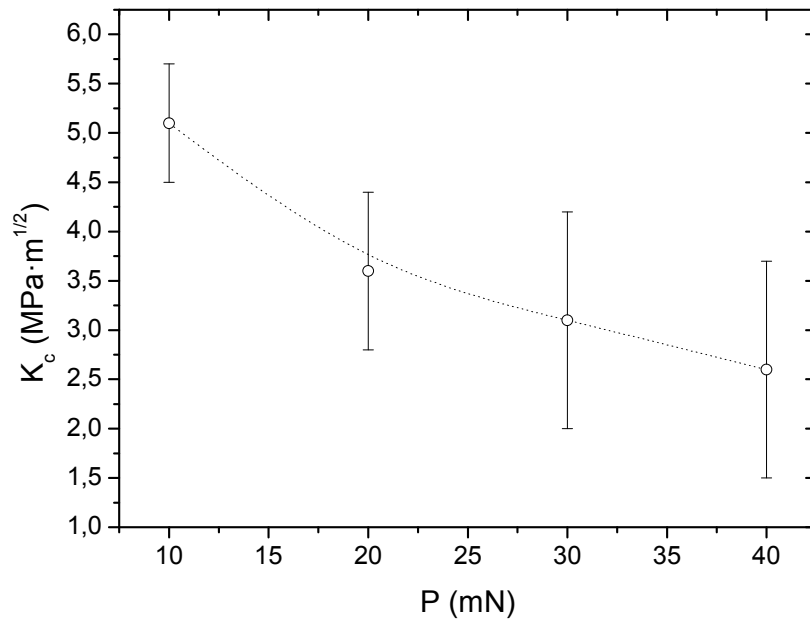
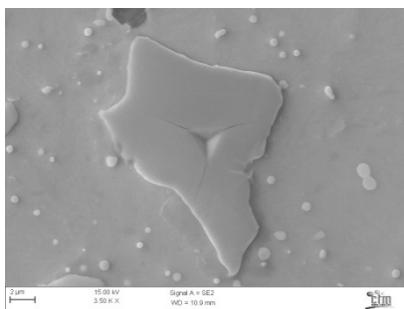
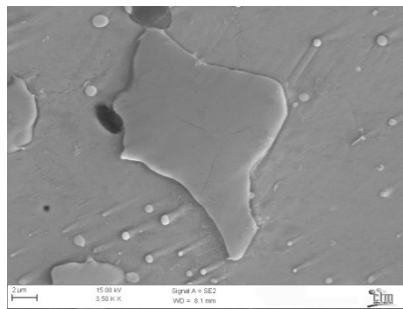


Figure 5. 9.- Plot of K_c vs. P for a M_7C_3 carbides in a UNIVERSAL sample.

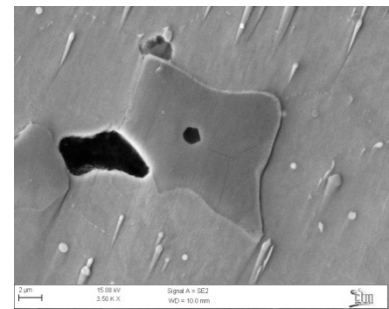
Figure 5.10 and Figure 5.11 show SEM images of the evolution of cracks and carbide morphology during the sequential polishing process. Voids present inside the carbides or carbide morphological heterogeneities interact with the cracks generating complicated crack systems. Consequently, the scatter in K_c results observed in Figure 5. 9 is mainly due to the anisotropy inherent to the carbides either morphological or crystallographic. Anisotropy effects and crack morphology effects were not clearly discernible on K_c evaluation using equation 1.25 thus, either Palmqvist or quarter-penny cracks report the same K_c value.



(a) Berkovich at 0.12 N



(b) $h = -0.30 \mu\text{m}$



(c) $h = -0.56 \mu\text{m}$

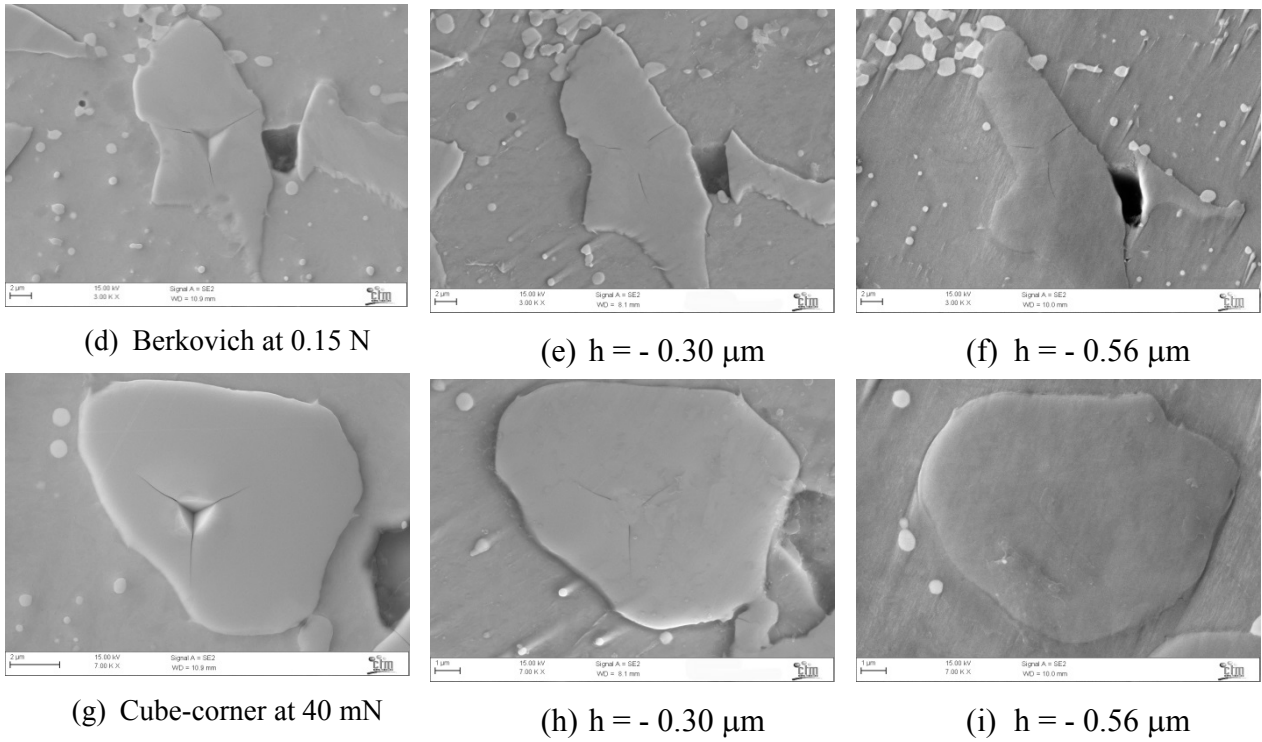
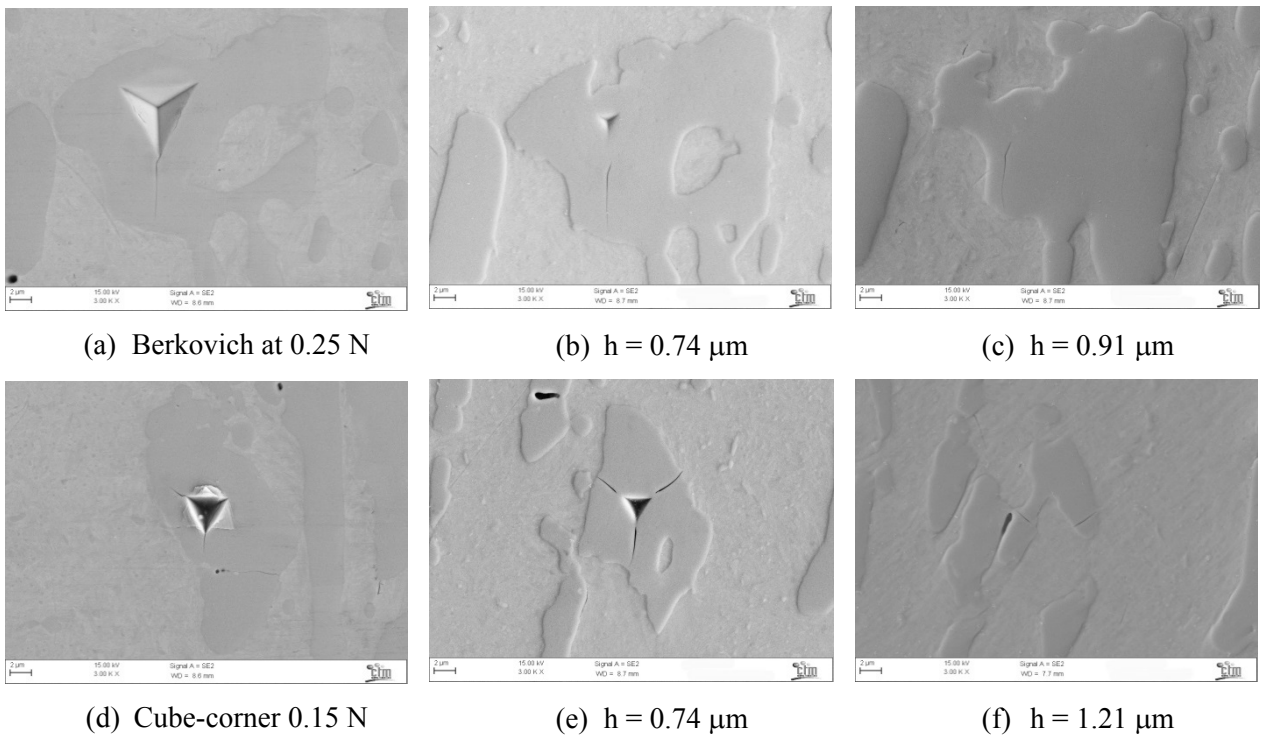


Figure 5.10.- SEM images of different sequential polishing steps of MC carbides in CAST WRA 46 tool steel.



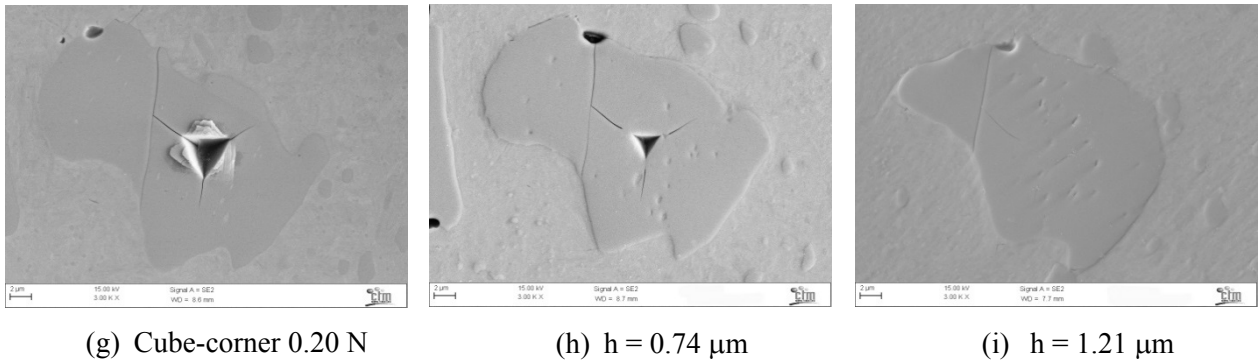


Figure 5.11.- SEM images of different sequential polishing steps of M_7C_3 carbides in 1.2379 tool steel.

The aforementioned experimental observation that K_c do not vary with P is based on results in the range from 20 mN to 40mN. Nevertheless, at 10 mN a meaningful increase in K_c is observed. Figure 5.12 shows a cube-corner indentation performed at 10 mN in a MC carbide for a UNIVERSAL tool steel. Only one small crack was achieved meaning that at such applied load was experimentally difficult to generate cracks by means of sharp indentation. Moreover, the generated crack arrested nearly at the plastic zone boundary, hence, size effects could affect to the computation of K_c since well-developed cracks are needed for using the IM method. Therefore, although low applied loads are preferred in order to generate Palmqvist cracks and apply equation 1.25 appropriately, i.e. fulfilling the conditions under which the equation was developed, lowering too much the applied load could lead to an indentation size effect.

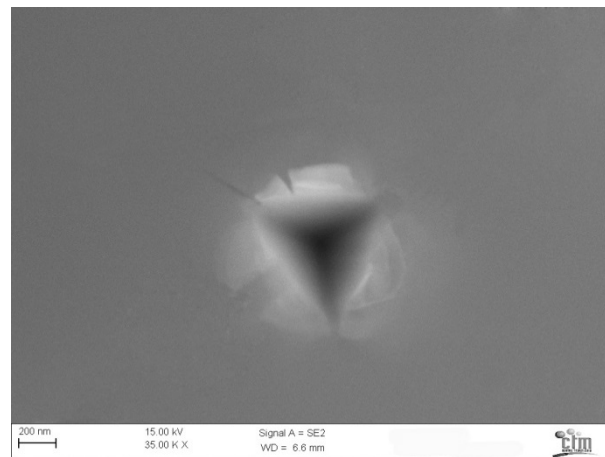


Figure 5.12.- SEM image of a cube-corner indentation performed at 10 mN in a MC carbide from a UNIVERSAL tool steel sample.

In order to corroborate the ISE observed in the M_7C_3 UNIVERSAL carbides when P is decreased in cube-corner nanoindentation, M_7C_3 carbides embedded in a 1.2379 tool steel were also analysed. Figure 5.13 shows the same tendency either carbides in UNIVERSAL or 1.2379 tool steels are analysed. Accordingly, it can be said that plasticity induced by the indentation process affects the crack growth when small volumes are analysed. Thus, K_c is affected by an ISE induced by the indentation process

itself. This assertion is validated when the influence of the applied load on K_c using Berkovich tips is quantified. Figure 5.14 shows that ISE is not present in K_c when Berkovich tips are used, even when the applied load range is similar than that used with cube-corner tips. Given this results and observing the fracture behaviour of the carbides (Figure 5.1 – Figure 5.3) when Berkovich and cube-corner tips are used, it is clear that the plasticity induced by the indentation process is crucial in order to compute a proper value for K_c .

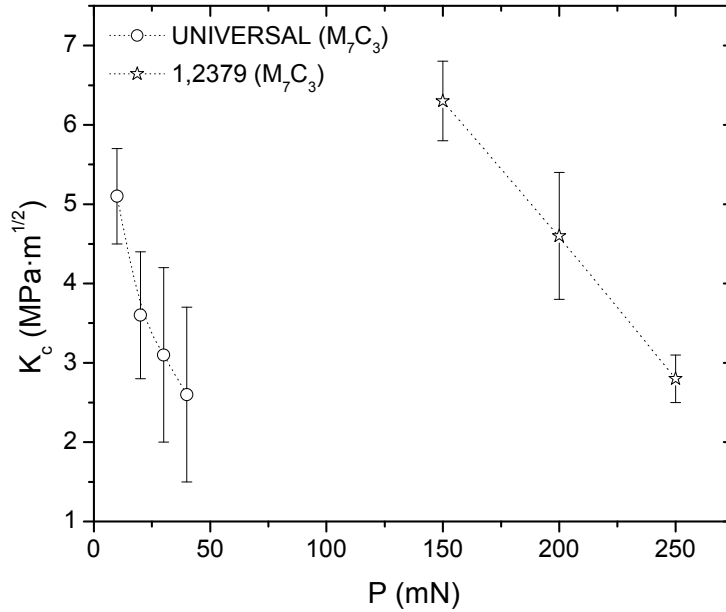


Figure 5.13.- Plot of K_c vs. P for a M_7C_3 carbides in a UNIVERSAL and 1.2379 samples when cube-corner indenters are used.

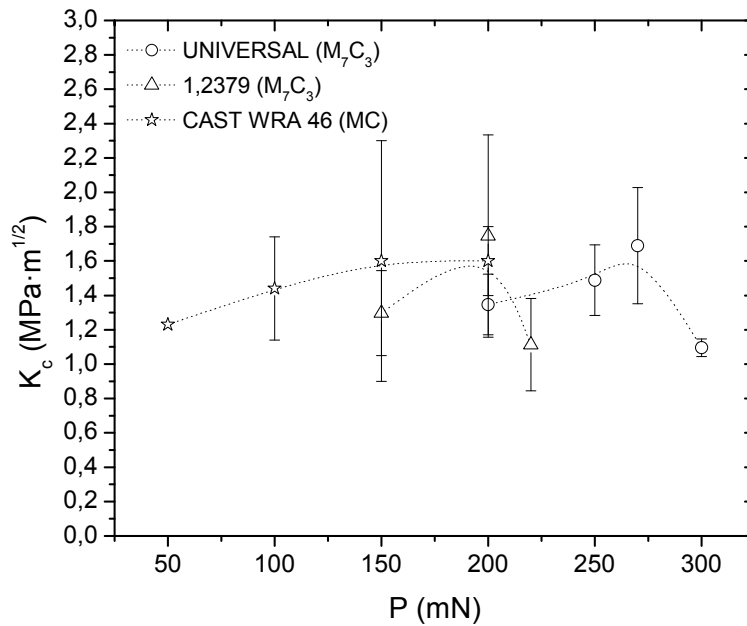


Figure 5.14.- Plot of K_c vs. P for a M_7C_3 carbides in a UNIVERSAL and 1.2379 samples when Berkovich indenters are used.

Taking into account the aforementioned results, the application of the IM method by nanoindentation does not always give a unique numeric value for K_c since many factors affect the measure. Crystal anisotropy, residual stresses, applied load among others are influencing the calculation of fracture toughness by means of nanoindentation. IM method is an easy, inexpensive and fast test in order to evaluate K_c in brittle materials, but it has been seen that extend this methodology to nanoindentation technique is not straightforward. Nevertheless, results also show that some differences in the measured values of K_c among micro-sized particles and crystal orientations can be assessed. Thus, IM by nanoindentation appears as a promising while the only to estimate fracture properties in small volumes.

5.2. COD: another method to compute fracture toughness by nanoindentation

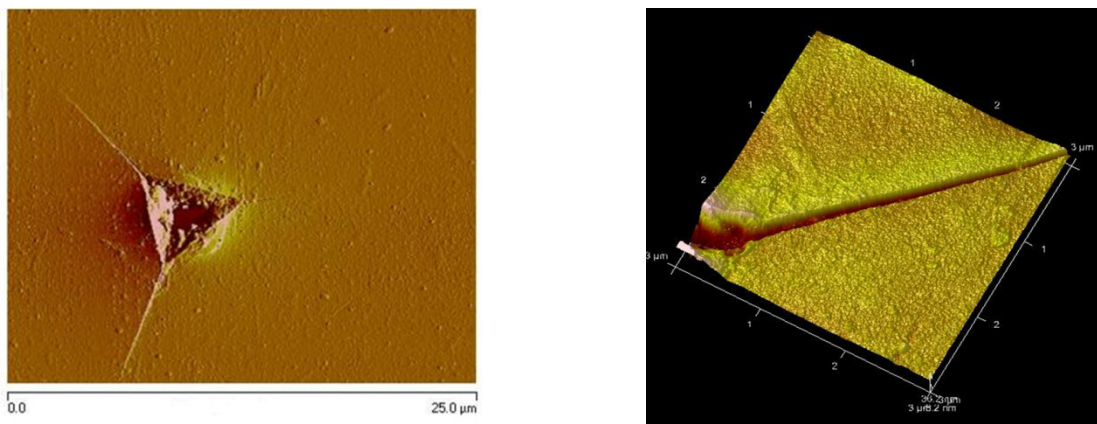
It has been proved that the IM method presents several disadvantages for calculating K_c in nanoindentation. The most critical one is the uncertainty associated with the empirical constant calibration required to calculate K_c . Such calibration depends on the indenter used and the crack morphology generated. It leads to an inherent dubiety in the computed toughness values. Another disadvantage is the indentation size effect since the IM equations depend on the hardness, elastic modulus and sometimes on the applied load, which adds further uncertainty on the K_c values obtained using this methodology. Nevertheless, the method is widely used since, if the appropriate expression is chosen,

reports K_c values close enough to that reported by other techniques that do not require any calibration as SENB method.

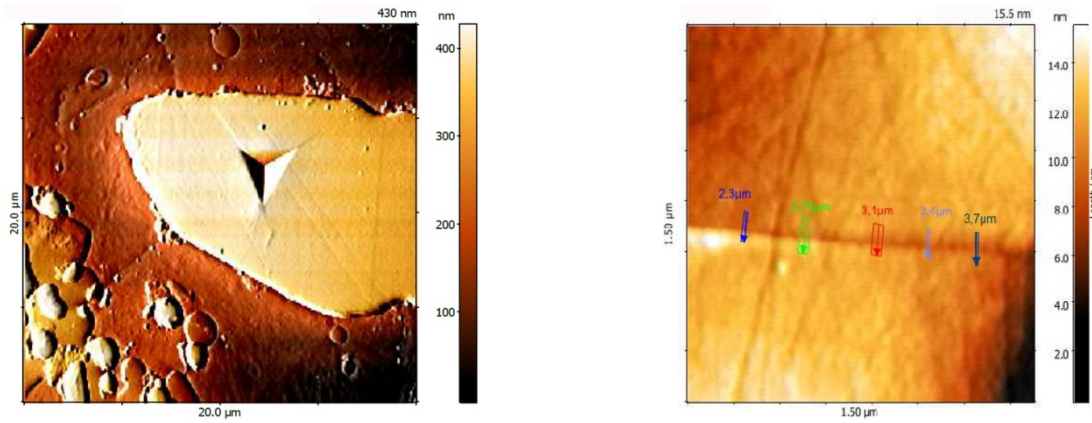
An alternative method to compute K_c has been proposed by Fett *et al.* [19] based on the measured crack-opening displacements (COD). This method offers some advantages with respect the IM method since it does not need an empirical calibration of the equation and the hardness is not part of the formulation (equation 1.30). Thus, there is no indentation size effect regarding H but, since plasticity will affect the crack growth, ISE in K_c evaluation cannot be avoided.

An important observation to be made is that the IM and the COD methods, depend on the crack morphology and thus on the indenter geometry. Accurate K_c measurements require a proper knowledge of the crack morphology in order to select the most appropriate expression for evaluating K_c . However, the final crack morphology not only depends on the tip geometry used, but also depends on the crystal structure of the indented material and on the orientation of the indenter with respect to the sample. Thus, these indentation techniques for evaluating K_c could not be the most accurate ones but sometimes are the only suitable ones for measuring K_c in small volumes.

In this thesis cube-corner indenters were used in order to generate cracks in soda-lime glass, Si (100) single crystal and MC carbides in CAST WRA 46. The crack opening displacements were measured by means of AFM. Figure 5.15a and 5.15b present AFM images of indentation imprints and their cracks in soda-lime glass and CAST WRA 46 steel, respectively, using cube-corner and Berkovich tips at 100 mN. Although here a different tip geometry was used and thus, a different crack morphology, of that used by Fett *et al.* for developing expression 1.30, the same equation without any modification was used to compute the K_c . It will allow comparing the obtained results with those computed by means of IM method. Further studies should contain a revision of the equation taken into account different tips and crack morphologies in order to evaluate how can affect it in the computed K_c value.



(a) Soda –lime glass at 100 mN



(b) MC carbide in CAST WRA 46 at 100 mN

Figure 5.15.- AFM images of (a) cube-corner indentation performed at 100 mN and (b) Berkovich indentation performed at 100 mN.

The K_c values obtained by means of IM method and COD method, as well as the accepted K_c values for the tested materials (obtained by SENB method), are compared in Table 5.3. The same cracks were used to compute K_c by either IM or COD method so that; the results are directly comparable. It can be observed that both methods give K_c values close to the accepted ones. However, it must be taken into account that fracture toughness of single crystals can be affected by its crystallography as the crack morphology can be deviated following preferential planes. Another detected experimental difficulty in WC crystals is related with the COD measurements which can be affected by the slip lines steps. Figure 5.16 shows that WC crystals exhibit marked slip lines when indented. Profiles through by AFM images in this case were unreliable since slip line steps clearly interact with the crack. Consequently, a proper value of K_c in these cases cannot be obtained using COD method.

Table 5.3.- K_c values obtained by IM method (equation (1.25)) and COD method (equation (1.30))

Sample	P (mN)	$K_c - \text{IM}$ ($\text{MPa} \cdot \text{m}^{1/2}$)	$K_c - \text{COD}$ ($\text{MPa} \cdot \text{m}^{1/2}$)	$K_c - \text{SENB}$ ($\text{MPa} \cdot \text{m}^{1/2}$)
Soda lime glass	100	0.8 ± 0.1	0.6 ± 0.1	0.7
Si (100)	10	1.0 ± 0.3	1.0 ± 0.1	0.95
MC (CAST WRA 46)	100	1.0 ± 0.3	0.8 ± 0.4	-

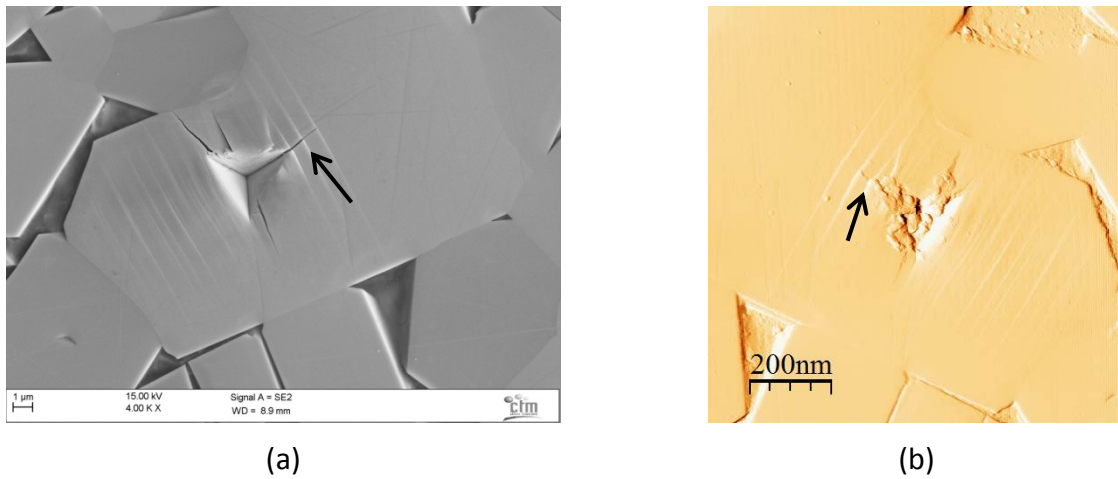


Figure 5.16.- (a) SEM image and (b) AFM image of an indented WC crystal.

In summary, in this work it was confirmed that indentation techniques compute properly K_c values. However, a study including a wide range of materials should be done in order to corroborate these preliminary results.

5.3. Multiphase materials design

This thesis shows that micromechanical characterization of micro-sized particles in terms of H , E and K_c , together with microscopic analysis of the crystals orientation, allows the proper evaluation of the fracture resistance of the hard particles. Such technique can be seen as a powerful experimental tool to understand the crack-microstructure interaction in multiphase materials, aimed at micromechanically designing materials with tailored toughness and strength.

In order to further study the crack-microstructure interaction a hardmetal with a mean size grain of $1.2 \mu\text{m}$ (GD13 hardmetal grade) was analysed. First of all a large crack were generated using a Vickers indenter at 30 N (macrohardness) , and then an EBSD analysis was performed in order to know the crack dependency on the WC single crystal orientation. Figure 5.17 shows a SEM image and their respective EBSD analysis of the crack path. It can be observed that transgranular and intergranular fracture occurs. This behaviour can be rationalized by the WC crystals anisotropy. In Chapter 4 it was experimentally assessed that prismatic facets have higher K_c than basal facets. It means that when crack has to propagate through a WC crystal, prismatic facets show higher resistance to fracture transgranular than basal one. Thus, intergranular fracture is expected to be observed more often around WC crystals when the crack tip faces prismatic facets. This behaviour is observed in the large crack produced by a high load indentation. Figure 5.17 shows the crack propagation path, through WC that has different crystallographic orientation with respect to the propagating crack. Both intergranular and transgranular fractures can be discerned. It is interesting to see that basal facets tend to show intergranular fracture (see reddish WC crystals in EBSD

image in Figure 5.17) and prismatic facets tend to fracture transgranularly (see bluish WC crystals in the EBSD image in Figure 5.17).

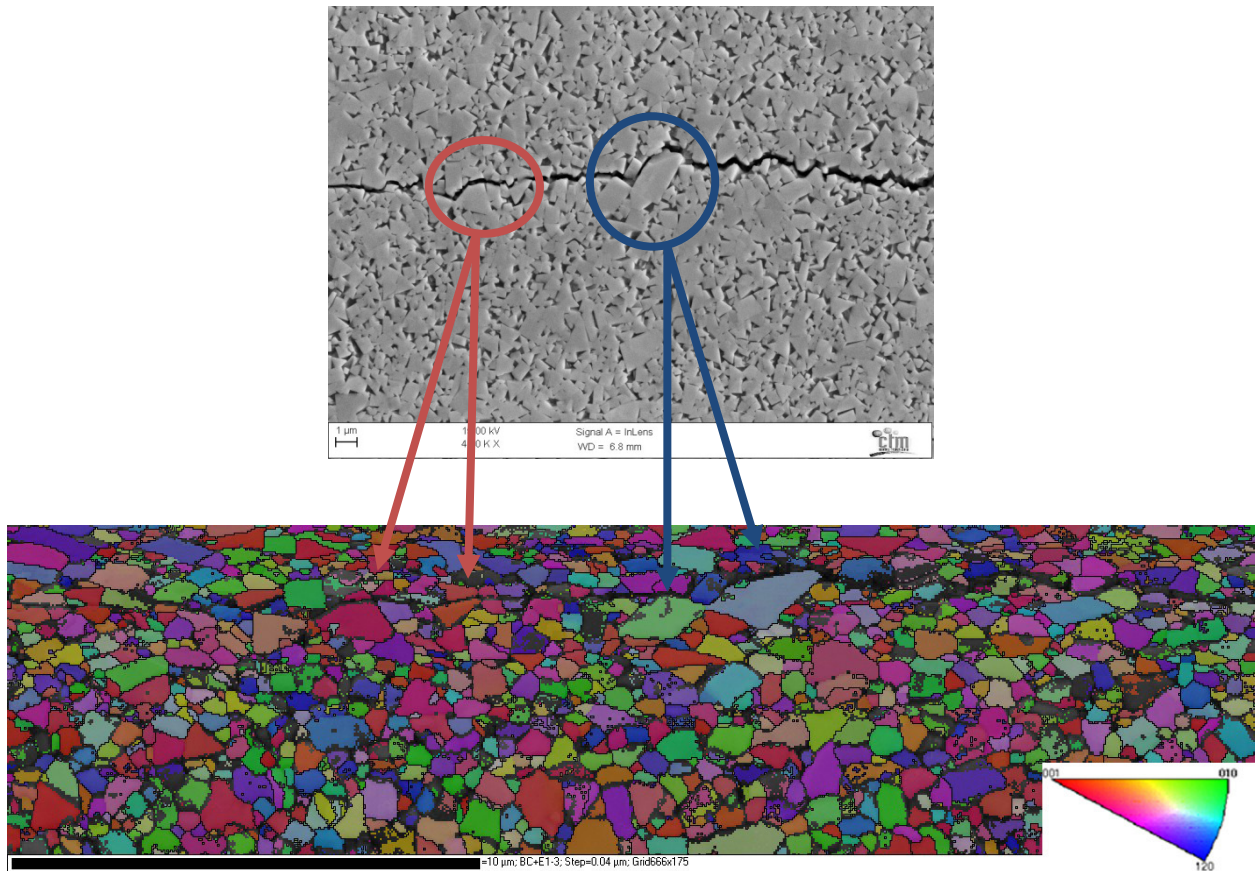


Figure 5.17.- SEM and their corresponding EBSD images of a crack path in a hardmetal sample.

The hardness/fracture toughness anisotropy together with the plasticity /fracture compromise should be considered for understanding the role of WC during crack propagation in hardmetals. In this regard, besides the relatively high toughness exhibited by this hard phase with independency of crystal orientation, the anisotropy factor may be speculated as another important microstructural factor for rationalizing the transgranular/intergranular interaction between propagating cracks and WC crystals. Research in this direction is currently in progress.

Tools steels are another example of how micromechanical characterization can help in the design of tailored materials. Primary carbides in this kind of materials play an important role on the overall mechanical behaviour of the component.

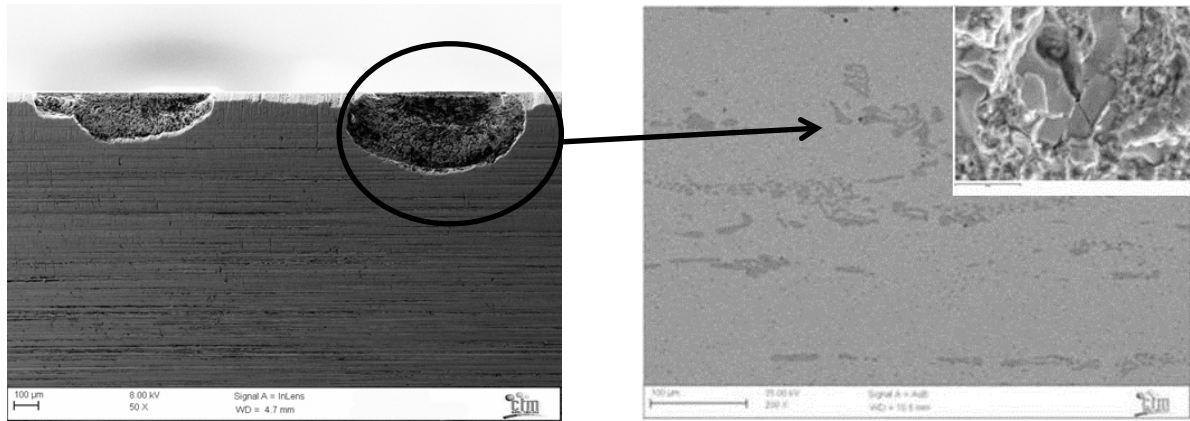


Figure 5.18._ SEM image of: (a) a damaged tool steel and (b) the initial fracture point located in a primary carbide.

Figure 5.18 shows a damaged forming tool. The fracture origin was identified to be a primary carbide. Consequently, micromechanical characterization of hard particles in tool steels is a valuable approach to design materials with improved mechanical performance. A proper combination of carbides with optimum values of hardness and toughness embedded in the right metallic matrix with the suitable size and dispersion of the carbides is needed in attain such optimization from a fracture and tribological point of view.

Chapter 6

Conclusions

It's the job that's never started as takes longest to finish.

J.R.R. Tolkien, The Lord of the Rings (1954)

6.1. Conclusions

The main aim of this thesis was to extend and to assess the applicability of the IM method for obtaining K_c of small material volumes to three-sided pyramidal indenters, particularly to cube-corner indenters. In order to fulfil this aim, an amorphous isotropic material (soda-lime glass) and two single crystals (Si (100) and SiC-6H (0001)) were widely investigated. Special attention has been paid to determine whether the crack morphology induced by three sided pyramidal tips still holds the requirements of the main equations developed for the determination of fracture toughness by the IM method. Multiphase materials including a hypereutectic Al-Si alloy, different hardmetal grades and different tool steels were also investigated to analyse anisotropy, residual stresses and matrix effects by analysing the mechanical properties of the hard phases by nanoindentation. According to the experimental results and the discussions presented in previous chapters, the following conclusions can be drawn:

1. At the same applied load, Vickers tips (four-sided pyramids) generate half-penny cracks (semi-circular), whereas Berkovich tips (three-sided pyramids) generate quarter-penny cracks (semi-elliptical). Cube-corner (three-sided pyramids) tips generate either quarter-penny or Palmqvist cracks depending on the applied load. Therefore, from a phenomenological point of view Laugier's equation would be more suitable for evaluating K_c when three-sided pyramidal indenters are used. The experimental calibration of this equation gives a calibration constant k^p of 0.022 ± 0.001 for a Berkovich indenter and 0.057 ± 0.002 for a cube-corner one. The nanoindentation fracture toughness values obtained using this calibrated equation are close to the actual K_c values measured by standardized methods that are independent of any calibration, like the SENB method, in materials without R-curve behaviour.
2. In single crystals, the crack morphology depends on the direction of the applied load with respect to the crystal axes, that is, marked anisotropy effects are observed. Besides, lateral cracks are also formed in both amorphous and single crystal samples. Thus, the crack system generated is more complex than that required for the use of fracture toughness equations of the IM method, which were developed for only either half-penny or Palmqvist crack morphologies without any concern about extra crack systems.
3. Crystal anisotropy must be considered when indenting single crystals, since indentation cracking depends on crystallographic orientation. In this sense, K_c measurements are especially sensitive to the relative crystallographic plane-indentation force. However, no evidence was found of preferred fracture directions or abrupt changes in the crack propagation direction for the two different crystal-indentation force orientations studied.

4. The calculated K_c was found to be dependent on the magnitude of the applied load because an indentation size effect is present. The IM equations depend on the hardness, elastic modulus and sometimes on the applied load, which adds further uncertainty on the K_c values obtained using this methodology. Nevertheless, the method is widely used since, if the appropriate expression is chosen, reports K_c values close enough to that reported by other techniques that do not require any calibration as SENB method.
5. Crystal anisotropy does not significantly affect the values of k^p for Berkovich and cube-corner tips. Nevertheless, consideration of the relative orientation of the indenter tip in reference to the indented plane and crystal anisotropy must be kept in mind when characterizing single crystals by nanoindentation and accurate analysis of cracks patterns is highly recommended.
6. The IM method is a reliable technique to compute K_c by means of Berkovich tips if the proper equation for fracture toughness with its experimental calibration is used. This assertion was confirmed by comparing the results of the IM method with the crack opening displacement method (COD method) which does not depend on any experimental calibration and it gives similar K_c values. These results sustain the validity of using IM method with nanoindentation with Berkovich and cube-corner tips.
7. Anisotropy affects the measure of properties in micro-sized particles as well as the overall mechanical properties of multiphase materials: a) a strong dependency of the mechanical properties according to the indented plane was observed in WC crystals, while silicon in Al-Si alloy did not exhibit any marked anisotropy. This different mechanical behaviour between Si and WC particles can be attributed to their different plastic behaviour related to the crystallographic structure (FCC for Si and HP for WC); b) the plastic and fracture behaviour in WC crystal is anisotropic, which may be another important microstructural factor for rationalizing the transgranular/intergranular interaction between propagating cracks and WC crystals. Consequently, a micromechanical design in order to improve the fracture behaviour of hardmetals is possible in terms of the orientation of their constituent WC crystals; c) In carbides of tool steels anisotropy effects involving crack deflections depend on the orientation of the crystals with respect the forging direction. Besides, the orientation between the tip and the longer axis of the carbide affects the fracture toughness since in some cases cracks are not nucleated in the three corners of the tip. Thus, anisotropy strongly affects the fracture process of micro-sized particles and consequently the overall fracture behaviour of the multiphase material.
8. Fracture toughness of hard particles is affected by residual stresses imposed by the surrounding matrix while hardness and Young's modulus are not significantly affected. It is concluded that residual stresses imposed by the matrix in Si needles modify the $P-h_s$ behaviour with respect to unstressed Si single crystals. Since the mechanical behaviour of the material under the indenter tip is different when

there is a compressive or tensile stress, the sign of the residual stresses can be determined. Although promising results were obtained, further research is needed in this field since a proper evaluation of the magnitude of the residual stresses could not be achieved in this thesis. On the contrary, residual stresses imposed by the surrounding matrix in multiphase materials do not have a measurable effect on the H and E values of micro-sized particles. For instance, MC and M_7C_3 carbides in tool steels exhibit similar mechanical properties in terms of H , E and K_c . Since all the analysed tool steels, CAST WRA 46, 1.2379 and UNIVERSAL, present approximately the same kind of metallic matrix, effects on mechanical properties and on the fracture behaviour should be the same in the analysed carbides.

9. Since cube-corner tips generate Palmqvist and quarter-penny cracks, which are both semi-elliptical, from a phenomenological point of view, Laugier equation, which is based on a semi-elliptical crack, is more appropriate. Although smaller volume can be characterised with the above tips, it is also concluded that when the applied load is decreased, ISE effects appear increasing both H and K_c . Crack changes from Palmqvist to quarter-penny cracks when the load is increased. This change in the morphology does not affect the evaluation of K_c by means of Laugier equation.

To conclude, nanoindentation was satisfactory applied in micro-sized particles being able to obtain reliable values for H , E and K_c . Nevertheless, anisotropy effects and residual stresses imposed by the surrounded matrix in multiphase materials must be taken into account. Anisotropy might introduce scatter in the results in terms of H but can strongly affect fracture behaviour. Concerning residual stresses, H and E are not significantly affected by the surrounding matrix but K_c could be significantly affected by it. Although further research is still needed, the main aim of this thesis has been achieved thus, bases for applying the IM method to characterize small material volumes by nanoindentation have been set.

6.2. Future work

This investigation was initiated with the main aim of extending IM method to nanoindentation in order to characterize small volumes in engineering materials. During the course of the work new interesting topics appeared: residual stresses determination during the indentation process, the feasibility to compute K_c by the crack opening instead of the crack length or the anisotropy effect on the mechanical properties in micro-sized particles and its effects on the material mechanical behaviour. These topics were treated during the investigation but some further work should be done.

1. Promising results on residual stresses determination by nanoindentation were obtained. Nevertheless, if a methodology would be developed, tests in smallest hard particles should be done in order to minimize the stress variations along the analysed particle and thus, the scatter in the results. Research in this field is being carried out with success in an Al-Si alloy with Si particle with an average mean size of 40 -50 μm .
2. COD method appears to be an adequate method to evaluate K_c by indentation since ISE do not affect the results and any experimental calibration is needed. In this work COD method was used to validate the results obtained by IM method. Although COD method was found to be a reliable method, further work concerning the effects of crack morphology and anisotropy on the reported K_c values should be done.
3. In this work the anisotropy effect on K_c was proved. Moreover, work on how this anisotropy could affect the mechanical behaviour of a multiphase material was started. A relationship between the deflection of a crack in a hardmetal sample and the K_c of their WC constituent crystals was found. Thus, further work in this direction will be interesting in order to correlate micro and macro mechanical behaviour.

References

- [1] K. L. Johnson, *Contact mechanics*, Cambridge University Press, London, 1985.
- [2] Ian N. Sneddon, *The relation between load and penetration in the axisymmetric boussinesq problem for a punch of arbitrary profile*, International journal of engineering science (3), 1965.
- [3] R. Hill, *The mathematical theory of plasticity*, Oxford University Press, New York, 1950.
- [4] Y.T. Cheng and C.M. Cheng, *Scaling, dimensional analysis, and indentation measurements*, Materials Science & Engineering R-Reports (44), 2004.
- [5] A.C. Fischer-Cripps., *Nanoindentation*, Springer-Verlag New York, Inc.;2002
- [6] W.C. Oliver and G.M. Pharr, *An Improved Technique for Determining Hardness and Elastic-Modulus using Load and Displacement Sensing Indentation Experiments*, Journal of Materials Research (7), 1992.
- [7] W.C. Oliver and G.M. Pharr, *Measurement of hardness and elastic modulus by instrumented indentation: Advances in understanding and refinements to methodology*, Journal of Materials Research (19), 2004.
- [8] Y.I. Golovin, *Nanoindentation and mechanical properties of solids in submicrovolumes, thin near-surface layers, and films: a review*, Physics of the Solid State (50), 2008.
- [9] T. Fett and D. Munz, *Influence of narrow starter notches on the initial crack growth resistance curve of ceramics*, Archive of Applied Mechanics (76), 2006.
- [10] B.R. Lawn, A.G. Evans and D.B. Marshall, *Elastic-Plastic Indentation Damage in Ceramics - the Median-Radial Crack System*, Journal of the American Ceramic Society (63), 1980.
- [11] G.R. Anstis, P. Chantikul, B.R. Lawn and D.B. Marshall, *A Critical-Evaluation of Indentation Techniques for Measuring Fracture-Toughness .1. Direct Crack Measurements*, Journal of the American Ceramic Society (64), 1981.
- [12] G.D. Quinn and R.C. Bradt, *On the Vickers indentation fracture toughness test*, Journal of the American Ceramic Society (90), 2007.
- [13] T. Zhang, Y. Feng, R. Yang and P. Jiang, *A method to determine fracture toughness using cube-corner indentation*, Scripta Materialia (62), 2010.

- [14] K.I. Schiffmann, *Determination of fracture toughness of bulk materials and thin films by nanoindentation: comparison of different models*, Philosophical Magazine (91), 2011.
- [15] D.J. Morris and R.F. Cook, *In situ cube-corner indentation of soda-lime glass and fused silica*, Journal of the American Ceramic Society (87), 2004.
- [16] R.F. Cook and G.M. Pharr, *Direct Observation and Analysis of Indentation Cracking in Glasses and Ceramics*, Journal of the American Ceramic Society (73), 1990.
- [17] K. Niihara, R. Morena and D.P.H. Hasselman, *Evaluation of K_{Ic} of Brittle Solids by the Indentation Method with Low Crack-To-Indent Ratios*, Journal of Materials Science Letters (1), 1982.
- [18] M.T. Laugier, *New Formula for Indentation Toughness in Ceramics*, Journal of Materials Science Letters (6), 1987.
- [19] T. Fett, A.B. Kouna Njiwa and J. Rödel. *Crack opening displacements of Vickers indentation cracks*, Engineering Fracture Mechanics (72), 2005.
- [20] B. Lawn, *Fracture of Brittle Solids-Second Edition*, Cambridge University Press, New York, 1993
- [21] Y.B. Xin, K.J. Hsia and D.A. Lange, *Quantitative characterization of the fracture surface of Si single crystals by confocal microscopy*, Journal of the American Society (78), 1995.
- [22] J.L. Henshall and C.A. Brookes, *The Measurement of K_{Ic} in Single-Crystal SiC using the Indentation Method*, Journal of Materials Science Letters (4), 1985
- [23] A.V. Shatov, S.S. Ponomarev and S.A. Firstov, *Fracture of WC–Ni cemented carbides with different shape of WC crystals*, International Journal of Refractory Metals and Hard Materials (26), 2008.
- [24] S. Lay, C.H. Allibert, M. Christensen and G. Wahnström, *Morphology of WC grains in WC–Co alloys*, Materials Science and Engineering: A (486), 2008.
- [25] L. Pons, *Plastic properties in tungsten monocarbide, Anisotropy in single-crystal refractory compounds*, Vahldiek, Fred W., Mersol, Stanley A, New York, 1968.
- [26] J.C. Hay, A. Bolshakov and G.M. Pharr, *A critical examination of the fundamental relations used in the analysis of nanoindentation data*, Journal of Materials Research (14), 1999.
- [27] J.B. Pethica and W.C. Oliver, *Mechanical properties of nanometer volumes of materials: use of the elastic response of small area indentations*, Materials Research Society Symposium Proceedings (130), 1989.

- [28] B.N. Lucas, W.C. Oliver and J.E. Swindeman, *The dynamics of frequency-specific, depth-sensing indentation testing*, Fundamentals of Nanoindentation and Nanotribology (522), 1998.
- [29] S.S. Chiang, D.B. Marshall and A.G. Evans, *The Response of Solids to Elastic Plastic Indentation. (1) Stresses and Residual-Stresses*, Journal of Applied Physics (53), 1982.
- [30] J. Jang and G.M. Pharr, *Influence of indenter angle on cracking in Si and Ge during nanoindentation*, Acta Materialia (56), 2008.
- [31] T. Lube, *Indentation crack profiles in silicon nitride*, Journal of the European Ceramic Society (21), 2001.
- [32] F. Elfallagh and B.J. Inkson, *3D analysis of crack morphologies in silicate glass using FIB tomography*, Journal of the European Ceramic Society (29), 2009.
- [33] S.J. Bull, *Analysis methods and size effects in the indentation fracture toughness assessment of very thin oxide coatings on glass*, Comptes Rendus Mecanique (339), 2011.
- [34] R.F. Cook, *Strength and sharp contact fracture of silicon*, Journal of Materials Science (41), 2006.
- [35] J.I. Jang, M.J. Lance, S.Q. Wen, T.Y. Tsui and G.M. Pharr, *Indentation-induced phase transformations in silicon: influences of load, rate and indenter angle on the transformation behavior*, Acta Materialia (53), 2005.
- [36] G.M. Pharr, W.C. Oliver and D.S. Harding, *New Evidence for a Pressure-Induced Phase-Transformation during the Indentation of Silicon*, Journal of Materials Research (6), 1991.
- [37] G.M. Pharr, W.C. Oliver and D.R. Clarke, *The Mechanical-Behavior of Silicon during Small-Scale Indentation*, Journal of Electronic Materials (19), 1990.
- [38] D. Kramer, H. Huang, M. Kriese, J. Bobach, J. Nelson, A. Wright, D. Bahr, W.W. Gerberich, *Yield strength predictions from the plastic zone around nanocontacts*, Acta Materialia (47), 1998.
- [39] M. Yoshioka, *Plastically Deformed Region Around Indentations on Si Single-Crystal*, Journal of Applied Physics (76), 1994.
- [40] C.L. Woodcock and D.F. Bahr, *Plastic zone evolution around small scale indentations*, Scripta Materialia (43), 2000.

- [41] P. Puech, S. Pinel, R.G. Jasinevicius and P.S. Pizani, *Mapping the three-dimensional strain field around a microindentation on silicon using polishing and Raman spectroscopy*, Journal of Applied Physics (88), 2000.
- [42] K. Zeng, A.E. Giannakopoulos and D.J. Rowcliffe, *Vickers Indentations in Glass. (2) Comparison of Finite-Element Analysis and Experiments*, Acta Metallurgica Et Materialia (43), 1995.
- [43] L.C. Zhang and I. Zarudi, *Towards a deeper understanding of plastic deformation in monocrystalline silicon*, International Journal of Mechanical Sciences (43), 2001.
- [44] K E. Petersen, *Silicon as a mechanical material*, Proceedings of IEEE (70), 1982.
- [45] T.F. Page, L. Rester and S.V. Hainsworth, *The plasticity response of 6H-SiC and related isostructural materials to nanoindentation: Slip vs densification*, Fundamentals of Nanoindentation and Nanotribology (522), 1998.
- [46] F. Ebrahimi and L. Kalwani, *Fracture anisotropy in silicon single crystal*, Materials Science and Engineering A-Structural Materials Properties Microstructure and Processing (268), 1999.
- [47] J. Alcala, L. Llanes and M. Anglada, *Fracture characteristics of silicon nitride at elevated T*, Fourth euro ceramics (3), 1995.
- [48] S. Fuenfschilling, T. Fett, R. Oberacker, M.J. Hoffmann, G.A. Schneider, P.F., Becher, J.J. Kruzic, *Crack-Tip Toughness from Vickers Crack-Tip Opening Displacements for Materials with Strongly Rising R-Curves*, Journal of the American Ceramic Society (94), 2011.
- [49] R.D. Dukino and M.V. Swain., *Comparative Measurement of Indentation Fracture-Toughness with Berkovich and Vickers Indenters*, Journal of the American Ceramic Society (75), 1992.
- [50] D.S. Harding, W.C. Oliver and G.M. Pharr, *Cracking during nanoindentation and its use in the measurement of fracture toughness*, Thin Films: Stresses and Mechanical Properties V (356), 1995.
- [51] G.M. Pharr, D.S. Harding and W.C. Oliver, *Measurement of Fracture-Toughness in Thin-Films and Small Volumes using Nanoindentation Methods*, Mechanical Properties and Deformation Behavior of Materials Having Ultra-fine Microstructures (233);1993
- [52] G.M. Pharr, *Measurement of mechanical properties by ultra-low load indentation*, Materials Science and Engineering A-Structural Materials Properties Microstructure and Processing (253), 1998.
- [53] S.S. Zumdahl and S.A. Zumdahl, *Chemistry*, Charles Hatford - Brooks Cole, Belmont (USA), 2010.

- [54] Y.B. Xin, K.J. Hsia and D.A. Lange, *Quantitative characterization of the fracture surface of Si single crystals by confocal microscopy*, Journal of the American Ceramic Society (78), 1995.
- [55] B. Roebuck, P. Klose and K.P. Mingard, *Hardness of hexagonal tungsten carbide crystals as a function of orientation*, Acta Mater. (60), 2012.
- [56] E. Söderlund and D.J. Rowcliffe, *Analysis of penetration curves produced by depth-sensing indentation systems*, Journal of hard materials (5), 1994.
- [57] D.N. French and D.A. Thomas, *Hardness anisotropy and slip in WC crystals*, Transactions of the Metallurgical Society of AIME (233), 1965.
- [58] R. Warren, *Measurement of Fracture Properties of Brittle Solids by Hertzian Indentation*, Acta Metallurgica (26), 1978,
- [59] R.K. Viswanadham, T.S. Sun, E.F. Drake and J.A. Peck, *Quantitative Fractography of WC-Co Cermets by Auger-Spectroscopy*, Journal of Materials Science (16), 1981.
- [60] L. Llanes, Y. Torres and M. Anglada, *On the fatigue crack growth behavior of WC-Co cemented carbides: kinetics description, microstructural effects and fatigue sensitivity*, Acta Materialia (50), 2002,
- [61] D. Casellas, J. Caro, S. Molas, J.M. Prado and I. Valls, *Fracture toughness of carbides in tool steels evaluated by nanoindentation*, Acta Materialia (55), 2007.
- [62] R. Nowak and M. Sakai, *The Anisotropy of Surface Deformation of Sapphire - Continuous Indentation of Triangular Indenter*, Acta Metallurgica Et Materialia (42), 1994.
- [63] S. Suresh and A.E. Giannakopoulos, *A new method for estimating residual stresses by instrumented sharp indentation*, Acta Materialia (46), 1998.
- [64] J. Malzbender, G. de With and J.M. J. den Toonder, *Elastic modulus, indentation pressure and fracture toughness of hybrid coatings on glass*, Thin Solid Films (366), 2000.

Published articles

J. Fornell; A. Concustell; S. Surinach; W.H. Li; N. Cuadrado; A. Geberet; M.D. Baro; J. Sort, *Yielding and intrinsic plasticity of Ti-Zr-Ni-Cu-Be bulk metallic glass*, International Journal of plasticity (25), 2009.

N. Cuadrado; D. Casellas; J. Caro; L. Llanes, *Caracterización mediante la técnica de nanoindentación de partículas duras*, XXVI encuentro del grupo español de fractura ISSN 0213-3725 (2), 2009.

I. Picas; N. Cuadrado; D. Casellas; A. Goez; L. Llanes, *Microstructural effects on the fatigue crack nucleation in cold work tool steels*, Procedia Engineering (2), 2010.

J.G. La Barbera-Sosa; Y.Y. Santana, E. Moreno, N. Cuadrado; J. Caro; P.O. Renault; E. Le Bourhis; M.H. Staia; E.S. Puchi-Cabrera, *Effect of spraying distance on the microstructure and mechanical properties of a Colmonoy 88 alloy deposited by HVOF thermal spraying*, Surface and Coatings Technology (205), 2010.

N. Cuadrado; E. Jiménez-Piqué; D. Casellas; M. Anglada, *Estudio de la morfología de grietas generadas por nanoindentación y su efecto en el cálculo de la tenacidad de fractura*, XXVIII encuentro del grupo español de fractura ISSN 0213-3725 (2), 2011.

I. Picas; N. Cuadrado; D. Casellas; A. Goez; L. Llanes, *Efecto de la microestructura en la nucleación y propagación de fisuras en aceros de herramienta de trabajo en frío*, XXVIII encuentro del grupo español de fractura ISSN 0213-3725 (1), 2011.

J. Caro; N. Cuadrado; I. Gonzalez; D. Casellas; J.M. Prado; A. Vilajoana; P. Artús; S. Peris; A. Carrilero; J.C. Dürsteler, *Microscratch resistance of ophthalmic coatings on organic lenses*, Surface and Coatings Technology (205), 2011.

N. Cuadrado; D. Casellas; L. Llanes; I. Gonzalez; J. Caro, *Effect of cristal anisotropy on the mechanical properties of WC-Co cemented carbides*, Euro PM2011 (2), 2011.

N. Cuadrado; D. Casellas; M. Anglada; E. Jimenez-Pique, *Evaluation of fracture toughness of small volumes by means of cube-corner nanoindentation*, Scripta Materialia (66), 2012.